

Strain Functionals: A Complete and Symmetry-adapted Set of Descriptors to Characterize Atomistic Configurations

Edward M. Kober,^{*,a} Jacob P. Tavenner,^{*,2} Colin M. Adams,^{*,3} Nithin Mathew^{*,1}

^{*}Group T-1, Theoretical Division, Los Alamos National Laboratory, Los Alamos, NM 87544

¹Center for Non-Linear Studies, Theoretical Division, Los Alamos National Laboratory, Los Alamos, NM 87544

²Department of Mechanical Engineering, Colorado School of Mines, Golden, CO 80401

³Department of Physics, Harvey Mudd College, Claremont, CA 91711

^aCorresponding author: emk@lanl.gov

Abstract

Extracting relevant information from atomistic simulations relies on a complete and accurate characterization of atomistic configurations. We present a framework for characterizing atomistic configurations in terms of a complete and symmetry-adapted basis, referred to as strain functionals. In this approach a Gaussian kernel is used to map discrete atomic quantities, such as number density, velocities, and forces, to continuous fields. The local atomic configurations are then characterized using n^{th} order central moments of the local number density. The initial Cartesian moments are recast unitarily into a Solid Harmonic Polynomial basis using SO(3) decompositions. Rotationally invariant metrics, referred to as Strain Functional Descriptors (SFDs), are constructed from the terms in the SO(3) decomposition using Clebsch-Gordan coupling. A key distinction compared to related methods is that a minimal but complete set of descriptors is identified. These descriptors characterize the local geometries numerically in terms of shape, size, and orientation descriptors that recognize n -fold symmetry axes and net shapes such as trigonal, cubic, hexagonal, etc. They can easily distinguish between most different crystal symmetries using $n = 4$, identify defects (such as dislocations and stacking faults), measure local deformation, and can be used in conjunction with machine learning techniques for *in situ* analysis of finite temperature atomistic simulation data and quantification of defect dynamics.

1. Introduction

Macroscopic properties of materials are governed by generation and propagation of defects at the atomic scale and their interaction with the microstructure. Atomistic simulation methods, using *ab initio* or empirical interatomic potentials have enabled us to study these processes with atomic scale resolution. The extraction of information from these atomistic simulation techniques often relies on identifying and categorizing the local configurations/geometries around atomic centers. For example, in simulations of crystalline materials, deformation processes give rise a variety of defect structures (vacancies and interstitials, point defect clusters, dislocation loops, stacking faults, twins

etc.) that can be identified by the distinct local geometries of the atoms associated with the defects. A wide variety of techniques have been developed to achieve these goals and these have been reviewed by Stukowski who has pointed out the relative merits and limitations of the various techniques.^{1, 2} Many of these methods, such as the common neighbor analysis,^{3, 4} are specific to particular crystal systems (*e.g. fcc, bcc, hcp*). Some, such as centrosymmetry analysis,⁵ Steinhardt order parameters,⁶ bond-angle analysis,⁷ diamond structure analysis,⁸ and Voronoi-type analyses^{4, 9} rely on a limited set of symmetry functions/heuristic rules applied to a specific listing of neighbors. These are not necessarily robust under thermal fluctuations. To overcome these limitations, recent methods^{10, 11} have relied on ‘shape/pattern/template matching’ techniques using diverse set of shape and orientation descriptors. Methods using geometric constructions such as the Burger’s circuit construction^{12, 13}, Nye tensor calculations,¹⁴ or perturbations of the Voronoi topology¹⁵ have also been applied with good success. Recently, there has been a lot of interest in developing physics-inspired descriptors of atomic environments^{16, 17-23} which is partly motivated by the application of data-driven approaches for materials modeling. A comprehensive review of these methods and their relationships has recently been published.²⁴ While these approaches have their own particular advantages, the physical meaning of these descriptors, in terms of symmetry elements of atomic environments, remains unclear. Moreover, the large number of descriptors used in these approaches to describe atomic environments suggest either redundancies in the underlying basis are present or a strong dependence on thermal fluctuations, especially for the higher order terms.

We present an approach for characterizing atomic geometries and identifying symmetry elements based on the technique of moment analyses. Moment analyses have been used for several decades as a means to characterize three-dimensional (3D) structures, especially for image/pattern analysis.²⁵⁻²⁷ The parallels with identifying atomic geometries using such an approach are obvious, albeit the irregular distributions of atoms due to localized strains/defects and thermal fluctuations adds computational complexity compared to working with regular arrays of pixels and voxels. We also note that there are inherent parallels between the moment analyses and gradients of the distributions. While the n^{th} order moments are easy to calculate in a particular reference frame (often expressed in terms of spherical harmonic or harmonic polynomial functions), the comparison between similar objects (geometries) in different reference frames requires using rotationally invariant formulations, and these aspects have not been fully developed. An approach for building rotational invariance into 3D moment analysis was developed by Lo & Don²⁸ using techniques of angular momentum (or Clebsch-Gordan) coupling.²⁹ Lo & Don had demonstrated this approach for second and third order moments and identified several different invariant descriptors for those orders. However, they did not present a clear means by which a unique set of descriptors could be developed, nor did they develop a geometric understanding of what each of the terms implied. A mathematically-related approach based on irreducible tensors has also been presented along with its applicability to physical properties that can be described by third and fourth order tensors.³⁰ Again, this approach identifies some of the invariants, but is incomplete in their description. In related work on Magnetic Resonance Imaging (MRI), Kindlmann and co-workers^{31, 32} have formulated an orthonormal set of rotationally invariant fourth order descriptors that is highly relevant to

the work here, though their feature space is more limited because of the higher symmetry of the diffusion tensor. They do attach physical significance to their descriptors and point out that there are different frameworks in which these can be cast depending on the desired physical interpretations.

The goal here is to consolidate these types of approaches through fourth order in an extensible framework appropriate for the interpretation of deformations. Fourth is the minimal order required to distinguish most crystal symmetries and deformations, where sixth order would be required to distinguish variations of hexagonal symmetry. We aim to develop a complete, general, and symmetry-adapted method that utilizes symmetry elements derived from local neighborhood moments to develop descriptors for describing these atomistic geometries. As the descriptors cannot depend upon the relative orientations of the experimental and observation frames, they can be defined within the 3D rotation group, $SO(3)$, and all features of the deformation must be describable using the rotationally invariant basis functions of that group. These basis functions can be expressed in terms of functions that carry angular momentum (e.g. spherical harmonic or harmonic polynomial functions) that are combined and contracted using the Clebsch-Gordan coefficients. Such a framework has been previously utilized in the development of the Steinhardt parameters,⁶ the SOAP descriptors¹⁸ and the related GAP method,¹⁷ the SNAP potentials^{33, 34}, the Moment Tensor Potentials^{22, 35}, and Atomic Cluster Expansion (ACE).²³ A somewhat similar logic was used in the earlier development of the EAM and MEAM potentials.³⁶⁻³⁸ While the rotational invariance of these approaches is mathematically correct, they use a variety of methods for defining a local neighborhood (e.g., simple radial cutoffs, splined functions) that result in complex basis functions that are not readily interpreted. Here, we use a simple Gaussian kernel to define the neighborhood, which allows us to develop a complete, minimal, and orthogonal set of descriptors with clear physical/geometric meaning in terms of shape, size, and orientation of atomic configurations.

Beyond the immediate goal of describing the local deformations in atomic neighborhoods, the method of moment expansions has other physical significance. Foremost, there should be a strong relationship to similar tensorial expansions of physical properties.³⁰ When applied to the local atomic density, the moments are a method for characterizing the nature of the local strain field.³⁹ That is, the moments measure the gradients in local number density which in turn reflects the existence of local strain and its gradients. We note here that local atomic strain, in the strict continuum mechanics sense, has also been defined in multiple previous works using deformation gradient tensor calculated utilizing different radial kernels.³⁹⁻⁴⁴ Such analyses have provided a good means for characterizing macroscopic deformation processes. Again, by using a simple Gaussian kernel, we can formalize these analyses in terms of a Taylor's series expansion and develop a better understanding of the deformation processes.

2. Method

2.1. Continuous fields and their derivatives from discrete quantities

For this initial development, we will consider a system where all of the atoms are of the same type. The standard difficulty in defining strains (and other continuum physical

quantities) of atomistic systems is that the atomic positions are treated as discrete points, and some sort of smoothing function or kernel must be applied in order to map the discrete quantities to a continuum function. As will become apparent below, these functions then define the characteristics of the “neighborhood” of each atom. Various techniques, such as cubic splines or graded step functions,⁴³ hard-sphere cut-off with unit weighting,³⁹ and cosine switching function^{17, 45} have been employed for performing this smoothing. The problem with the approaches using a cut-off function is that, being based on discrete neighbor lists, the atomic “neighborhoods” change discontinuously during dynamic simulations and this frustrates defining continuum properties with desirable properties such as continuity and curl-free fields. Employing smoothing functions at cutoff distances can alleviate, but not eliminate, these issues, but they do introduce complexities in describing the radial dependence of the resulting descriptors. Here, we will use Gaussian kernels as our smoothing functions which have the useful property of being infinitely differentiable and smooth. These have been used extensively for image processing applications because of these useful mathematical properties.⁴⁶ These functions also diminish rapidly with distance such that a cut-off distance based on the amplitude becoming comparable with computational noise is practical. We also note that the Gaussian function arises from a Maximum Entropy argument as the least-biased kernel used for interpolation in mesh-free continuum mechanics simulations.^{47, 48} The explicit form of the normalized, isotropic kernel used in this work is given in eq. 1 below.

$$w_b(\mathbf{r}) = \frac{1}{(2\pi)^{3/2}\sigma^3} \exp\left(-\frac{|\mathbf{r}_b - \mathbf{r}|^2}{2\sigma^2}\right) \quad (1)$$

This is defined with respect to the position of the b^{th} atom, \mathbf{r}_b , where \mathbf{r} is a general coordinate in space and σ is the width of the Gaussian which has units of length. The kernel function itself, w_b , has units of 1/volume. The integral of this normalized function over all space simply equals 1. This expression is used to define the continuum number density function N (number of atoms per volume) at an arbitrary point in space as shown in eq. 2.

$$N(\mathbf{r}) = \sum_b w_b(\mathbf{r}) = \frac{1}{V_0} \sum_b \exp\left(-\frac{|\mathbf{r}_b - \mathbf{r}|^2}{2\sigma^2}\right) \quad (2a)$$

Here, because all of the atoms are the same type, we assume the length scale σ to be independent of the atomic identities and factor out a constant scalar volume, V_0 , defined in eq. 2b.

$$V_0 = (2\pi)^{3/2}\sigma^3 \quad (2b)$$

This same approach can be used to define analogous continuum property fields such as mass density, momentum and stress. We now consider defining the Taylor series expansion of the number density in the neighborhood of atom a , as shown in eq. 3 given below:

$$\begin{aligned}
n_a(\mathbf{r}) &= N(\mathbf{r}_a + \Delta\mathbf{r}) \\
&\approx N(\mathbf{r}_a) + \Delta\mathbf{r} \odot \left. \frac{\partial N}{\partial \mathbf{r}} \right|_{\mathbf{r}_a} + \frac{1}{2} (\Delta\mathbf{r} \otimes \Delta\mathbf{r}) \odot \left. \frac{\partial^2 N}{\partial \mathbf{r}^2} \right|_{\mathbf{r}_a} + \dots
\end{aligned} \quad (3)$$

This expression is written in tensor form, where the terms associated with the n^{th} derivative are a rank n tensor of dimension 3. The general three-dimensional coordinate $\mathbf{r} = [x, y, z]$ is redefined in terms of a small displacement $\Delta\mathbf{r}$ with respect to the chosen central position of \mathbf{r}_a . The symbol \otimes designates the vector outer product where $\Delta\mathbf{r} \otimes \Delta\mathbf{r}$ is a rank 2 tensor of dimension 3 (or the 3x3 matrix T_{ij}), and the next term in the sequence, $\Delta\mathbf{r} \otimes \Delta\mathbf{r} \otimes \Delta\mathbf{r}$, is a rank 3 tensor of dimension 3 (or the 3x3x3 array T_{ijk}). The symbol \odot indicates the scalar product (total contraction) between two rank n tensors.

In general, the n^{th} order derivatives of the atomic number density can then be written as in eq. 4.

$$\left. \frac{\partial^n N}{\partial \mathbf{r}^n} \right|_{\mathbf{r}_a} = \sum_b \left. \frac{\partial^n w_b}{\partial \mathbf{r}^n} \right|_{\mathbf{r}_a} = \frac{1}{V_0 \sigma^n} \sum_b w_b(\mathbf{r}_a) \mathbf{H}_n \left(\frac{\mathbf{r}_{ab}}{\sigma} \right) = \frac{1}{V_0 \sigma^n} \sum_b w_{ab} \mathbf{H}_n \left(\frac{\mathbf{r}_{ab}}{\sigma} \right) \quad (4)$$

Here, \mathbf{H}_n is defined as the n^{th} order tensor formulation of the Hermite polynomial expressions,⁴⁹ which arise from taking the derivatives of the Gaussian function. These formulations can also be expanded out in terms of polynomial combinations of the individual Cartesian components as outlined in eq. 5, where the terms would comprise elements of the general Cartesian tensors written above.

$$\left. \frac{\partial^n N}{\partial x^p \partial y^q \partial z^s} \right|_{\mathbf{r}_a} = \frac{1}{\sigma^n} \sum_b w_{ab} (x_b - x_a)^p (y_b - y_a)^q (z_b - z_a)^s \quad (5)$$

Here p, q, s are all non-negative integers and $p + q + s = n$. These define the general set of harmonic polynomials, where the Hermite polynomials are a subset of that class. Multiplying the Hermite polynomials by factors of r^{2m} , with $m = 0, 1, 2, \dots$ would then span the range of harmonic polynomials.

The individual terms in eq. 3 can then be evaluated by substituting in the definition in eq. 2a. The first term for the local density given by equation 2a, with $\mathbf{r} = \mathbf{r}_a$. The subsequent terms (derivatives), given through fourth order, take the following forms:

$$\left. \frac{\partial N}{\partial \mathbf{r}} \right|_{\mathbf{r}_a} = \sum_b \left. \frac{\partial w_a}{\partial \mathbf{r}} \right|_{\mathbf{r}_b} = -\frac{1}{V_0} \sum_b \frac{\mathbf{r}_{ab}}{\sigma^2} \exp\left(-\frac{|\mathbf{r}_b - \mathbf{r}_a|^2}{2\sigma^2}\right) = -\frac{1}{\sigma} \sum_b \frac{\mathbf{r}_{ab}}{\sigma} w_{ab} \quad (6a)$$

$$\begin{aligned}
\left. \frac{\partial^2 N}{\partial \mathbf{r}^2} \right|_{\mathbf{r}_a} &= \sum_b \left. \frac{\partial^2 w_a}{\partial \mathbf{r}^2} \right|_{\mathbf{r}_b} = \frac{1}{\sigma^4} \sum_b (\mathbf{r}_{ab} \otimes \mathbf{r}_{ab} - \sigma^2 \mathbf{I}_2) w_{ab} \\
&= \frac{1}{\sigma^4} \sum_b \left(\mathbf{r}_{ab} \otimes \mathbf{r}_{ab} - \frac{\sigma^2}{r_{ab}^2} [\mathbf{r}_{ab} \otimes \mathbf{r}_{ab}]_s \right) w_{ab}
\end{aligned} \quad (6b)$$

$$\begin{aligned}
\left. \frac{\partial^3 N}{\partial \mathbf{r}^3} \right|_{\mathbf{r}_a} &= \sum_b \left. \frac{\partial^3 w_a}{\partial \mathbf{r}^3} \right|_{\mathbf{r}_b} \\
&= -\frac{1}{\sigma^6} \sum_b \left(\mathbf{r}_{ab} \otimes \mathbf{r}_{ab} \otimes \mathbf{r}_{ab} - \frac{\sigma^2}{r_{ab}^2} [\mathbf{r}_{ab} \otimes \mathbf{r}_{ab} \otimes \mathbf{r}_{ab}]_s \right) w_{ab}
\end{aligned} \tag{6c}$$

$$\begin{aligned}
\left. \frac{\partial^4 N}{\partial \mathbf{r}^4} \right|_{\mathbf{r}_a} &= \sum_b \left. \frac{\partial^4 w_a}{\partial \mathbf{r}^4} \right|_{\mathbf{r}_b} \\
&= \frac{1}{\sigma^8} \sum_b \left(\mathbf{r}_{ab} \otimes \mathbf{r}_{ab} \otimes \mathbf{r}_{ab} \otimes \mathbf{r}_{ab} - \frac{\sigma^2}{r_{ab}^2} [\mathbf{r}_{ab} \otimes \mathbf{r}_{ab} \otimes \mathbf{r}_{ab} \otimes \mathbf{r}_{ab}]_s \right. \\
&\quad \left. + \frac{\sigma^4}{2r_{ab}^4} [[\mathbf{r}_{ab} \otimes \mathbf{r}_{ab} \otimes \mathbf{r}_{ab} \otimes \mathbf{r}_{ab}]_s]_s \right) w_{ab}
\end{aligned} \tag{6d}$$

In these equations, w_{ab} denotes the function $w_b(\mathbf{r})$ evaluated at $\mathbf{r} = \mathbf{r}_a$ and $[M]_s$ denotes the symmetric trace of tensor M where the trace has been expanded back into the full rank order of the initial tensor M . For example, the trace of a 3x3 matrix (e.g. eq 6b) is a simple scalar, and the reconstituted symmetric trace tensor is that scalar times the 3x3 identity matrix. This follows the approach of Coope, et al.⁵⁰ and Jerphagnon, et al.³⁰ in terms of expressing a rank n dimension 3 tensor in terms of its irreducible spherical components. Further details of the manipulations are given in the Supplemental Material, along with the definitions of the symmetric trace tensors. Note that the summations are over all atoms b , including $b = a$. For the expressions as written, the latter terms would simply be zero and there are no mathematical complications. For some applications, it would be more advantageous to evaluate these expansions about a position $\mathbf{r}_A \approx \mathbf{r}_a$ where \mathbf{r}_A is defined as the center of position or mass of the neighborhood associated with atom a . The expressions above can be smoothly adopted to such a transformation.

The terms are directly interpretable. The number density at the position of the a^{th} atom depends upon how many other atoms are in its neighborhood, with a Gaussian weight that depends upon the distances to the other atoms $\mathbf{r}_{ab} = \mathbf{r}_b - \mathbf{r}_a$, eq 2a with $\mathbf{r} = \mathbf{r}_a$. Properties of the Gaussian become quite useful in defining the subsequent derivatives: the derivative of the Gaussian is the product of the scaled vector contained in the argument times the original Gaussian. This recursive property greatly simplifies how the derivative functions are expressed. The right-most term in eq. 6a emphasizes that, by using the Gaussian kernel, the first derivative can be simply related to the Gaussian-weighted sum of the vector distances to the atoms of the system. Consequently, *the gradient of the number density is equivalent to the first order moment of the spatial distribution of the atomic positions* in this Gaussian-weighted neighborhood. In addition, Gaussian weighting functions enable ready access to the higher order derivatives that cannot be achieved with either discrete or low order polynomial neighborhoods.

The second derivative is given in eq 6b. Considering just the first term in the parentheses in eq. 6b, this contains the second order moment of the spatial distribution of the atomic

positions in this neighborhood. This can be related to the second order strain and measures the amounts of uniaxial and shear deformations. The subtraction of the identity matrix basically modifies the trace of the matrix so that the resulting expression has different effective weights for the deviatoric components, which measure the change in shape of the local neighborhood, versus the trace which measures the level of volumetric strain, i.e. change in size. This difference in weighting depends upon the original choice of the weighting function and is also tied to making the subsequent moment expressions orthogonal to one another.

The expressions for the third and fourth derivatives are given in eqs. 6c and 6d, respectively. Overall, these are symmetric rank 3 and rank 4 tensors, respectively. The forms have a structure similar to eq 6b, where there are separate terms based on the traces of highest order tensor. This suggests a further reduction of transforming all of the tensor expressions to traceless versions, denoted by $[M]_T$, where eqs 6b-d can be rewritten as eqs 7a-c, respectively. Further details are given in Supplemental Material (S.1).

$$\left. \frac{\partial^2 N}{\partial \mathbf{r}^2} \right|_{\mathbf{r}_a} = \frac{1}{\sigma^4} \sum_b \left([\mathbf{r}_{ab} \otimes \mathbf{r}_{ab}]_T - \left\{ \frac{\sigma^2}{r_{ab}^2} - \frac{1}{3} \right\} [\mathbf{r}_{ab} \otimes \mathbf{r}_{ab}]_S \right) w_{ab} \quad (7a)$$

$$\left. \frac{\partial^3 N}{\partial \mathbf{r}^3} \right|_{\mathbf{r}_a} = -\frac{1}{\sigma^6} \sum_b \left([\mathbf{r}_{ab} \otimes \mathbf{r}_{ab} \otimes \mathbf{r}_{ab}]_T - \left\{ \frac{\sigma^2}{r_{ab}^2} - \frac{1}{5} \right\} [\mathbf{r}_{ab} \otimes \mathbf{r}_{ab} \otimes \mathbf{r}_{ab}]_S \right) w_{ab} \quad (7b)$$

$$\begin{aligned} & \left. \frac{\partial^4 N}{\partial \mathbf{r}^4} \right|_{\mathbf{r}_a} \\ &= \frac{1}{\sigma^8} \sum_b \left([\mathbf{r}_{ab} \otimes \mathbf{r}_{ab} \otimes \mathbf{r}_{ab} \otimes \mathbf{r}_{ab}]_T - \left\{ \frac{\sigma^2}{r_{ab}^2} - \frac{1}{7} \right\} [[\mathbf{r}_{ab} \otimes \mathbf{r}_{ab} \otimes \mathbf{r}_{ab} \otimes \mathbf{r}_{ab}]_S]_T \right. \\ & \left. + \left\{ \frac{\sigma^4}{2r_{ab}^4} - \frac{\sigma^2}{3r_{ab}^2} + \frac{1}{30} \right\} [[\mathbf{r}_{ab} \otimes \mathbf{r}_{ab} \otimes \mathbf{r}_{ab} \otimes \mathbf{r}_{ab}]_S]_S \right) w_{ab} \end{aligned} \quad (7c)$$

The final terms of such a reduction cannot be reduced further. For the even-powered derivatives, the final term becomes a scalar, which would be r_{ab}^2 for eq 7a and r_{ab}^4 for eq 7c. For the odd-powered derivatives, the final term depends on a vector of 3 terms, which is $(r_{ab}^2 x_{ab}, r_{ab}^2 y_{ab}, r_{ab}^2 z_{ab})$ for eq 7b. This derivation again follows the approach given by Coope⁵⁰⁻⁵² and Jerphagnon.³⁰ As discussed further below, the individual terms of these polynomial expansions are irreducible Spherical Tensors (ST), which can then also be directly mapped onto angular momentum vectors. These correspond to subspace groups of the rotationally invariant space symmetry group SO(3). Very similar expressions would be derived for any other spherically symmetric weighting function besides a Gaussian, such as a simple exponential decay (which occurs in the definition of atomic orbitals). The difference would lie only in the terms in the curly brackets in eqs 7a-c, which define where radial nodes would occur that define the orthogonality for closely related subspaces. If finite n th-order polynomials were used as the weighting functions, the moments would vanish for orders $> n$. The use of polynomial spline functions would have similar issues.

The angular dependence, captured in the ST, is independent of the spherically-symmetric radial function. At the top level, this is a restatement that any physics problem that involves a radially symmetric field can be separated into radial and angular components, where the latter can usually be succinctly expressed in terms of spherical harmonic functions. We wish to emphasize a deeper level here where the radial node pattern supplies an additional partitioning into the SO(3) subspaces.

2.2. Transformation of Cartesian moments to rotationally invariant descriptors

While complete, recognizing the shapes or deformations expressed in Cartesian moments is difficult and only works well when the coordinate axes happen to be aligned with any symmetry axes of the system. To simplify this, the Cartesian moments can be recast into expressions based on spherical harmonics, which can then be re-expressed in a rotationally invariant format. Both Jerphagnon, et al.³⁰ and Lo and Don²⁸ have shown how to transform the harmonic polynomial terms (eq 5) into spherical harmonic expressions, where their approaches follow the algebra of angular momentum.²⁹ The first step in this process is to linearly transform the Cartesian moments into the regular solid harmonic polynomials, $R_{l(n)}^m$, defined in eq. 8.

$$R_{l(n)}^m = \tilde{r}^{n-l} \tilde{r}^l Y_l^m = \left(\frac{r}{\sigma}\right)^n Y_l^m \quad (8)$$

Here, \tilde{r} is the scaled magnitude of the distance, r is the magnitude of the vector \mathbf{r} , σ is the scale factor from the Gaussian weighting process, n is the overall order of the polynomial, l is the overall order of the harmonic polynomial, and Y_l^m is the standard spherical harmonic function defined in their standard complex form. The constraints on the integer indices are that $n \geq 0$; $l = n, n-2, \dots, \geq 0$; $m = -l, -l+1, \dots, l-1, l$. We emphasize that the while Y_l^m functions have no dependence on distance, but only on direction, the $R_{l(n)}^m$ functions do have an explicit radial dependence of $\left(\frac{r}{\sigma}\right)^n$, in addition to the angular dependence. Thus, this approach supplants the need to build-in further radial dependence or the use of hyper-spherical harmonics.^{17,27}

The complex moments about atom a are then defined in eq. 9.

$$v_{l(n)}^m(a) = \sum_b R_{l(n)}^m(\mathbf{r}_{ab}) w_{ab} \quad (9)$$

These $v_{l(n)}^m$ terms, which are complex, have the same indices as the solid harmonic polynomials and have the same behavior as angular momentum functions. These terms contain the information of the moment tensors expressed in this solid harmonic basis and are called Spherical representations of the irreducible moment tensors²⁷ or simply as Spherical Tensors (ST).³⁰ Each of the irreducible tensors in eqs 7a-c can then be directly mapped onto the ST as shown in Table I. This basis facilitates defining both rotational invariant descriptors and orientation functions.

Table I. Mapping between the irreducible moment tensors (IMT) and spherical tensors (ST). The final column gives the degrees of freedom (DOF) for the tensors.

IMT	ST	DOF
\mathbf{r}_{ab}	$\mathbf{v}_{1(1)}$	3
$[\mathbf{r}_{ab} \otimes \mathbf{r}_{ab}]_T$	$\mathbf{v}_{2(2)}$	5
$[\mathbf{r}_{ab} \otimes \mathbf{r}_{ab}]_S$	$\mathbf{v}_{0(2)}$	1
$[\mathbf{r}_{ab} \otimes \mathbf{r}_{ab} \otimes \mathbf{r}_{ab}]_T$	$\mathbf{v}_{3(3)}$	7
$[\mathbf{r}_{ab} \otimes \mathbf{r}_{ab} \otimes \mathbf{r}_{ab}]_S$	$\mathbf{v}_{1(3)}$	3
$[\mathbf{r}_{ab} \otimes \mathbf{r}_{ab} \otimes \mathbf{r}_{ab} \otimes \mathbf{r}_{ab}]_T$	$\mathbf{v}_{4(4)}$	9
$[[\mathbf{r}_{ab} \otimes \mathbf{r}_{ab} \otimes \mathbf{r}_{ab} \otimes \mathbf{r}_{ab}]_S]_T$	$\mathbf{v}_{2(4)}$	5
$[[\mathbf{r}_{ab} \otimes \mathbf{r}_{ab} \otimes \mathbf{r}_{ab} \otimes \mathbf{r}_{ab}]_S]_S$	$\mathbf{v}_{0(4)}$	1

There are $2l+1$ components for each order l of the $\mathbf{v}_{l(n)}$ vectors, and they can be generally written as a complex vector as shown in eq 10.

$$\mathbf{v}_{l(n)} = \{v_{l(n)}^l e^{-il\omega_l}, v_{l(n)}^{l-1} e^{-i(l-1)\omega_{l-1}}, \dots, v_{l(n)}^{l-1} e^{+i(l-1)\omega_{l-1}}, v_{l(n)}^l e^{+il\omega_l}\} \quad (10)$$

Here the $l+1$ $v_{l(n)}^m$ coefficients ($0 \leq m \leq l$) are real quantities which define the magnitude of the m -th component, and the l ω_m angles ($1 \leq m \leq l$) are the phase angles that define the complex terms (the ω_0 angle is zero because that term has no dependence on the rotation about the z axis). This defines the $2l+1$ number of degrees of freedom that uniquely define these vectors / ST in a fixed frame. An alternative method for expressing this vector is to resolve all the complex components into real expressions by appropriate addition / subtraction of conjugate components as below. Such formulations are generally referred to as Real Spherical Harmonics, and the tilde is added to signify that the magnitude has been modified by $\sqrt{2}$.⁵³

$$\tilde{v}_{l(n)}^{mc} = \frac{1}{i^m \sqrt{2}} (v_{l(n)}^m e^{-im\omega_m} - v_{l(n)}^m e^{+im\omega_m}) = \tilde{v}_{l(n)}^m \cos(m\omega_m) \quad (11a)$$

$$\tilde{v}_{l(n)}^{ms} = \frac{1}{i^m \sqrt{2}} (v_{l(n)}^m e^{-im\omega_m} + v_{l(n)}^m e^{+im\omega_m}) = \tilde{v}_{l(n)}^m \sin(m\omega_m) \quad (11b)$$

The real spherical tensor is then generally written as in eq 12.

$$\tilde{\mathbf{v}}_{l(n)} = \{\tilde{v}_{l(n)}^0, \tilde{v}_{l(n)}^1 \cos(\omega_1), \tilde{v}_{l(n)}^1 \sin(\omega_1), \dots, \tilde{v}_{l(n)}^l \cos(l\omega_l), \tilde{v}_{l(n)}^l \sin(l\omega_l)\} \quad (12)$$

We illustrate these functions in Figure 1. In the left half of the figure are shown representative solid harmonic functions $R_{l(n)}^m$ which have positive (red) and negative (blue) phases. Their appearance is very similar to typical atomic orbital representations (p , d , f and g orbitals for $l = 1, 2, 3$ and 4 , respectively) which would have an exponential decay in density with distance compared to the Gaussian damping used here. These show the density changes that would result for that type of deformation. Also included in the figure

are the Schoenflies notation for the point group that describes the symmetry of deformation.⁵⁴ In the right half of the figure are shown the density distributions that would result from applying those changes to a spherically symmetric Gaussian density. The red regions show where density has been added and the blue regions show where density has been removed. For example, the case of $l=2$ and $m=0$ in Fig 1B would correspond to a uniaxial shear (tetragonal distortion, $a \neq b = c$) along the vertical (z) axis. Neighboring atoms have been brought in closer along the z axis, but pushed further away in the xy plane. The $l=2$ and $m=1,2$ distortions show shear strains where the neighborhoods are compressed along one axis, expanded along a perpendicular axis, but left undistorted along the third perpendicular axis (orthorhombic distortion, $a \neq b \neq c$). Thus, the $m=0$ distortion results in a cylindrically symmetric geometry ($D_{\infty h}$), while the $m=1,2$ distortions result in a lower symmetry brick-like geometry (D_{2h}). The deformations represented in the $l=2$ terms can be directly mapped to strain tensors defined in mechanics literature. These are described in the supplemental material (S.2).

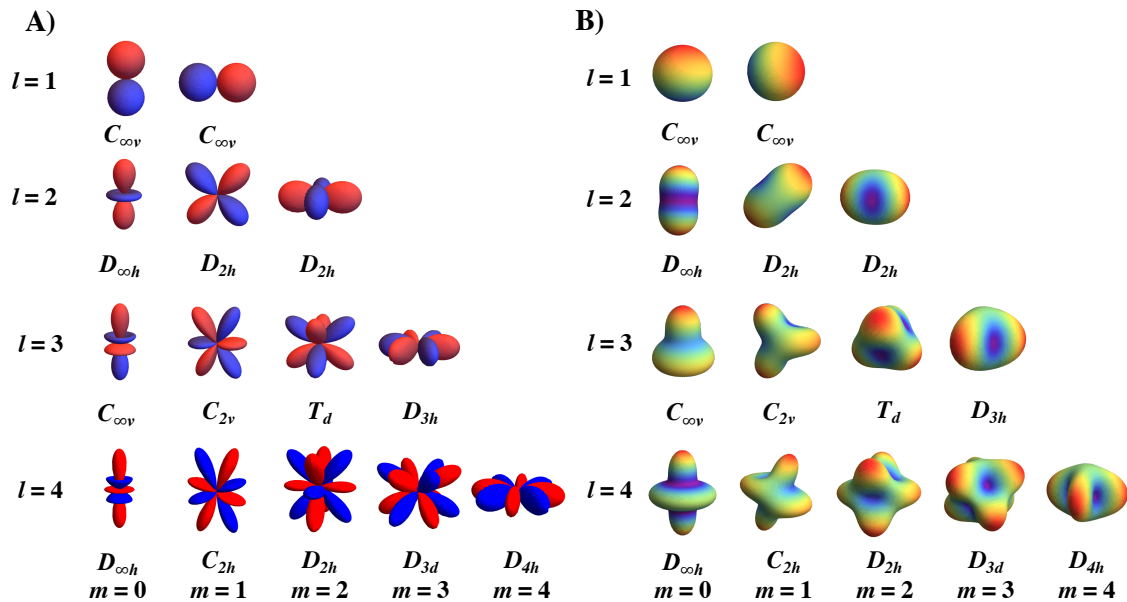


Figure 1. Comparison plot of the solid harmonic basis functions and the resulting density deformations. A) Illustrative solid harmonic basis functions, $R_{l(n)}^m$, for $l=n=1-4$, and for $0 \leq m \leq l$. The surfaces are drawn for an isodensity surface and are colored as red for a positive phase and blue for a negative phase. The vertical axis is the z direction, the x axis points to the right, and with the y axis projecting into the plane of the page. The structures have been slightly rotated and tilted to add perspective. The corresponding functions for $-l \leq m \leq -1$ would be obtained by rotating the positive analogs by $\pi/2m$ radians about the vertical (z) axis. B) Illustrative density deformation plots $l=n=1-4$ and for $0 \leq m \leq l$. These were generated by adding $1/2$ of the functions on the left to a spherically symmetric Gaussian distribution: $[1 + \frac{1}{2}R_{l(n)}^m] \exp\left(-\frac{r^2}{2\sigma^2}\right)$. The surfaces are drawn for an isodensity surface and are colored by how far that surface is from the central point: red for the farthest distance, blue for the closest. Thus, the color simply accentuates the surface plot

to highlight where density has been added (red) and depleted (blue). Also included are the Shoenflies notation for the point group of the deformation.

Clebsch-Gordan coupling. The second step in the process is to derive rotationally invariant descriptors from these $v_{l(n)}^m$ terms. This is done using the Clebsch-Gordan (CG) coupling procedure which defines the addition or coupling process between two angular momentum vectors.²⁹ While this is normally thought of as a quantum mechanical process for coupling between the spin of an electron and its orbital angular momentum (see ref 55 for example)⁵⁵, when only integer spins are involved this describes classical angular momentum processes as well. As shown below, rotational symmetry axes are directly identified by their application.

One can somewhat arbitrarily take the product between any two ST (or between an ST and itself) by the expression in eq. 13.

$$N[l_1(n_1), l_2(n_2)]_h^k = \sum_{m=-l}^{m=l} \langle l_1, m, l_2, k - m | l_1, l_2, j, k \rangle v_{l_1(n_1)}^m v_{l_2(n_2)}^{k-m} \quad (13)$$

The N terms are the components of the ST \mathbf{N} of rank h that results from the CG procedure and $|k| \leq h$. The terms in the brackets $\langle \rangle$ are the CG coefficients which specify how different terms are coupled, where there are somewhat restrictive rules as to which terms are allowed to combine. We particularly note the restriction that only values of $h = |l_1 - l_2|, |l_1 - l_2 + 2|, \dots, |l_1 + l_2 - 2|, |l_1 + l_2|$ have non-zero coefficients. Notice that there is no explicit dependence of the CG coefficients on the (n_1, n_2) values in these expressions, only the (l, m) values. For the cases where $l = n$, we will subsequently drop the n label to simplify the notation.

The resulting vectors $\mathbf{N}[l_1, l_2]_h$ have the same type of angular momentum properties as the initial vectors, and contain $2h+1$ terms which could be specifically identified by the superscript k . These were called “composite” vectors by Lo&Don, where the original definition of the CG coefficients came from the addition or coupling of two angular momentum vectors. Given the uncertainty in the relative directions of those vectors, the CG coefficients define the probability that some desired product vector would be observed from that coupling procedure. This gives rise to a different set of normalizations constants compared to other treatments of vector or matrix manipulations. Further additions between these “composite” vectors and the original vectors can also be formed. As such, there are an unlimited number of such contractions that can be formed. For the case where $h = 0$ (and implicitly $k = 0$), a scalar (zeroth rank tensor) results which then has no angular dependence. These terms contain the desired rotational invariance properties required to describe the geometries in a coordinate independent frame. That is, these expressions provide direct algebraic links back to the initial vector compositions and thus provide a pathway by which those compositions can be determined.

Unfortunately, there are still an unlimited number of such contractions that can be formed. The approach of Moment Tensor Potentials (MTP)²² relies on formulating an extensive list

of such invariants, and then using Machine Learning methods to formulate a potential function based on this large list.³⁵ Such an approach is suggested by earlier expressions for moment expansions which were written in a manner that could suggest that there is an infinite expansion of moments required to capture a particular l -th order spherical harmonic term (see eq 3.3 in ref 6).⁶ However, as noted above, each l -th rank ST contains only $2l+1$ degrees of freedom (DOF). As such, it should be possible to find a combination of $2l+1$ invariant terms that capture that information, and any additional invariants would represent only redundant information. It is presumed that the simplest invariants that achieve this would be preferable over more complex expressions. That is the critical aspect of this work and we shall now describe an approach for finding these terms. Within the ST framework, it also works out that these terms have rather direct physical interpretations.

The first step in this process is to recognize that the ST are initially expressed in an arbitrary frame. By rotating that frame appropriately, various terms of the vector can be zeroed out.⁵³ In fact, it is always possible to cause three of the terms to become zero. That is, 3 of the initial $2l+1$ DOF of the arbitrary oriented tensor can be recast as the 3 rotation angles that would define the tensor in a more desirable orientation. The remaining $2l-2$ DOF then would describe the shape of that rotated tensor in a fewer number of terms. (The exception to this is $l=1$ which defines a vector. In that case, only 2 angles are required to describe the orientation and the remaining invariant is the magnitude of the vector.) There are options as to which terms can be zeroed out. Our preferred option, the reasons for which will become fully apparent below, is to zero out the two $m=l$ terms and the second $m=l$ term. The resulting form of the vectors is shown in eq 14 below, where the rotation matrix to achieve this is discussed in Appendix A. The three DOF that have been eliminated by this process are $\tilde{\nu}_{l(n)}^1$, ω_1 , and ω_l . As the $m=l$ terms are the lowest symmetry components of the expansion (see Figure 1), their elimination enables a more ready appreciation of the symmetry of the tensor. We refer to this as the High Symmetry (HS) orientation. This transformation aligns the internal \bar{z} axis with the l -th order rotation axis, and the internal \bar{x} axis defines the orientation of the $m=l$ component. The resulting magnitudes of the other terms will be altered by this rotation which is noted by the changing the labels from $\bar{\nu}$ to μ . The rotation angles are also altered in the process such that $m\bar{\omega}_m = m\omega_m - l\omega_l$, hence the addition of a bar accent to those terms.

$$\boldsymbol{\mu}_{l(n)} = \{\mu_{l(n)}^0, 0, 0, \mu_{l(n)}^2 \cos(2\bar{\omega}_2), \mu_{l(n)}^2 \sin(2\bar{\omega}_2), \dots, \mu_{l(n)}^l, 0\} \quad (14)$$

Rank 0 and 1 terms. First, we consider the rank 1 tensors. These are simply vectors and are somewhat an exception to the rules we will subsequently use. There is one invariant for this class which simply the norm of the vector, which is defined in the CG sense below:

$$N[1,1]_0 = \frac{1}{\sqrt{3}} \{(\tilde{\nu}_1^0)^2 + (\tilde{\nu}_1^1)^2\} = \frac{1}{\sqrt{3}} (\mu_1^0)^2 \quad (15)$$

The results are defined in both the initial unrotated frame ($\tilde{\nu}_l^m$), and in the HS orientation (μ_l^m). In the original Cartesian notation, the term in the curly brackets would simply correspond to $\{z^2 + (x^2 + y^2)\}$, where x , y and z are the Cartesian elements of the vector.

In the rotated frame, only μ_1^0 would be non-zero (and aligned with \bar{z}), and two angles would describe the orientation of that axis with respect to the original frame.

We note that the CG normalization factors are different from the normal Cartesian definitions, where these had been defined to achieve a unitary sum of possible combinations of the angular momentum vectors. These factors are scalars of order 1, $\sim O(1)$, and do not otherwise impact the results, so we do not correct for them. It is appropriate to normalize the invariants by the Gaussian-weighting factors though and convert them into unitless quantities. The first invariant of our overall expansion comes from the zeroth order term which is simply the sum of weights:

$$P0I0(a) = V_0 * N(\mathbf{r}_a) = V_0 * \sum_b w_{ab} = \sum_b \exp\left(-\frac{|\mathbf{r}_b - \mathbf{r}_a|^2}{2\sigma^2}\right) \quad (16)$$

The label P indicates that this comes from the positions of the atoms, where similar metrics could be defined for other atomic quantities (e.g. velocity, force, etc.). This *P0I0* term is a density metric which has been normalized by the reference volume. The second invariant then comes from the rank 1 tensor which then is normalized by this first term:

$$P1I0(a) = \frac{\sqrt{N[1,1]_0}}{P0I0(a)} \quad (17)$$

By taking the square root of this invariant, the term is properly normalized by dividing by *P0I0*, rather than its square. And, although the term is unitless, this effectively scales its units as being in terms of $(r/\sigma)^l$ with $l=1$. This pattern will be followed for the subsequent invariants.

Rank 2 terms. Next, we consider the rank 2 tensors, which have previously been considered in a similar context by Kindlman^{31, 32} and Lo&Don.²⁸ Starting with a symmetric 3x3 matrix, it is well-known that these can be characterized by 3 invariants. The first of these is the trace of matrix, which is also the average of the eigenvalues of that matrix. In the current context, this corresponds to a separate subspace, which can be characterized by the scalar below:

$$v_{0(2)}^0(a) = \sqrt{\frac{2}{3}} \sum_b \left(\frac{r_{ab}^2}{\sigma^2}\right) w_{ab} \quad (18)$$

This term nominally characterizes the $\langle r^2 \rangle$ value of the neighborhood. This would correspond to the pressure element of the stress tensor or the change in volume element of the strain tensor. These elements then have a separable mechanical response compared to the deviatoric stress/strain elements.

The second invariant of the rank 2 tensor is then the norm of the v_2^m vector defined below:

$$N[2,2]_0 = \frac{1}{\sqrt{5}} \{(\tilde{v}_2^0)^2 + (\tilde{v}_2^1)^2 + (\tilde{v}_2^2)^2\} = \frac{1}{\sqrt{5}} \{(\mu_2^0)^2 + (\mu_2^2)^2\} \quad (19)$$

In the general orientation, this is simply the sum of the magnitudes of the three component terms. In the special HS orientation, this reduces to the sum of the magnitudes of the two possible distortion types, the cylindrically symmetric (tetragonal) μ_2^0 and the orthorhombic μ_2^2 distortion (see Fig 1B, $l=2$). In general matrix theory, this value corresponds to the root mean square (rms) of the difference in the eigenvalues about their mean.³¹ This measures how asymmetric the matrix is and is analogous to the von Mises stress/strain metrics.

The third invariant of the rank 2 tensor is found by the procedure of Lo & Don:²⁸ first, the rank 2 outer product of the v_2^m vector with itself is formed, and then this is contracted with the original vector. This is given in eq 17 below.

$$\begin{aligned}
& N[N[2,2]_2, 2]_0 \\
&= -\sqrt{\frac{1}{70}} \{2(\tilde{v}_2^0)^3 + 3(\tilde{v}_2^0)^2\tilde{v}_2^1 - 6(\tilde{v}_2^2)^2\tilde{v}_2^0 + 3\sqrt{3}(\tilde{v}_2^1)^2\tilde{v}_2^2 \cos(2(\omega_1 - \omega_2))\} \\
&= -\sqrt{\frac{2}{35}} \mu_2^0 \{(\mu_2^0)^2 - 3(\mu_2^2)^2\} \tag{20}
\end{aligned}$$

The expression for this invariant in general coordinates is rather complicated and not readily interpreted. However, in the HS orientation, the expression simplifies considerably and depends primarily on the difference in magnitudes of the two distortion types. In general matrix theory, this quantity measures the skewness or the cubic difference of the eigenvalues about the mean.³¹ This is related to the Tresca stress/strain metrics.

We normalize these invariants in the manner above and define them below

$$P2I0(a) = \frac{\sqrt{N[2,2]_0}}{P0I0(a)} \tag{21}$$

$$P2I1(a) = -\frac{N[N[2,2]_2, 2]_0}{N[2,2]_0 * P0I0(a)} \tag{22}$$

$$P2I2(a) = \frac{v_{0(2)}^0}{P0I0(a)} - \sqrt{\frac{3}{2}} \tag{23}$$

The terms are all defined to effectively have units of $(r/\sigma)^2$, and that the weighting functions are normalized between the numerator and denominator (e.g. the weighting functions appear as the second power in both). In the current derivation, the radial function contains a node (see eq 7a), which gives rise to the offset term in eq 23. This nominally makes this element orthogonal to the other totally symmetric subspace $v_{0(0)}^0$, which is equivalent to the net density function in eq 2a. For the current application (see below), all of these invariants (along with $P1I0$ and $P0I0$) all span a range of several tenths. These normalization scheme therefore represents a nicely balanced basis set for characterizing these geometries.

The interpretation of the second order terms is illustrated in Figure 2, where this is very similar to a previous illustration by Kindlmann.³¹ The $P2I0$ metric, corresponding to the norm of the deviatoric components, quantifies the total amount of the second order distortion away from a spherically symmetric object. This quantity is non-negative and there are no constraints on its magnitude. The $P2I1$ metric quantifies the skewness of that distribution. For a positive value, the structure is elongated along one particular axis (which corresponds to its internal \bar{z} axis) and contracted about equally in the other two directions. For a negative value, it is contracted along one particular axis and elongated about equally in the other two directions. Both of these limits would correspond to a tetragonal distortion, with $a > b = c$ and $a < b = c$, respectively. For a value of $P2I1 = 0$, there is elongation along one axis, contraction along another, with no distortion in the third direction (e.g. an orthorhombic distortion, $a \neq b \neq c$). The magnitude of $P2I1$ is constrained by the value of $P2I0$. From eqs 19 and 20, it can be defined that:

$$\frac{N[N[2,2]_{2,2}]_0}{(N[2,2]_0)^{3/2}} = -\frac{P2I1(a)}{P2I0(a)} = \sqrt{\frac{2\sqrt{5}}{7}} \cos 3\psi \quad (24)$$

Thus, one could also consider a ratio between those two moments as a means to characterize the invariants, similar to the approach by Kindlmann.³¹ The definition of ψ can be explicitly defined as $\cos \psi = \mu_2^0 / \sqrt{(\mu_2^0)^2 + (\mu_2^2)^2}$. Here, however, we prefer to keep all of these terms defined in the same dimensional units for a more direct comparison between them. In this form, all of the terms can be interpreted as a net physical displacement from some reference geometry.

The $P2I2$ term is a characterization of the r^2 distribution of the neighborhood. In particular, it characterizes whether the weighted values of r^2 are larger or smaller than $(3/2) \sigma^2$. As such, it represents a metric of the size and distribution of the atomic positions in the neighborhood, as suggested in the figure. While this weighting with a radial node function should make this moment orthogonal to the base density metric of $P0I0$, the unevenness of the distribution of the atomic centers (i.e. there are no atoms that are close to the central atom), results in some correlation between those two terms. However, the inclusion of both terms insures the mathematical completeness of the analysis. These three shape invariants, in combination with three orientation factors to be defined later, cover the original 6 DOF contained in the 3x3 symmetric matrix. As noted by Lo&Don,²⁸ any higher order invariant contractions can be shown to be algebraic combinations of these three shape terms.

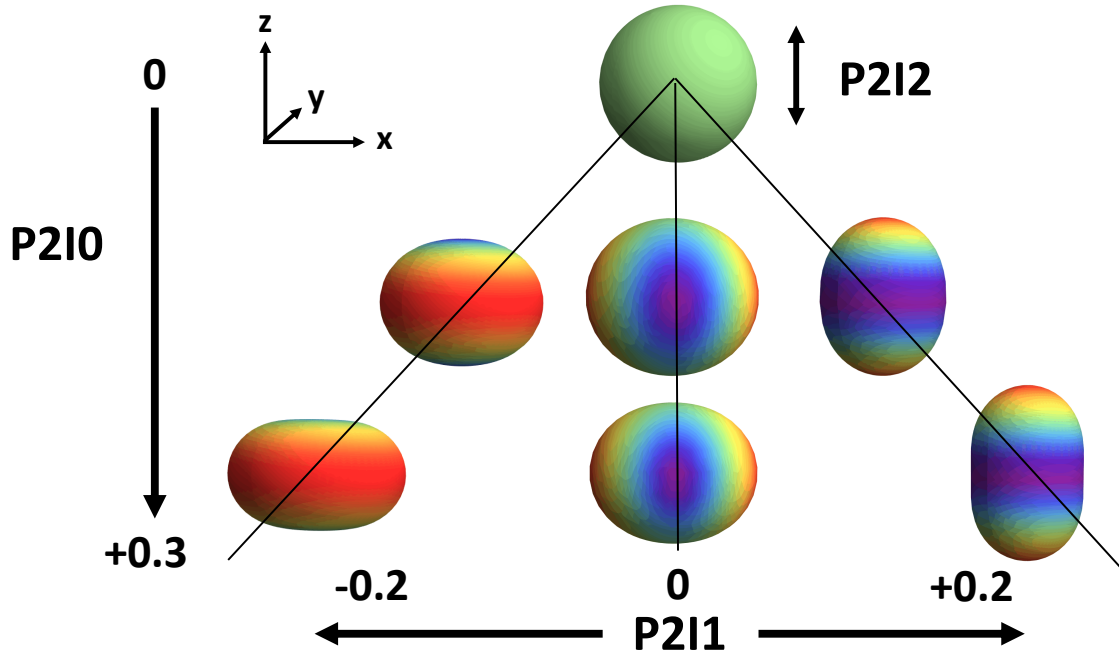


Figure 2. Illustration of the second order Strain Functional Descriptors. The P2I0 quantity measures the net amount of second order distortion. This quantity can have an unlimited positive value, with a value of 0 indicating that there is no second order deformation. The P2I1 quantity measures the skewness character of that second order distortion. A positive value corresponds to a prolate distortion and a negative value corresponds to an oblate distortion, with both tending to structures that cylindrically symmetric about the vertical axis. A value of P2I1 = 0 indicates an asymmetric, orthorhombic distortion. The magnitude of P2I1 is constrained by the value of P2I0. The P2I2 quantity is a measure of the radial size of the object.

Rank 3 terms. Next, the third rank tensor is considered, building off the approach suggested by Lo&Don.²⁸ First, the rank 3 subspace will be examined. The first invariant is readily defined as the norm of the rank 3 spherical tensor defined in eq 25 below.

$$N[3,3]_0 = \frac{1}{\sqrt{7}} \{(\tilde{\nu}_3^0)^2 + (\tilde{\nu}_3^1)^2 + (\tilde{\nu}_3^2)^2 + (\tilde{\nu}_3^3)^2\} = \frac{1}{\sqrt{7}} \{(\mu_3^0)^2 + (\mu_3^2)^2 + (\mu_3^3)^2\} \quad (25)$$

This is the sum of the magnitudes of all of the $l=3$ distortions shown in Figure 1. Similar to $N[2,2]_0$ (eq 19), this measures the net distortion away from spherical symmetry, except now for only the third order terms. For higher order terms, the exploration of higher order rank 3 contractions would seem likely. However, these terms contain no additional information as shown below. The odd contractions are all equal to zero by symmetry (eq 26a), and the even contractions are related to $N[3,3]_0$ (eq 26b). These relationships follow for the similar higher order contractions.

$$N[N[3,3]_3, 3]_0 = 0 \quad (26a)$$

$$N[N[3,3]_3, N[3,3]_3]_0 = A(N[3,3]_0)^2 \quad (26b)$$

Consequently, contractions to other rank orders must then be explored for invariants. The first of these is the norm of the rank 2 contraction. When evaluated in the random orientation, this yields a complicated expression that depends on all seven variables (see Supplemental Material S.3). However, when rotated to the HS configuration, the dependence on the rotation angles disappears and the term depends only on the magnitudes of the components as shown below.

$$\begin{aligned} & N[N[3,3]_2, N[3,3]_2]_0 \\ &= \frac{1}{84\sqrt{5}} \{16(\mu_3^0)^4 + 40(\mu_3^0)^2(2(\mu_3^2)^2 - (\mu_3^3)^2) + 25(\mu_3^3)^2(2(\mu_3^2)^2 + (\mu_3^3)^2)\} \end{aligned} \quad (27)$$

The skewness of the rank 2 contraction can also be calculated like the skewness of the rank 2 tensor above. One constructs the rank 2 composite of the rank 2 composite with itself and then contracts that with the rank 2 composite. The result in the HS configuration is somewhat more complicated than the term above and now depends on the three magnitudes and the one rotation angle $\bar{\omega}_2$, as shown below.

$$\begin{aligned} & N[N[N[3,3]_2, N[3,3]_2]_2, N[3,3]_2]_0 \\ &= -\frac{1}{588\sqrt{30}} \{4(\mu_3^0)^2 - 5(\mu_3^3)^2\} \\ &* \{16(\mu_3^0)^4 - 40(\mu_3^0)^2(6(\mu_3^2)^2 + (\mu_3^3)^2) + 25(\mu_3^3)^2(3(\mu_3^2)^2 + (\mu_3^3)^2)\} \\ &+ \frac{25}{49\sqrt{2}} \mu_3^0(\mu_3^2)^3(\mu_3^3)^2 \cos(6\bar{\omega}_2) \end{aligned} \quad (28)$$

Performing similar higher order self-contractions of the rank 2 contraction generates terms that depend on the lower order contractions as shown below.

$$\begin{aligned} & N[N[N[N[3,3]_2, N[3,3]_2]_2, N[3,3]_2]_2, N[3,3]_2]_0 = \\ & N[N[N[3,3]_2, N[3,3]_2]_2, N[N[3,3]_2, N[3,3]_2]_2]_0 = \frac{2}{7\sqrt{5}} (N[N[3,3]_2, N[3,3]_2]_0)^2 \end{aligned} \quad (29)$$

Hence, there is no further information to be gained along that path of contractions. Next we examine the rank 4 contractions. The norm of the first contraction has a fairly simple form in the HS configuration, similar to that of the rank 2 contraction.

$$\begin{aligned} & N[N[3,3]_4, N[3,3]_4]_0 \\ &= \frac{1}{154} \{12(\mu_3^0)^4 - 24(\mu_3^0)^2((\mu_3^2)^2 - 4(\mu_3^3)^2) + 3(\mu_3^3)^2(2(\mu_3^2)^2 + (\mu_3^3)^2) + 28(\mu_3^2)^4\} \end{aligned} \quad (30)$$

In studying the behavior of these terms in the analysis of MD simulations, it was apparent that there was some direct relationship between this term and the norm of the rank 2 contraction (eq 27). Similar relationships were apparent also with the norm of the rank 6 contraction. Straightforward algebraic manipulations produced the following relationships:

$$(N[3,3]_0)^2 = \frac{15}{7\sqrt{5}}N[N[3,3]_2, N[3,3]_2]_0 + \frac{11}{14}N[N[3,3]_4, N[3,3]_4]_0 \quad (31a)$$

$$(N[3,3]_0)^2 = -\frac{35}{24\sqrt{5}}N[N[3,3]_2, N[3,3]_2]_0 + \frac{11\sqrt{13}}{24}N[N[3,3]_6, N[3,3]_6]_0 \quad (31b)$$

$$(N[3,3]_0)^2 = \frac{7}{22}N[N[3,3]_4, N[3,3]_4]_0 + \frac{3\sqrt{13}}{11}N[N[3,3]_6, N[3,3]_6]_0 \quad (31c)$$

Because of these relationships, it is apparent that the norms of the rank 4 and rank 6 contractions do not contain any independent information compared to that of the rank 2. It is also apparent that the rank 4 term is complementary to the rank 2 (eq 31a); where one is large, the other should be small for the same value of $N[3,3]_0$. From the behavior illustrated in Figure 2, the skewness of the rank 4 term should then carry different information than that of the rank 2. The value for that term in the HS orientation is given below.

$$N[N[N[3,3]_4, N[3,3]_4]_4, N[3,3]_4]_0 = \frac{1}{11858\sqrt{13}} \left\{ \begin{array}{l} -648(\mu_3^0)^6 + 72(\mu_3^0)^4(37(\mu_3^2)^2 + 207(\mu_3^3)^2) \\ -12(\mu_3^0)^2(434(\mu_3^2)^4 + 1263(\mu_3^2)^2(\mu_3^3)^2 - 621(\mu_3^3)^4) + 2744(\mu_3^2)^6 \\ -168(\mu_3^2)^4(\mu_3^3)^2 - 243(\mu_3^2)^2(\mu_3^3)^4 - 81(\mu_3^3)^6 \\ + 3300\sqrt{15} \mu_3^0(\mu_3^2)^3(\mu_3^3)^2 \cos(6\bar{\omega}_2) \end{array} \right\} \quad (32)$$

By zeroing out different combinations of the three magnitude terms, it becomes apparent that the four equations 25, 27, 28 and 32 capture different aspects of the third order shapes. Since there are only 4 DOF for the HS configuration, these invariants are then sufficient to describe that shape space. The skewness of the rank 6 contraction produced a similar, but more complex expansion than eq 32, and the higher order contractions that were examined were found to be repetitive.

Those four invariant terms were then normalized similarly to the second order terms, where the terms are all defined to effectively have units of $(r/\sigma)^3$ and that the weighting functions occur to equal order between the numerator and denominator. The two skewness metrics, P3I2 and P3I3, are normalized with respect to their base functions. The resulting functions then have comparable magnitudes of several tenths and are defined below.

$$P3I0(a) = \frac{(N[3,3]_0)^{1/2}}{P0I0(a)} \quad (33)$$

$$P3I1(a) = \frac{(N[N[3,3]_2, N[3,3]_2]_0)^{1/2}}{(N[3,3]_0)^{1/2} * P0I0(a)} \quad (34)$$

$$P3I2(a) = \frac{N[N[N[3,3]_2, N[3,3]_2]_2, N[3,3]_2]_0}{N[N[3,3]_2, N[3,3]_2]_0 * (N[3,3]_0)^{1/2} * P0I0(a)} \quad (35)$$

$$P3I3(a) = \frac{N[N[N[3,3]_4, N[3,3]_4]_4, N[3,3]_4]_0}{N[N[3,3]_4, N[3,3]_4]_0 * (N[3,3]_0)^{1/2} * P0I0(a)} \quad (36)$$

The significance of the first invariant $P3I0$ is straightforward. It is the net magnitude of the different possible third order distortions shown in Figure 1B for $l=3$. Similar to $P2I0$, it is a non-negative quantity and could be infinitely large, though it samples a fairly small range in the current application. The significance of the other three invariants is illustrated in Figures 3 and 4.

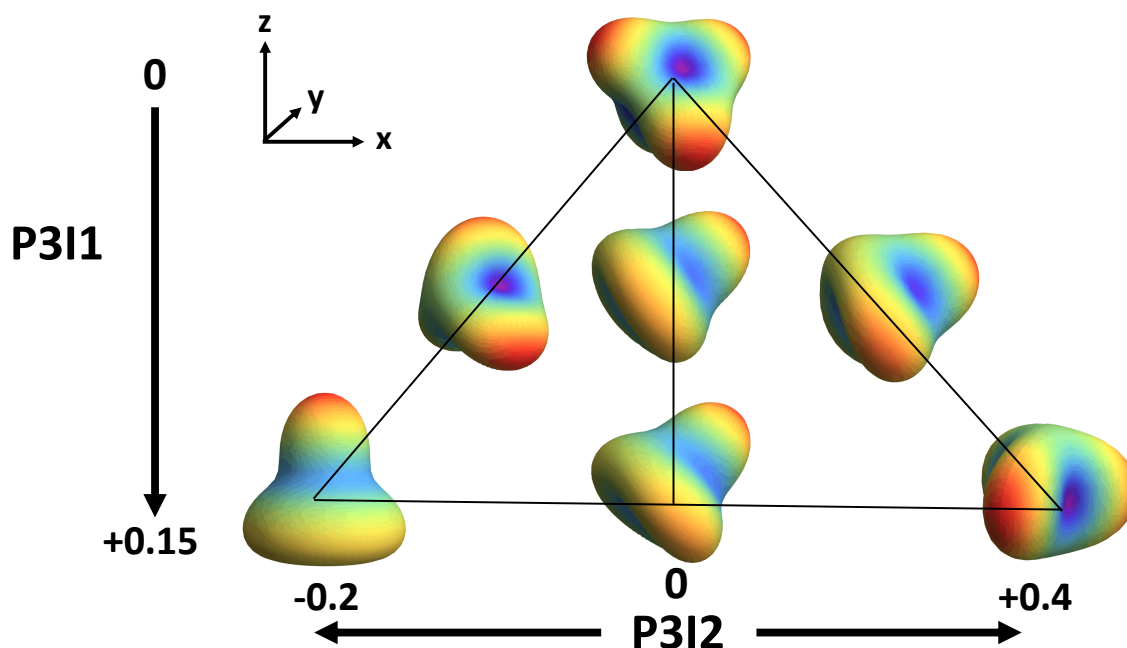


Figure 3. Illustration of the third order Strain Functional Descriptors $P3I1$ and $P3I2$. The $P3I1$ quantity measures the net amount of distortion away from the ideal tetrahedral geometry $T_d \tilde{v}_3^{\pm 2}$. The $P3I2$ quantity measures one of the skewness characteristics of that third order distortion. A positive value corresponds to a flattening distortion of the tetrahedron along one of its C_3 axes to generate the $D_{3h} \tilde{v}_3^{\pm 3}$ structure. A negative value corresponds a smoothing rotation about one of the C_3 axes to generate the bell-shaped $C_{\infty v} \tilde{v}_3^0$. These figures are drawn in the HS frame, with that axis frame shown in the upper left. For the $P3I2$ deformation, the $C_{\infty v}$ and C_3 rotation axes coincide with the internal z axis and the xy plane is defined by the threefold outward extensions of the D_{3h} structure. Note the similarity to the $P2I1$ metric in Figure 2. The magnitudes of the $P3I1$ and $P3I2$ terms will be constrained by the value of the $P3I0$ term.

Figure 3 shows the nature of the $P3I1$ and $P3I2$ invariants. We first note that the magnitudes of these two terms are constrained by the value of the $P3I0$. They have finite ranges limited by that, which has a value of ~ 0.4 for the illustrative figures shown. The $P3I1$ invariant has the notable characteristic that its value is zero for a pure tetrahedral distortion, and its value becomes increasingly positive as the geometry is distorted away from tetrahedral. This can be traced back to the initial definition of the norm of the rank 2 contraction given in equation 27, where it can be seen that if only the μ_3^2 term (tetrahedral distortion) is non-zero, then the equation will be zero. Otherwise, this term is a metric of the non-tetrahedral

distortions to the geometry. In contrast, the norms of the redundant rank 4 (eq 27) and rank 6 (not shown) terms have finite positive values over their complete ranges and lack such a simplistic and direct interpretation. This is one argument for using rank 2 contraction as our primary metric. We particularly note that the tetrahedron is the highest symmetry object (i.e., the most ideal shape) that can be realized for third order distortions.

The $P3I2$ invariant is the primary skewness metric for the $P3II$ distortion which characterizes the nature of the non-tetrahedral distortion. In the negative extreme, the structure becomes the axially symmetric $C_{\infty v} \tilde{\nu}_3^0$ structure, while in the positive extreme the structure becomes the flatter $D_{3h} \tilde{\nu}_3^{\pm 3}$ structure. For a value of $P3I2 = 0$, the structures have a lower symmetry of C_s or C_{2v} . In the Figure, the shapes were drawn in the HS configuration. This emphasizes that the $C_{\infty v}$ axis of the $\tilde{\nu}_3^0$ structure and C_3 axis of the $D_{3h} \tilde{\nu}_3^{\pm 3}$ structure coincide with the internal z axis of the HS structure. Further, the three-fold lobes of the $D_{3h} \tilde{\nu}_3^{\pm 3}$ structure define the xy plane, with one lobe aligned with the x axis. This behavior is very similar to the $P2II$ metric shown in Figure 2, which also derives from a rank 2 skewness metric.

Figure 4 shows the nature of the $P3I2$ and $P3I3$ invariants. We note again that the magnitudes of these two terms are constrained by the value of the $P3I0$ (which is ~ 0.4 for this illustration). As these are both skewness metrics, they can have positive or negative values whose magnitudes would be further constrained by the norms of the base rank 2 and rank 4 contractions (eqs 27 and 30, respectively). At the left of the figure (most negative $P3I3$ values), the character of the $P3I2$ metric as previously described for Figure 3 is apparent. For the most positive $P3I2$ metric (upper left), the structure becomes the $D_{3h} \tilde{\nu}_3^{\pm 3}$ extreme limit, while for the most negative value of $P3I2$ (lower left), the structure limits to the $C_{\infty v} \tilde{\nu}_3^0$ limit. As $P3I3$ then transits to positive values, those characteristics remain dominant as the structures morph to tetrahedral structures. They converge to the ideal tetrahedral structure at $P3I3 \approx +0.4$ (not shown). We also note that C_3 symmetries are apparent for both the most positive and most negative $P3I2$ values. However, for $P3I2 = 0$, there is a lack of C_3 character, and the structures can be best described as having a symmetry plane (C_s) and possibly C_2 symmetries. For a value of $P3I3 = 0$, the structure has only a symmetry plane (C_s) though the structures become C_{2v} for increasingly positive or negative values of $P2I3$. In the vertical direction, the C_s structure morphs towards C_3 symmetry for both positive and negative values of $P2I2$.

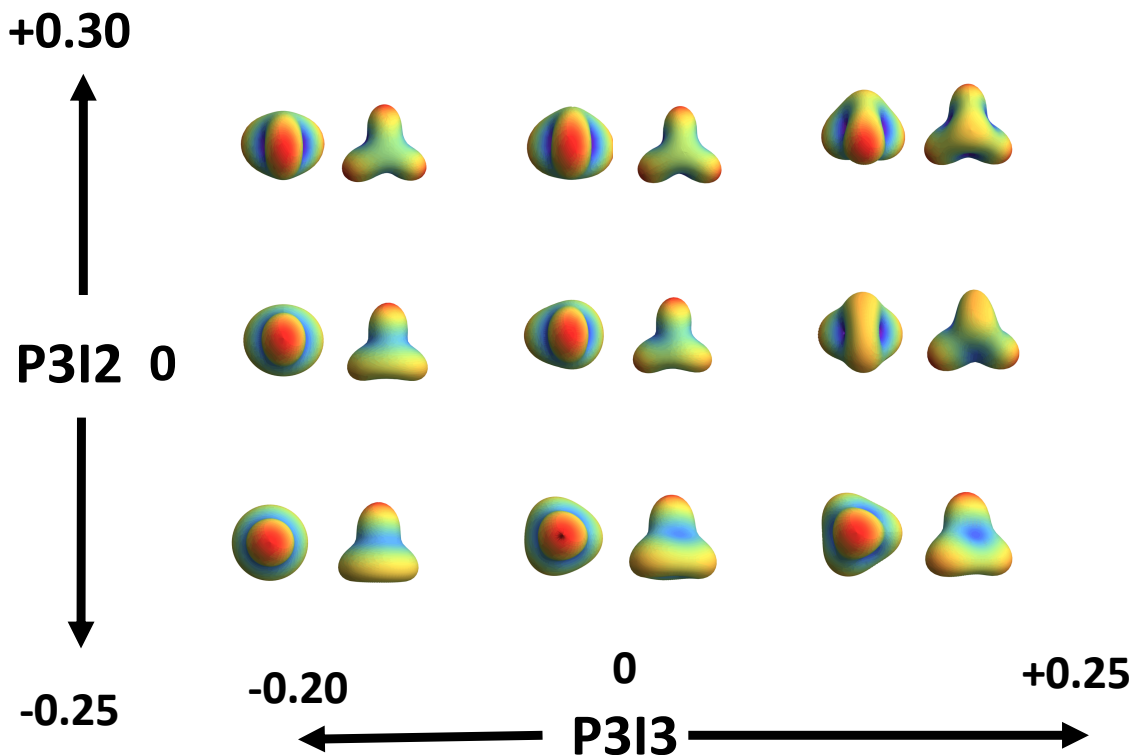


Figure 4. Illustration of the third order Strain Functional Descriptors $P3I2$ and $P3I3$. A total of 9 geometries shown, with two different orthogonal perspectives being shown to fully illustrate the geometries. The pairs are located at roughly their positions in the $P3I2/P3I3$ Cartesian space. The magnitudes of both metrics are constrained by the value of $P3I0$, which is ~ 0.4 for this illustration. Both of these are skewness metrics that characterize the nature of the non-tetrahedral distortion and can have positive or negative values. Note that for the most positive or most negative $P3I2$ values, the structures have identifiable C_3 symmetries. For $P3I2 = 0$ values, the structures have lower symmetries. For $P3I3 = 0$, the symmetry is lowered down to just a symmetry plane C_s structure. As $P3I3$ becomes more positive or negative, the structures acquire C_{2v} character. For the most positive $P3I3$ value (~ 0.4), the structures all converge to the ideal tetrahedron.

The other distortion that arises from the 3rd order terms comes from the $v_{1(3)}^m$ subspace. These terms are dipolar in nature (Figure 1, $l=1$), but with r^3 weighting rather than r^l . The moments can be described with a vector with three independent values. Those can be transformed into one invariant (the magnitude) and two orientation angles. The magnitude is defined analogously to the previous dipole definition as below

$$N[1(3),1(3)]_0 = \frac{1}{\sqrt{3}} \left\{ (\tilde{v}_{1(3)}^0)^2 + (\tilde{v}_{1(3)}^1)^2 \right\} = \frac{1}{\sqrt{3}} (\mu_{1(3)}^0)^2 \quad (37)$$

This is then normalized similar to the other invariants as shown in eq 38.

$$P3I4(a) = \frac{(N[1(3),1(3)]_0)^{1/2}}{P0I0(a)} \quad (38)$$

The units here are then $(r/\sigma)^3$ with equal weighting factors in both the numerator and denominator. This quantity will have a non-negative value whose value is otherwise unconstrained, though in the current application the values are typically several tenths. We note that this term is not constrained by the value of $P3I0$, as are the other three third order invariants, but is completely independent.

These third order shape invariant terms are then analogous to the standard strain gradient terms that are defined for mechanical solids.^{56, 57} This is shown in Figure 5 where we show the comparison between our representation of the Gaussian-weighted deformations and mechanics representations of the strain-gradients.⁵⁶

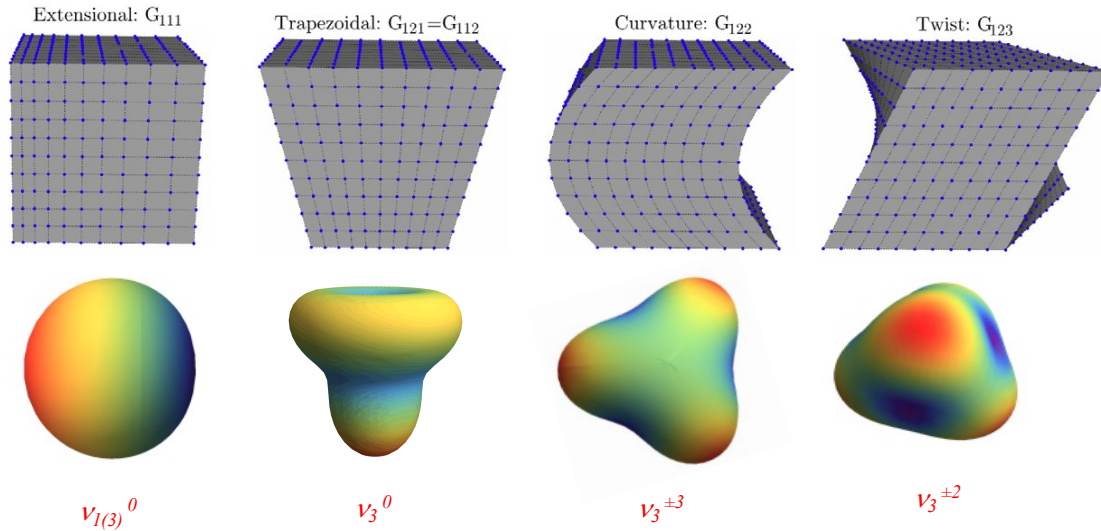


Figure 5. Comparison of strain-gradient visualizations for a finite element simulation (ref 56) and for the current deformations of spheres. The reddish regions of the latter show regions where the density of the material has been increased, and the bluish regions are where the density has been decreased. Alternatively, this can be interpreted as to regions where material has been added / removed.

There is a fair level of correspondence between these basic deformation patterns. For the extensional gradient (first column, A), there is an increased density at one end of the sample, a decreased density at the other, with no gradients in the transverse direction. This is well reproduced by the gradient term captured in $v_{1(3)}^0$. For the trapezoidal distortion (B), there are symmetric transverse gradients which result in an outward expansion of the material at the top and a densification at the bottom similar to the bell-shaped distortion of v_3^0 . For the curvature distortion (C), material is moved forward in the middle of the left, while it is pulled back at the two right corners. This is similar to the trigonal distortion of $v_3^{\pm 3}$. The twist distortion (D) is directly thought of as the twisting a cube. However, it can also be thought of as increasing the density or adding material at alternate corners of the cube and

decreasing the density at the others. This amounts to a tetrahedral distortion of the cube, captured by the $v_3^{\pm 2}$ distortion. The discrepancies partially result from the finite element displacements not being fully orthogonal to one another the way the spherical harmonic representations are. Also, the Gaussian-weighting will foreshorten the displacements as a function of distance from the center while the mechanical representations emphasize those. Still there is a clear correspondence between these deformations. We emphasize that in our current analysis, the extensional strain gradient corresponds to a separate subspace that the other third order displacements. Thus, the mechanics of its displacement should be separable in the same manner that volumetric strain and stress (pressure) should be separable from their deviatoric components.

Rank 4 terms. Next, the fourth rank tensor is considered, building off the approach developed above. First, the rank 4 subspace will be examined, and terms analogous to those derived for the second and third rank tensors will be examined. The first invariant is readily defined as the norm of the rank 4 spherical tensor defined in eq 25 below.

$$\begin{aligned} N[4,4]_0 &= \frac{1}{3} \{(\tilde{v}_4^0)^2 + (\tilde{v}_4^1)^2 + (\tilde{v}_4^2)^2 + (\tilde{v}_4^3)^2 + (\tilde{v}_4^4)^2\} \\ &= \frac{1}{3} \{(\mu_4^0)^2 + (\mu_4^2)^2 + (\mu_4^3)^2 + (\mu_4^4)^2\} \end{aligned} \quad (39)$$

This is the sum of the magnitudes of all of the $l=4$ distortions shown in Figure 1. The expansions of the rank 2 contractions are then explored, similar to the third order terms above. The first of these is the norm of the rank 2 contraction. When evaluated in the random orientation, this yields a complication expression that depends on all nine variables (See Supplemental Material S.4). However, when rotated to the *HS* configuration, the dependence on the rotation angles simplifies somewhat to a dependence on just $\bar{\omega}_2$ and $\bar{\omega}_2 - 3\bar{\omega}_3$ as shown below.

$$\begin{aligned} &N[N[4,4]_2, N[4,4]_2]_0 \\ &= \frac{1}{13860} \{ \sqrt{5}(400(\mu_4^0)^4 + 64(\mu_4^2)^4 + 14(\mu_4^2)^2 \{(\mu_4^3)^2 - 8(\mu_4^4)^2\}) \\ &+ 49\{(\mu_4^3)^4 + 32(\mu_4^3)^2(\mu_4^4)^2 + 16(\mu_4^4)^4\} + 40(\mu_4^0)^2 \{62(\mu_4^2)^2 - 7(\mu_4^3)^2 - 28(\mu_4^4)^2\} \\ &+ 120\sqrt{7}\mu_4^2\mu_4^4 (12\mu_4^0\mu_4^2 \cos(4\bar{\omega}_2) + 7\sqrt{5}(\mu_4^3)^2 \cos(2\{\bar{\omega}_2 - 3\bar{\omega}_3\})) \} \\ &= F \left[\begin{array}{c} (\mu_4^0)^4, (\mu_4^2)^4, (\mu_4^3)^4, (\mu_4^4)^4, \\ (\mu_4^0)^2(\mu_4^2)^2, -(\mu_4^0)^2(\mu_4^3)^2, -(\mu_4^0)^2(\mu_4^4)^2, (\mu_4^2)^2(\mu_4^3)^2, -(\mu_4^2)^2(\mu_4^4)^2, (\mu_4^3)^2(\mu_4^4)^2 \\ \mu_4^0(\mu_4^2)^2\mu_4^4 \cos(4\bar{\omega}_2), \mu_4^2(\mu_4^3)^2\mu_4^4 \cos(2\{\bar{\omega}_2 - 3\bar{\omega}_3\}) \end{array} \right] \end{aligned} \quad (40)$$

Additionally, we reduce that expression to a simpler functional form where we only list the polynomial forms (and their sign dependence where appropriate). Here, this makes it obvious that all terms are quartic polynomials, and that not all possible terms are present. This is an important aspect for recognizing the completeness of the invariants. The skewness of the rank 2 contraction is also then calculated similar to the skewness of the rank 2 contraction of the third order tensor above. The result in the *HS* configuration is somewhat more complicated than the term above, and it is given in the supplemental

material S.5. The functional form is given below where this is now a sixth order polynomial, and again it is seen that not all possible terms are present.

$$\begin{aligned}
& N[N[N[4,4]_2, N[4,4]_2]_2, N[4,4]_2]_0 \\
= F & \left[\begin{array}{l}
(\mu_4^0)^6, (\mu_4^2)^6, -(\mu_4^3)^6, -(\mu_4^4)^6, -(\mu_4^0)^4(\mu_4^2)^2, -(\mu_4^0)^4(\mu_4^3)^2, -(\mu_4^0)^4(\mu_4^4)^2, \\
-(\mu_4^0)^2(\mu_4^2)^4, (\mu_4^0)^2(\mu_4^3)^4, (\mu_4^2)^4(\mu_4^3)^2, -(\mu_4^2)^4(\mu_4^4)^2, -(\mu_4^3)^4(\mu_4^2)^2, \\
-(\mu_4^3)^4(\mu_4^4)^2, (\mu_4^2)^2(\mu_4^4)^4, -(\mu_4^3)^2(\mu_4^4)^4, (\mu_4^0)^2(\mu_4^2)^2(\mu_4^3)^2, (\mu_4^0)^2(\mu_4^2)^2(\mu_4^4)^2, \\
(\mu_4^0)^2(\mu_4^3)^2(\mu_4^4)^2, -(\mu_4^2)^2(\mu_4^3)^2(\mu_4^4)^2, \\
[-(\mu_4^0)^2, -(\mu_4^2)^2, -(\mu_4^3)^2, (\mu_4^4)^2](\mu_4^0)(\mu_4^2)^2(\mu_4^4)\text{Cos}[4\bar{\omega}_2], \\
[(\mu_4^0)^2, -(\mu_4^2)^2, -(\mu_4^3)^2, -(\mu_4^4)^2](\mu_4^2)(\mu_4^3)^2(\mu_4^4)\text{Cos}[2\{\bar{\omega}_2 - 3\bar{\omega}_3\}], \\
-(\mu_4^0)(\mu_4^2)^3(\mu_4^3)^2\text{Cos}[6\{\bar{\omega}_2 - 3\bar{\omega}_3\}], -(\mu_4^0)(\mu_4^2)(\mu_4^3)^2(\mu_4^4)^2\text{Cos}[2\{\bar{\omega}_2 + 3\bar{\omega}_3\}]
\end{array} \right] \quad (41)
\end{aligned}$$

These terms are normalized to their invariant forms as has previously been done for the lower order forms.

$$P4I0(a) = \frac{(N[4,4]_0)^{1/2}}{P0I0(a)} \quad (42)$$

$$P4I1(a) = \frac{(N[N[4,4]_2, N[4,4]_2]_0)^{1/2}}{(N[4,4]_0)^{1/2} * P0I0(a)} \quad (43)$$

$$P4I2(a) = \frac{N[N[N[4,4]_2, N[4,4]_2]_2, N[4,4]_2]_0}{N[N[4,4]_2, N[4,4]_2]_0 * (N[4,4]_0)^{1/2} * P0I0(a)} \quad (44)$$

The units here are now $(r/\sigma)^4$ with equal weighting factors occurring in both the numerator and denominator. Similar to before, the $P4I0$ metric captures the net deformation away from spherical symmetry in any of the fourth order deformations. The characteristics of the $P4I1$ and $P4I2$ metrics are illustrated in Figure 6.

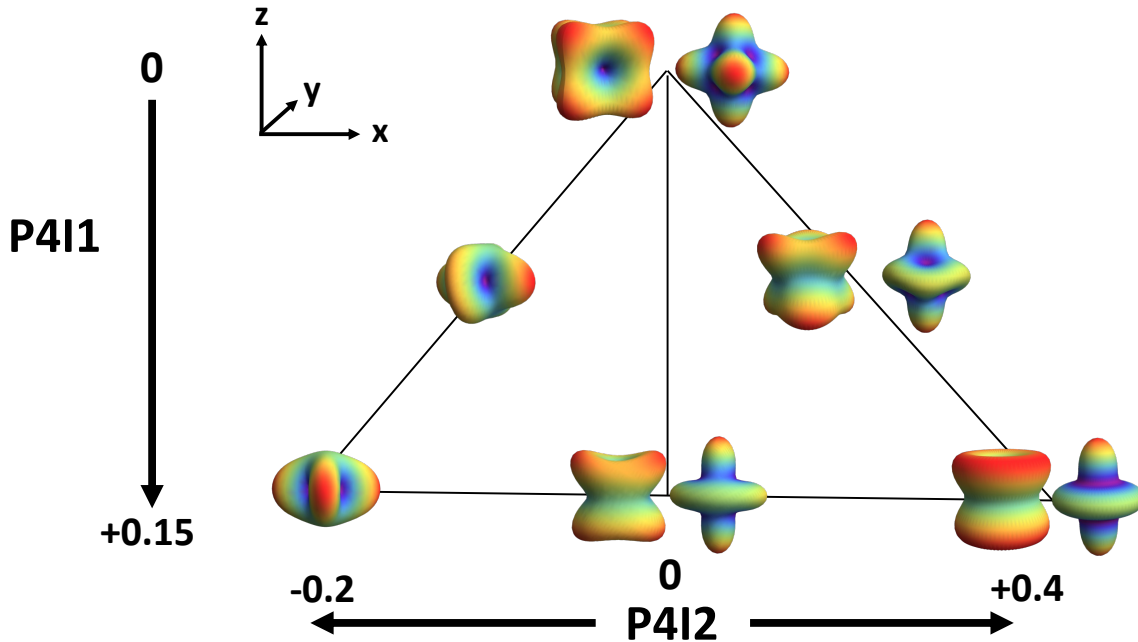


Figure 6. Illustration of the fourth order Strain Functional Descriptors $P4I1$ and $P4I2$. The $P4I1$ quantity measures the net amount of distortion away from the ideal octahedral geometry of O_h symmetry shown at the top. Here, this can be either a body-centered cubic structure on the left, or the simple cubic structure on the right. The $P4I2$ quantity measures one of the skewness characteristics of the fourth order distortions. A negative value corresponds to a flattening distortion of the octahedron along one of its C_4 axes to generate the $D_{4h} \tilde{v}_4^{\pm 4}$ structure. A positive value corresponds a smoothing rotation about one of the C_4 axes to generate the bell-shaped $D_{\infty h} \tilde{v}_4^0$. These figures are drawn in the HS frame, with that axis frame shown in the upper left. For the $P4I2$ deformation, the $D_{\infty h}$ and C_4 rotation axes coincide with the internal z axis and the xy plane is defined by the fourfold outward extensions of the D_{4h} structure. Note the similarity to the $P2I1$ metric in Figure 2 and the $P3I1$ and $P3I2$ metrics in Figure 3. The magnitudes of the $P4I1$ and $P4I2$ terms will be constrained by the value of the $P4I0$ term.

Figure 6 shows the nature of the $P4I1$ and $P4I2$ invariants. We first note that the magnitudes of these two terms are constrained by the value of the $P4I0$. They have finite ranges limited by that, which has a value of ~ 0.4 for the illustrative figures shown. The $P4I1$ invariant has the notable characteristic that its value is zero for a pure octahedral distortion, and its value becomes increasingly positive as the geometry is distorted away from octahedral, O_h . We particularly note that the octahedron is the highest symmetry object (i.e., the most ideal shape) that can be realized for fourth order distortions. Within this framework, there are two particular O_h variants that cannot yet be distinguished. These are the body-centered cubic (*bcc*) structure shown to the left side, and the simple cubic (*sc*) structure shown to the right side. Another invariant, to be defined below, is required to distinguish between those structures.

The $P4I2$ invariant is the primary skewness metric for the $P4II$ distortion which characterizes the nature of the non-octahedral distortion. In the positive extreme, the structure becomes the axially symmetric $D_{\infty h} \tilde{v}_4^0$ structure, while in the negative extreme the structure becomes the flatter $D_{4h} \tilde{v}_4^{\pm 4}$ structure. For a value of $P4I2 = 0$, the structures have a lower symmetry of D_{2h} or C_{2h} . In the Figure, the shapes were drawn in the HS configuration. This emphasizes that the $D_{\infty h}$ axis of the \tilde{v}_4^0 structure and C_4 axis of the $D_{4h} \tilde{v}_4^{\pm 4}$ structure coincide with the internal z axis of the HS structure. Further, the four-fold lobes of the $D_{4h} \tilde{v}_4^{\pm 4}$ structure define the xy plane, with one lobe aligned with the x axis. This behavior is very similar to the $P2II$ metric shown in Figure 2, which also derives from a rank 2 skewness metric. For a positive value of $P4I2$, the two variant structures of octahedral geometry persist and are shown. For a negative value of $P4I2$, these structural differences diminish and correspond more to a rotation angle difference.

Similar to what was observed for the moments of the third rank tensor (see eqs 31), it is not difficult to show that the $N[N[4,4]_x, N[4,4]_x]_0$ moments for $x = 4, 6, 8$ can be simply related back the moment for $x = 2$ and $N[4,4]_0$ (Supplemental Material S.6-8). Consequently, they contain no additional information. Additionally, the terms with $x = odd$ are all zero by symmetry. Similar to the third rank tensor, the skewness of the rank 4 contraction is then constructed and the signs of the various terms are given below, with the full expression given in the supplemental material (S.9).

$$N[N[N[4,4]_4, N[4,4]_4]_4, N[4,4]_4]_0 = F \begin{bmatrix} (\mu_4^0)^6, -(\mu_4^2)^6, -(\mu_4^3)^6, (\mu_4^4)^6, -(\mu_4^0)^4(\mu_4^2)^2, -(\mu_4^0)^4(\mu_4^3)^2, (\mu_4^0)^4(\mu_4^4)^2, \\ (\mu_4^0)^2(\mu_4^2)^4, -(\mu_4^2)^4(\mu_4^3)^2, (\mu_4^2)^4(\mu_4^4)^2, (\mu_4^0)^2(\mu_4^3)^4, -(\mu_4^2)^2(\mu_4^3)^4, -(\mu_4^3)^4(\mu_4^4)^2, \\ (\mu_4^0)^2(\mu_4^4)^4, -(\mu_4^2)^2(\mu_4^4)^4, (\mu_4^3)^2(\mu_4^4)^4, (\mu_4^0)^2(\mu_4^2)^2(\mu_4^3)^2, -(\mu_4^0)^2(\mu_4^2)^2(\mu_4^4)^2, \\ -(\mu_4^0)^2(\mu_4^3)^2(\mu_4^4)^2, -(\mu_4^2)^2(\mu_4^3)^2(\mu_4^4)^2, \\ [(\mu_4^0)^2, -(\mu_4^2)^2, -(\mu_4^3)^2, (\mu_4^4)^2](\mu_4^0)(\mu_4^2)^2(\mu_4^4)\text{Cos}[4\bar{\omega}_2], (\mu_4^2)^4(\mu_4^4)^2\text{Cos}[8\bar{\omega}_2] \\ [-(\mu_4^0)^2, (\mu_4^2)^2, (\mu_4^3)^2, (\mu_4^4)^2](\mu_4^2)(\mu_4^3)^2(\mu_4^4)\text{Cos}[2\{\bar{\omega}_2 - 3\bar{\omega}_3\}], \\ (\mu_4^0)(\mu_4^2)^3(\mu_4^3)^2\text{Cos}[6\{\bar{\omega}_2 - \bar{\omega}_3\}], (\mu_4^0)(\mu_4^2)(\mu_4^3)^2(\mu_4^4)^2\text{Cos}[2\{\bar{\omega}_2 + 3\bar{\omega}_3\}] \end{bmatrix} \quad (45)$$

This expression contains many terms in common with the rank 2 skewness term given in eq 41 where they are both sixth order polynomial forms. However, there are differences in the signs of some terms as well some terms that are absent in one or the other. This demonstrates that they capture different attributes. For example, the first four terms (which would describe the shape when there is distortion in only one of the fundamental modes) have different sign patterns: both terms would be positive if a μ_4^0 distortion is present and would be negative if a μ_4^3 distortion is present. However, the two terms would have opposite signs is only a μ_4^2 or a μ_4^4 distortion is present. Also of particular note is the last term in the fifth line: $(\mu_4^2)^4(\mu_4^4)^2\text{Cos}[8\bar{\omega}_2]$. This term will be non-zero only when contributions from both μ_4^2 and μ_4^4 are present. And if only those two terms are non-zero, then almost all of the other terms will be zero; only $-(\mu_4^2)^6$, $(\mu_4^2)^4(\mu_4^4)^2$ and $-(\mu_4^2)^2(\mu_4^4)^4$ would survive. Consequently, the $P4I3$ term should have a strong dependence on $\bar{\omega}_2$, the rotation angle of the μ_4^2 contribution relative to μ_4^4 contribution. These characteristics identify this term as the next invariant of the fourth order expansion, which is given in eq

46. It is normalized similarly to the analogous term in eq 36, measuring the skewness of the rank 4 contraction.

$$P4I3(a) = \frac{N[N[N[4,4]_4, N[4,4]_4]_4, N[4,4]_4]_0}{N[N[4,4]_4, N[4,4]_4]_0 * (N[4,4]_0)^{1/2} * P0I0(a)} \quad (46)$$

The characteristic behavior of this metric is illustrated in Figure 7, where it is plotted versus the $P4II$ metric. The base function of $P4I3$, the numerator in eq 46, is rigorously the skewness metric of the function $N[N[4,4]_4, N[4,4]_4]_0$. That is a complementary function of $N[N[4,4]_2, N[4,4]_2]_0$, which is the base function of $P4II$. Consequently, $P4I3$ spans a range of values and structures for $P4II \approx 0$, but limits to a narrow range as $P4II$ increases in value (limited by the value of $P4I0$). The defining characteristic of the O_h structures in the upper left, with an extreme positive value of $P4I3$, is that they have 3 perpendicular and equivalent C_4 axes, which then generate 6 equivalent C_2 axes and 3 equivalent and perpendicular C_3 axes. The defining characteristic of the high symmetry structures in the lower left is that they have *no* C_4 axes. The $D_{3d} \tilde{\nu}_4^3$ structure has one C_3 axis with 3 coplanar C_2 axes that are perpendicular to the C_3 direction, and the $D_{2h} \tilde{\nu}_4^2$ structure has 3 perpendicular but inequivalent C_2 axes. Both structures can be viewed as an overall trigonal distortion of the octahedral geometry. As the value of $P4II$ increases from its minimal value, the structures with a positive value of $P4I3$ degrade into D_{4h} structures only one C_4 axis, but with 4 C_2 axes and *no* C_3 axes. In contrast, the structures with a negative value of $P4I3$ maintain the lower symmetry D_{3d} structure with one C_3 axis, 3 C_2 axes and *no* C_4 axes. Along the midline of $P4I3 = 0$, the structures have only C_{2h} symmetry (a C_2 axis with a perpendicular reflection plane), with no obvious preference for higher C_4 or C_3 symmetry. Those tendencies develop for further distortions where positive or negative values of $P4I3$ develop, respectively.

The effect of the rotation angle $\bar{\omega}_2$ is illustrated by the structures contained in the yellow box in the middle of Figure 7. These structures are all a combination of $(2/3) \mu_4^2$ distortion and $(1/3) \mu_4^4$ distortion, with the only difference being the rotation angle between those two factors. If that phase angle is 0 , the nearly *bcc* D_{4h} structure results (upper right), and if the phase angle is $\pi/4$, the nearly *sc* D_{4h} structure results (upper left). If the phase angle is $\pi/8$, the nearly trigonal D_{2h} structure at the bottom results. For a phase angle of $\pi/16$ or $3\pi/16$, then the C_{2h} structures in the middle result. This further illustrates the points made above.

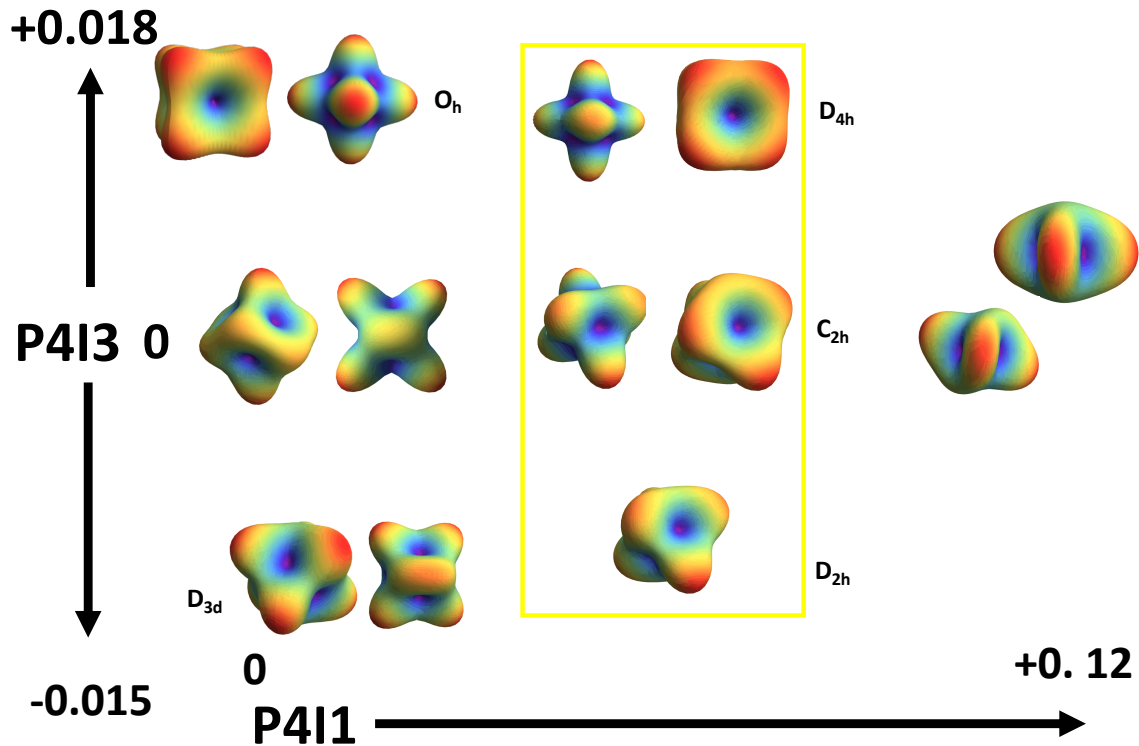


Figure 7. Illustration of the sixth order Strain Functional Descriptor $P4I3$. Similar to $P4I2$, this is a skewness metric related the base $P4I1$ quantity, though it is more directly related to a complement of that quantity. For a large value of $P4I1$, the range of $P4I3$ becomes quite narrow and the limiting structure is a distorted version of the $D_{4h} \tilde{v}_4^4$ structure (at right). The maximum range for $P4I3$ occurs when the $P4I1$ is ~ 0 . There, a positive value limits to the two possible octahedral structures (bcc and sc) in the upper left. Increasing the value of $P4I1$ while maintaining a positive value of $P4I3$ maintains the C_4 axis symmetry, and a primarily D_{4h} symmetry structure, while degrading the other octahedral symmetries. A negative value of $P4I3$, corresponds to two possible high symmetry distortions of the octahedron, the trigonally distorted $D_{3d} \tilde{v}_4^3$ and the orthorhombically distorted $D_{2h} \tilde{v}_4^2$ structures shown in the lower left. A range of structures with $P4I3 = 0$ and increasing values of $P4I1$ is shown along the center line. These structures have only C_{2h} symmetry, and their similarity to an octahedral structure is seen to diminish in progressing to the right. The structures contained in the yellow box are combinations of \tilde{v}_4^2 and \tilde{v}_4^4 distortions with different phase angles.

As with the third order expansions, it becomes apparent that the other skewness metrics $N[N[N[4,4]_x, N[4,4]_x]_x, N[4,4]_0]$ with $x = 6$ and 8 can be simply related back the lower order moments. So mixed order expansions and expansions with an odd number of terms were then explored. A fivefold contraction of rank 2 contractions had a quite interesting form given in eq 47 below. (This form is equivalent to the mixed fivefold contraction of rank 2 and rank 4 contractions as shown.) One aspect is that the first collection of terms is multiplied by μ_4^0 such that it will only be non-zero if $\mu_4^0 \neq 0$, and that the sign of that term

will be reflected by the sign of μ_4^0 . This is distinct from all of the previous terms discussed so far. The second aspect is the form of the last two terms in the final line. The last term in particular will be non-zero only if both the μ_4^2 and the μ_4^3 distortions are non-zero. Further if only those two factors are non-zero, then only that term will be non-zero and its sign will be determined by the phase angle difference $\bar{\omega}_2 - \bar{\omega}_3$.

$$N[N[N[4,4]_2, 4]_2, N[4,4]_2]_0 = N[N[N[4,4]_2, N[4,4]_2]_4, 4]_0 =$$

$$F \left[\mu_4^0 \begin{bmatrix} (\mu_4^0)^4, -(\mu_4^2)^4, -(\mu_4^2)^2(\mu_4^3)^2, (\mu_4^2)^2(\mu_4^4)^2, (\mu_4^3)^4, -(\mu_4^3)^2(\mu_4^4)^2, (\mu_4^4)^4 \\ -(\mu_4^0)^2(\mu_4^2)^4, -(\mu_4^0)^2(\mu_4^3)^2, -(\mu_4^0)^2(\mu_4^4)^4 \\ [(\mu_4^2)^2\mu_4^4((\mu_4^0)^2, -(\mu_4^2)^2, (\mu_4^3)^2, (\mu_4^4)^2)\text{Cos}[4\bar{\omega}_2], \\ -\mu_4^0\mu_4^2(\mu_4^3)^2\mu_4^4\text{Cos}[2(\bar{\omega}_2 - 3\bar{\omega}_3)], (\mu_4^2)^3(\mu_4^3)^2\text{Cos}[6(\bar{\omega}_2 - \bar{\omega}_3)] \end{bmatrix} \right] \quad (47)$$

These unique characteristics identify this term as a non-redundant invariant. Since the numerator is formed by a series of rank 2 contractions, it is scaled by the norm of the rank 2 contraction raised to the 3/2 power, as well as the overall norm of the rank 4 term and the sum of the weighting terms. The resulting *P4I4* invariant is defined in eq 48.

$$P4I4(a) = \frac{N[N[N[4,4]_2, 4]_2, N[4,4]_2]_0}{(N[N[4,4]_2, N[4,4]_2]_0)^{3/2} * (N[4,4]_0)^{1/2} * P0I0(a)} \quad (48)$$

The significance of this term is illustrated in Figure 8, where the deformations in the *P4I4* term are plotted vs the *P4I1* term. For the extreme values of *P4I1*, the structures limit to values of *P4I4* = 0. These are the equivalent *sc* and *bcc* O_h structures for *P4I1* = 0 at the left, and the D_{4h} \tilde{v}_4^4 structure at the right. For intermediate values of *P4I1* however is where the significance of the *P4I4* becomes apparent. As suggested above, the maximum range of *P4I4* occurs when only the \tilde{v}_4^0 deformation is present. It is positive for when \tilde{v}_4^0 is positive (density present along the z axis and cylindrically distributed in the xy plane), and negative for a negative value of \tilde{v}_4^0 (density cylindrically distributed intermediate between the z axis and the xy plane).

The effect of the $\bar{\omega}_2 - \bar{\omega}_3$ phase angle is illustrated by the structures highlighted in the yellow box. These structures are all a combination of $\sim(1/2) \mu_4^2$ distortion and $\sim(1/2) \mu_4^3$ distortion, with the only difference being the rotation angle between those two factors. If that phase angle is 0, the nearly D_{3d} distortion of the *sc* structure results (upper inset, C_{2h} actual symmetry). Here the alternate four in-plane apices of the *sc* structure distort above and below the plane and lose their radial distinction, as they trend towards the $+\tilde{v}_4^0$ structure. If the phase angle is $\pi/6$, the nearly D_{3d} distortion of the *bcc* structure results (lower inset, C_{2h} actual symmetry). Here, two pairs of diagonally opposite neighbors are coalescing into single nodes and losing their overall radial distinction, as they trend towards the $-\tilde{v}_4^0$ structure. If the phase angle is $\pi/12$ or $\pi/4$, the low symmetry C_{2h} structure in the middle results, where there are three distinct pairs of vertices apparent. Along the midline of *P4I4* = 0 in general are similar low symmetry structures, though these do limit into high symmetry structures for the extreme values of *P4I1* as noted above.

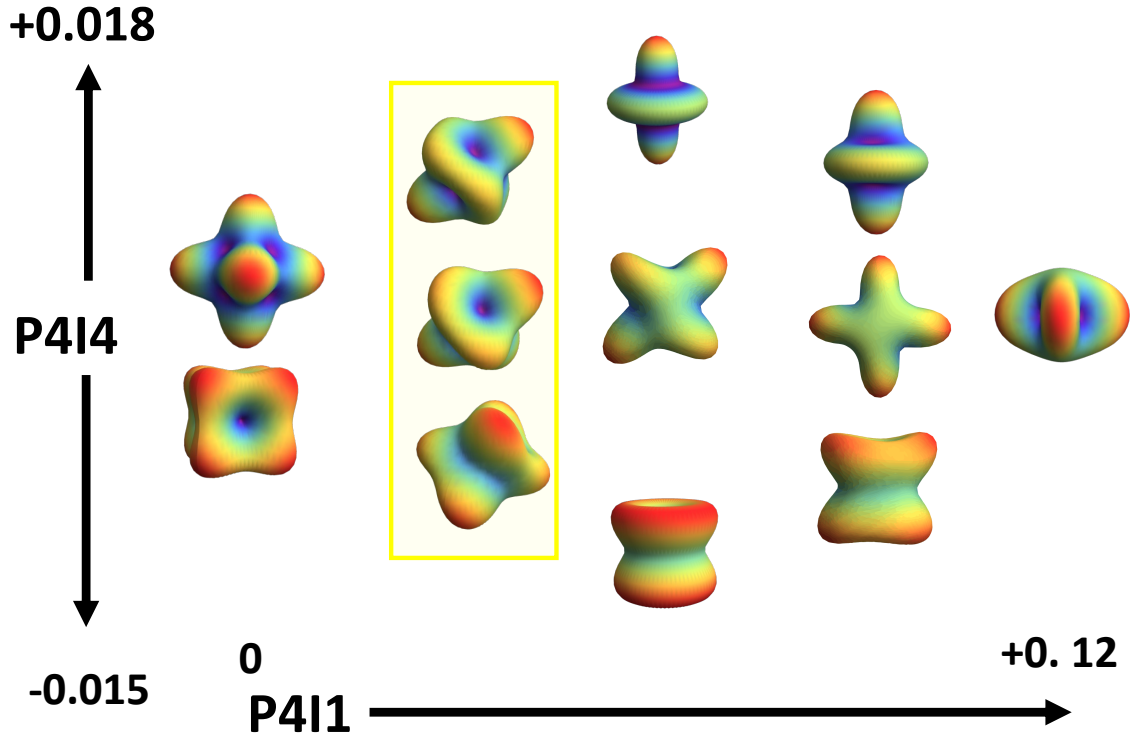


Figure 8. Illustration of the fifth order Strain Functional Descriptor $P4I4$. This element has rather distinct behavior plotted vs the $P4I1$ metric. For a large value of $P4I1$, the range of $P4I4$ becomes quite narrow and the limiting structure is the $D_{4h} \tilde{v}_4^4$ structure (at right). For the minimum value of $P4I1 = 0$, the range of structures also becomes quite narrow and limits to the two possible octahedral structures (bcc and sc). For an intermediate value of $P4I1$ is where $P4I4$ has its maximum range. The maximum positive value of $P4I4$ corresponds to a positive \tilde{v}_4^0 distortion, while the maximum negative value corresponds to a negative \tilde{v}_4^0 distortion. The structures contained in the yellow box are combinations of \tilde{v}_4^2 and \tilde{v}_4^3 distortions with different phase angles (see text). A range of structures with $P4I4 = 0$ and increasing values of $P4I1$ is shown along the center line. These structures have only C_{2h} symmetry, but limit to high symmetry structures for the extreme values of $P4I1$.

A sevenfold contraction of rank 4 contractions generates another invariant with distinct characteristic, where the functional form is given in eq 49. The unique term with respect to the other invariants is the final term in that expression which only depends on $\bar{\omega}_3$ itself rather than its value with respect to $\bar{\omega}_2$. It will be non-zero only when μ_4^3 and μ_4^4 are non-zero, and the magnitude and sign depends on $\bar{\omega}_3$, the phase angle between those two terms.

$$N[N[N[4,4]_4, 4]_4, N[[4,4]_4, [4,4]_4]_4]_0 = \quad (49)$$

$$F \left[\begin{array}{l} (\mu_4^0)^7, -(\mu_4^0)^5(\mu_4^2)^2, (\mu_4^0)^3(\mu_4^2)^4, -(\mu_4^0)(\mu_4^2)^6, (\mu_4^0)^5(\mu_4^3)^2, -(\mu_4^0)^3(\mu_4^3)^4, -(\mu_4^0)(\mu_4^3)^6, \\ -(\mu_4^0)^3(\mu_4^2)^2(\mu_4^3)^2, -(\mu_4^0)(\mu_4^2)^4(\mu_4^3)^2, -(\mu_4^0)(\mu_4^2)^2(\mu_4^4)^4, (\mu_4^0)^5(\mu_4^4)^2, (\mu_4^0)(\mu_4^4)^6, \\ -(\mu_4^0)^3(\mu_4^2)^2(\mu_4^4)^2, -(\mu_4^0)(\mu_4^2)^4(\mu_4^4)^2, -(\mu_4^0)^3(\mu_4^3)^2(\mu_4^4)^2, -(\mu_4^0)(\mu_4^2)^2(\mu_4^3)^2(\mu_4^4)^2, \\ (\mu_4^0)(\mu_4^3)^4(\mu_4^4)^2, (\mu_4^0)^3(\mu_4^4)^4, (\mu_4^0)(\mu_4^2)^2(\mu_4^4)^4, (\mu_4^0)(\mu_4^3)^2(\mu_4^4)^4, \\ (\mu_4^0)^4, (\mu_4^2)^4, (\mu_4^3)^4, (\mu_4^4)^4, \\ [(\mu_4^0)^2\{(\mu_4^2)^2, (\mu_4^3)^2, (\mu_4^4)^2\}, (\mu_4^2)^2\{(\mu_4^3)^2, (\mu_4^4)^2\}, (\mu_4^3)^2(\mu_4^4)^2] (\mu_4^2)^2(\mu_4^4)\text{Cos}[4\bar{\omega}_2], \\ [-(\mu_4^0)^2, (\mu_4^2)^2, (\mu_4^3)^2, -(\mu_4^4)^2](\mu_4^0)(\mu_4^2)(\mu_4^3)^2(\mu_4^4)\text{Cos}[2\{\bar{\omega}_2 - 3\bar{\omega}_3\}], \\ [-(\mu_4^0)^2, (\mu_4^2)^2, (\mu_4^3)^2, -(\mu_4^4)^2](\mu_4^2)^3(\mu_4^3)^2\text{Cos}[6\{\bar{\omega}_2 - \bar{\omega}_3\}], \\ [-(\mu_4^0)^2, -(\mu_4^2)^2, -(\mu_4^3)^2, (\mu_4^4)^2](\mu_4^2)(\mu_4^3)^2(\mu_4^4)^2\text{Cos}[2\{\bar{\omega}_2 + 3\bar{\omega}_3\}], \\ (\mu_4^0)(\mu_4^2)^4(\mu_4^4)^2\text{Cos}[8\bar{\omega}_2], -(\mu_4^3)^4(\mu_4^4)^3\text{Cos}[12\bar{\omega}_3], \end{array} \right]$$

This distinct characteristic identifies this term as the final non-redundant invariant for this subspace. Since the numerator is formed by a series of rank 4 contractions, it is scaled by the norm of the rank 4 contraction, as well as the overall norm of the rank 4 term and the sum of the weighting terms. The resulting *P4I5* invariant is defined in eq 50.

$$P4I5(a) = \frac{N[N[N[4,4]_4,4]_4, N[N[4,4]_4, N[4,4]_4]_4]_0}{N[N[4,4]_4, N[4,4]_4]_0 * N[4,4]_0 * P0I0(a)} \quad (50)$$

The significance of this term is illustrated in Figure 9, where the deformations in the *P4I5* term are plotted vs the *P4I1* term. For the extreme value of *P4I1* = 0, the *sc* and *bcc* O_h structures are finally resolved. For larger values of *P4I1*, this term demonstrates somewhat similar behavior to *P4I4*: the $\pm\tilde{\nu}_4^0$ structures are distinguished and they asymptote to the D_{4h} $\tilde{\nu}_4^4$ structure at the right. However, there are subtle differences arising from the presence of the $\bar{\omega}_3$ phase angle which is illustrated by the structures highlighted in the yellow box. These structures are all a combination of $\sim(1/2)\mu_4^3$ distortion and $\sim(1/2)\mu_4^4$ distortion, with the only difference being the rotation angle between those two factors. If that phase angle is 0, the structure shows a distortion towards the *sc* structure, with lobes appearing asymmetrically on the top and bottom of the D_{4h} $\tilde{\nu}_4^4$ structure. This is shown as the upper highlighted structure which has C_{2h} symmetry (the reflection plane is rotated $\pi/4$ about the vertical axis with respect to the plane of the page). If the phase angle is $\pi/12$, the structure shows a distortion towards the *bcc* structure, with all of the four lobes of the D_{4h} $\tilde{\nu}_4^4$ structure starting to split asymmetrically. This is shown as the lower highlighted structure which also has C_{2h} symmetry (the reflection plane is rotated $\pi/2$ about the vertical axis with respect to the plane of the page). If the phase angle is $\pi/24$, the low symmetry C_i structure in the middle results, where the lobe projecting out of the paper plane does *not* have C_2 symmetry. Along the midline of *P4I5* = 0 in general are similar low symmetry C_i structures.

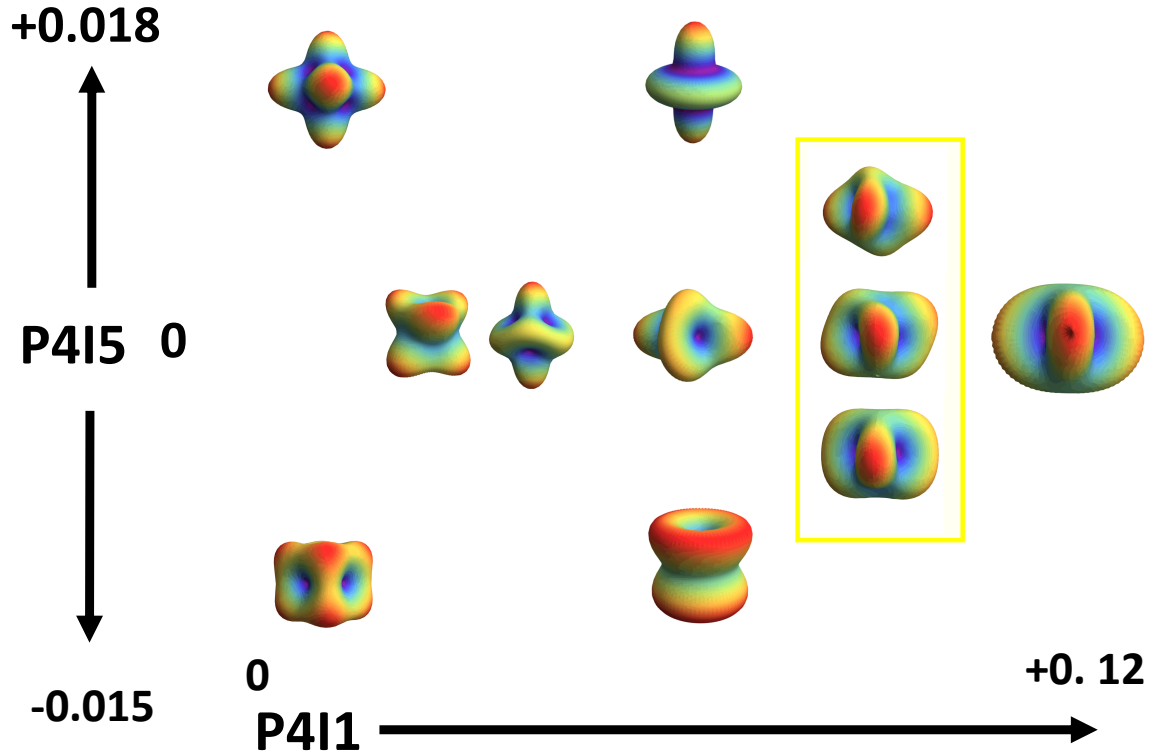


Figure 9. Illustration of the seventh order Strain Functional Descriptor $P4I5$. Again plotted vs. the $P4I1$ metric, this element has the distinct characteristic of distinguishing the two O_h structures at $P4I1 = 0$: the simple cubic (sc) in the upper left and the bcc structure in the lower left. This also distinguishes the positive and negative \tilde{v}_4^0 distortions for intermediate values of $P4I1$, similar to $P4I4$. The structures contained in the yellow box are combinations of \tilde{v}_4^3 and \tilde{v}_4^4 distortions with different phase angles (see text). This is another unique attribute of this descriptor. A range of structures with $P4I5 = 0$ and increasing values of $P4I1$ is shown along the center line. These structures generally have only C_i symmetry.

The 2nd order and 0th order subspaces are then readily define by analogy to the rank 2 subspace (eqs 21-23) and the scaled invariants are given below. For $P4I8$, this term is spherically symmetric (no angular dependence), but it nominally has two radial nodes to make it orthogonal to $P2I2$ and $P0I0$. Hence its more complicated structure.

$$P4I6(a) = \frac{\sqrt{N[2(4),2(4)]_0}}{P0I0(a)} \quad (51)$$

$$P4I7(a) = -\frac{N[N[2(4),2(4)]_2,2(4)]_0}{N[2(4),2(4)]_0 * P0I0(a)} \quad (52)$$

$$P4I8(a) = \frac{v_{0(4)}^0}{P0I0(a)} - \sqrt{5} \left(P2I2(a) + \sqrt{\frac{3}{2}} \right) + \sqrt{\frac{15}{8}} \quad (53)$$

Orientation functions. There are several options available for defining the orientation functions which can depend upon the particular application and the information desired. At least one of the ranks must be defined with respect to the external axis frame. The remaining ranks can then either be defined with respect to that chosen rank (defining a completely internally defined structure) or with respect the external axis frame. For the current application of characterizing MD simulations of metals, we will choose the latter. As discussed further below, the rank 4 tensors tend to carry information about the orientation of the local crystal domain. The lower rank tensors tend to carry information about the deformation of that crystal (shear strains, strain gradients) which tend to be predominantly oriented by an externally applied strain. For the subspaces within each rank, we choose to define their orientation with respect to the highest order subspace. This is because the deformations within those subspaces are likely interrelated.

We will start with the latter. As pointed out in the discussions above, the rank 2 contractions of any of the rank n tensors identify the internal xyz axes of that rank defining the HS coordinate frame. There are then three degrees of freedom (rotations) that define the relative orientations between any of these axis frames. These can be found from the 2 and 3-way rank 2 contractions of those tensors. This is illustrated in Appendix A where it is shown how to extract the Euler angles that define the orientation of a rank 2 ST with respect to an arbitrary coordinate frame. As discussed there, the selection of an absolute direction orientation is has subjective aspects to it. However, the invariants which define the relative orientations provide fixed values. For the rank 4 space, we define these invariants as follows:

$$P4I9(a) = N[N[4,4]_2, 2(4)]_0 \frac{(N[4,4]_0 * N[2(4), 2(4)]_0)^{1/4}}{(N[N[4,4]_2, N[4,4]_2]_0 * N[2(4), 2(4)]_0)^{1/2} * P0I0(a)} \quad (54)$$

$$P4I10(a) = N[N[N[4,4]_2, 2(4)]_2, N[4,4]_2] \frac{(N[4,4]_0 * N[2(4), 2(4)]_0)^{1/4}}{N[N[4,4]_2, N[4,4]_2]_0 * (N[2(4), 2(4)]_0)^{1/2} * P0I0(a)} \quad (55)$$

$$P4I11(a) = N[N[N[4,4]_2, 2(4)]_2, 2(4)] \frac{(N[4,4]_0 * N[2(4), 2(4)]_0)^{1/4}}{(N[N[4,4]_2, N[4,4]_2]_0)^{1/2} * N[2(4), 2(4)]_0 * P0I0(a)} \quad (56)$$

These terms are written in a way that emphasizes the three possible rank 2 contractions of two rank 2 ST multiplied by normalization factors. The denominators of the latter are all distinct and scale the contractions by the magnitudes of the component tensors. Multiplied by the leading contractions, this would constrain those products to have values in the range of $[-1, 1]$ and could be defined as an inverse cos function of an angle between the component tensors. The numerator of the normalization factors are the same and are the geometric mean of the magnitudes of main rank 4 ST and the rank 2 subspace of that. This gives all three invariants effective units of $(r/\sigma)^4$, balancing their magnitudes with the other P4 invariants.

Similar functions can be defined for the rank 3 space. A distinction here is that the rank 1 subspace is only defined by the direction of a line, so only two angles (and invariants) are required to define its orientation with respect to the rank 3 ST. Those invariants are defined

below, where eqs 57 and 58 are analogous to eqs 54 and 55. The analog to eq 56 does not contain any additional information.

$$P3I5(a) = N[N[3,3]_2, N[1(3), 1(3)]_2]_0$$

$$* \frac{(N[3,3]_0 * N[1(3), 1(3)]_0)^{1/4}}{(N[N[3,3]_2, N[3,3]_2]_0 * N[N[1(3), 1(3)]_2, N[1(3), 1(3)]_2]_0)^{1/2} * P0I0(a)} \quad (57)$$

$$P3I6(a) = N[N[N[3,3]_2, N[1(3), 1(3)]_2]_2, N[3,3]_2]$$

$$* \frac{(N[3,3]_0 * N[1(3), 1(3)]_0)^{1/4}}{N[N[3,3]_2, N[3,3]_2]_0 * (N[N[1(3), 1(3)]_2, N[1(3), 1(3)]_2]_0)^{1/2} * P0I0(a)} \quad (58)$$

Finally, we consider the orientation of the main ST themselves. One obvious choice would be to simply use the orientation framework that defines the HS orientation. While this would be useful for some applications, it is not very useful for the current application of MD simulations for metals. Considering *bcc* and *fcc* metals in particular, the *x*, *y* and *z* axes can be readily interchanged for the ideal structure and they cannot be distinguished. Given some low level of thermal fluctuations, there will be distortions away from that ideal structure, often dominated by an orthorhombic distortion. The C_4 axis of that structure will be defined as the *Z* axis for the HS structure. Given that the initial structure was aligned with the external *xyz* frame, one tends to observe structures that are randomly aligned with one of the *x*, *y* or *z* axes and these will fluctuate with time. For somewhat higher temperatures, one would also observe trigonal distortions that would align the *Z* axis with the 111 crystallographic direction. For higher temperatures, though still below melting, all sense of directionality will be lost because of the large of distortion.

An alternative approach would be to use a template matching approach. Here, one would define the ideal structure (e.g. *fcc* or *bcc*) in terms of its shape invariants and oriented in a preferred reference frame. A comparison with the shape invariants would define how close it is to the ideal structure, and then the rank 2 contractions of the rank 4 ST (eqs 54-56) would define the amount of misorientation. This avoids the explicit definition of the *Z* axis of the HS configuration and would identify the best match with a minimal rotation. A minor limitation of this is that the ideal geometry must be defined which will then have issues identifying the orientation of highly distorted geometries.

For more general applications, we favor a compromise approach. For each rank *n* tensor, we calculate the dot products with the \mathbf{v}_n^0 , \mathbf{v}_n^n and \mathbf{v}_n^{-n} tensors defined in the desired reference frame. By normalizing these with the magnitude of the rank *n* ST, these orientation functions will have values in the range of [-1, 1]. These are defined below:

$$O1I0(a) = N[M_1, v_1^0]_0 / (N[M_1, M_1]_0)^{1/2}$$

$$O1I1(a) = N[M_1, v_1^1]_0 / (N[M_1, M_1]_0)^{1/2} \quad (59)$$

$$O1I2(a) = N[M_1, v_1^{-1}]_0 / (N[M_1, M_1]_0)^{1/2}$$

$$O2I0(a) = N[M_2, v_2^0]_0 / (N[M_2, M_2]_0)^{1/2}$$

$$O2I1(a) = N[M_2, v_2^2]_0 / (N[M_2, M_2]_0)^{1/2} \quad (60)$$

$$O2I2(a) = N[M_2, v_2^{-2}]_0 / (N[M_2, M_2]_0)^{1/2}$$

$$\begin{aligned}
O3I0(a) &= N[M_3, v_3^0]_0 / (N[M_3, M_3]_0)^{1/2} \\
O3I1(a) &= N[M_3, v_3^3]_0 / (N[M_3, M_3]_0)^{1/2} \\
O3I2(a) &= N[M_3, v_3^{-3}]_0 / (N[M_3, M_3]_0)^{1/2}
\end{aligned} \tag{61}$$

$$\begin{aligned}
O4I0(a) &= N[M_4, v_4^0]_0 / (N[M_4, M_4]_0)^{1/2} \\
O4I1(a) &= N[M_4, v_4^4]_0 / (N[M_4, M_4]_0)^{1/2} \\
O4I2(a) &= N[M_4, v_4^{-4}]_0 / (N[M_4, M_4]_0)^{1/2}
\end{aligned} \tag{62}$$

3. Discussion

3.1. Choosing the size of the Gaussian neighborhood

The size of the Gaussian neighborhood, i.e., the value of σ , will obviously affect the magnitudes and relative values of the SFDs. Figure 10 shows the SFDs, P_4^0 and P_3^0 (normalized to their maximum values), for 0 K *fcc* and *hcp* (in panel a) and *bcc* and Diamond (abbreviated as DIA, in panel b) as function of the σ normalized by the nearest-neighbor distance (r_{NN}). The vertical lines in Fig. 3 shows the choice of σ corresponding to $(2\pi)^{3/2}\sigma^3 = V_a$ (solid line) or $4/3\pi\sigma^3 = V_a$ (dotted line), V_a where is the per-atom volume calculated using the equilibrium lattice constant. In case that the underlying lattice structure is not known or does not exist, V_a can be approximated locally using a spherical neighborhood or globally using the volume of the simulation cell. The following observations can be made from Fig. 10: (1) There exists an optimal value for σ which maximizes the SFDs, thus maximizing the amount of information that can be extracted from the neighborhood moments (2) The optimal value of σ for *fcc*, *hcp* (dense, close packed structures), *bcc* and *dia* (less dense structures) are close to the solid line where one approximates the volume of atom using a Gaussian i.e., a normalization of $(2\pi)^{3/2}$ (3) The distribution of SFDs tend to get broader for less dense structures and also with increase in value of n . (4) Using the normalization of $4/3\pi$ for V_a , which is equivalent to approximating the atoms as spheres in contact, is a poor choice as the SFDs provide very little information with this choice of σ .

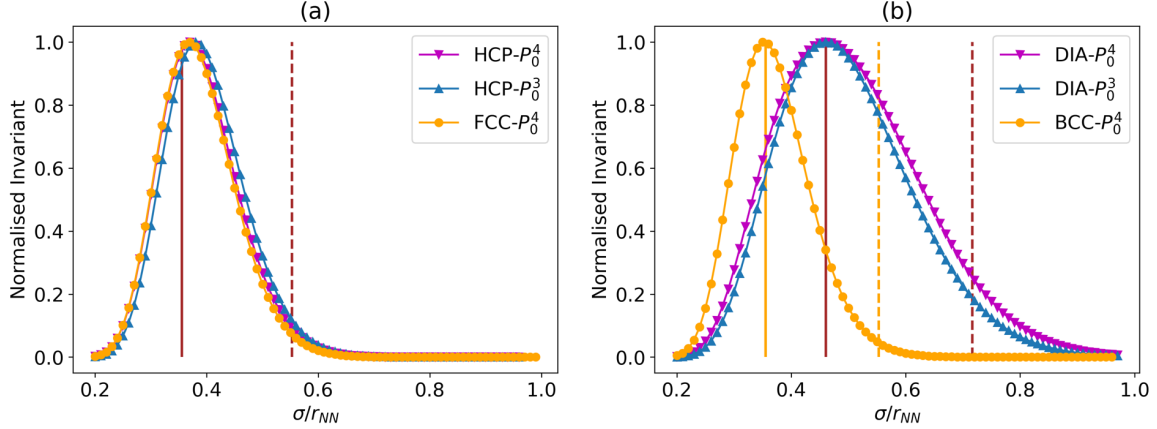


Figure 10: Normalized SFDs as a function of the size of the Gaussian neighborhood for crystals in their ideal 0 K structure. (a) FCC and HCP (b) BCC and Diamond (DIA). See text for definitions of solid and dotted vertical lines.

The presence of an optimum σ for the calculating the SFDs is easy to rationalize: If the width of the neighborhood is very small, no neighbors are detected and the SFDs quickly go to zero. Conversely, too many neighbors are included if the width is too large *i.e.*, the neighborhood becomes isotropic and the SFDs rapidly goes to zero. We subsequently employ the choice of σ corresponding to $(2\pi)^{3/2} \sigma^3 = V_a$ for all the results presented in this manuscript. Such a Gaussian neighborhood includes mostly contributions from the first nearest neighbor shells and some from the second nearest neighbors, respectively, but contributions from further atoms fall off rapidly in significance. For an *fcc* structure in equilibrium, the contribution is down to 10^{-6} by the 4th nearest-neighbor shell. Note that the SOAP/GAP analysis treats σ as an arbitrary value, typically 0.5 Å, for both amorphous²¹ and crystalline¹⁹ systems.

4. Results

In this section, we present some applications of the SFD analysis to MD simulations of defect-free and defective crystals. All MD simulations were performed using the LAMMPS⁵⁸ molecular dynamics software. All analysis involving Common Neighbor Analysis, Centro symmetry parameter, and Dislocation Extraction Algorithm (DXA) were performed using the OVITO⁵⁹ software, which was also used for visualizing atomic geometries.

4.1. Defect-free crystals at finite temperature

Figure 11 demonstrates how atoms in different defect-free crystal structures at finite temperatures are distinguished by the SFDs. Cu (FCC), Ta (BCC), Ti (HCP) and Si (DIA) were chosen as the representative systems. Finite temperature, equilibrium, molecular dynamics simulations were performed in the microcanonical ensemble for these systems using standard inter-atomic potentials.⁶⁰⁻⁶³ Each simulation cell contained between 10000 and 14000 atoms and was initially equilibrated to a temperature $T = 0.22 * T_m$, where T_m is the melting point. We then plotted the relative population of atoms vs. displacements in

two of our SFDs, $P_4^0 = N[4,4]_0$ and P_6^0 in figures 10a and 10b and $P_4^0 = N[4,4]_0$ and $P_6^0 = N[6,6]_0$ in figures 10c and 10d. The coordinates in figures 10a and 10c are from a single snapshot, while those in figures 10b and 10d were averaged over 5 snapshots, each of which was 50 fs apart. The color of a pixel on the panels in Fig. 10 denotes the number of atoms within a tenth of the coordinate of the pixel.

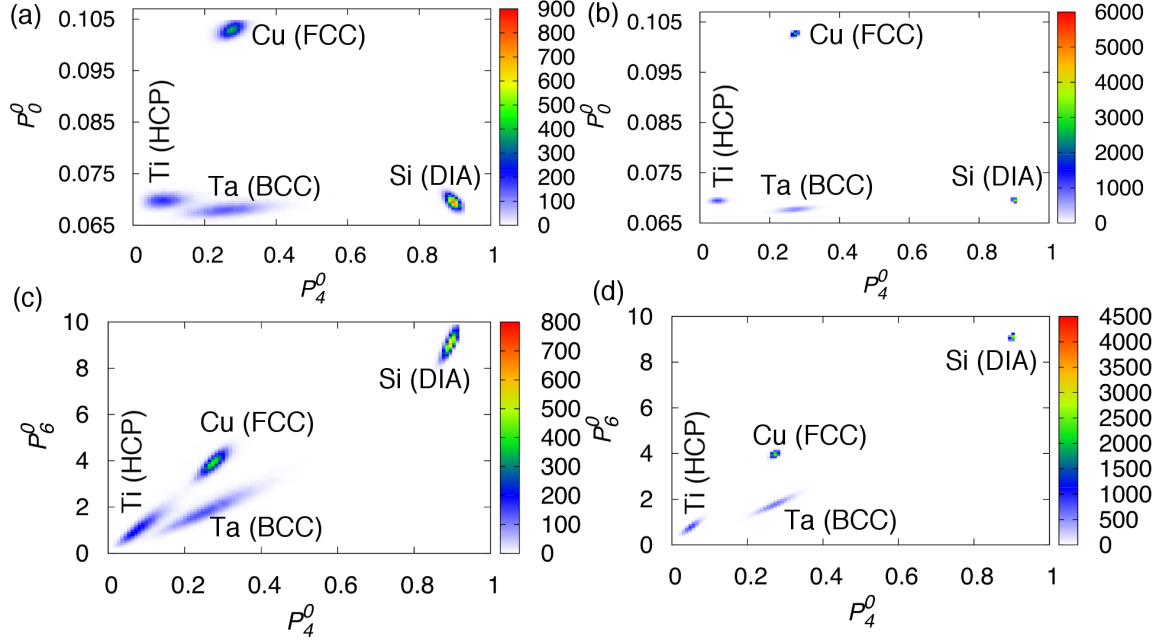


Figure 11: Population distribution of atoms in FCC, BCC, HCP and DIA crystals thermalized at $0.22 \cdot T_m$. (a) and (c) shows SFDs calculated using instantaneous coordinates (no time averaging of coordinates). (b) and (d) shows SFDs calculated using coordinates averaged over 5 snapshots, each of which was 50 fs apart.

It is readily apparent from panel (b) that the crystal structures can be easily distinguished using averaged coordinates and fourth-order SFDs. Without averaging, the distinction between BCC and FCC is slightly ambiguous in the space of fourth-order SFDs (panel (a)) but is clear with the addition of the sixth-order SFDs (panel (c)). The distinction between all the four crystal structures is very clear in panel (d), in which case, averaged coordinates are used to calculate P_4^0 and P_6^0 . This demonstrates the power of SFDs to characterize different crystal structures at finite temperatures with or without averaging of coordinates.

4.2. Volume-preserving deformation paths between crystal structures and melting

The behavior of SFDs during volume-preserving trigonal deformation and tetragonal deformation (along the Bain path) of the FCC structure was investigated. Figure 12 shows the fourth-order shape SFDs as a function of the strain along the deformation axis, *i.e.* $\langle 111 \rangle$ and $\langle 100 \rangle$, for the trigonal path (panel (a)) and the Bain path (panel (b)) respectively. Note that these are volume-preserving deformations and therefore, we used a constant value for σ throughout the deformation.

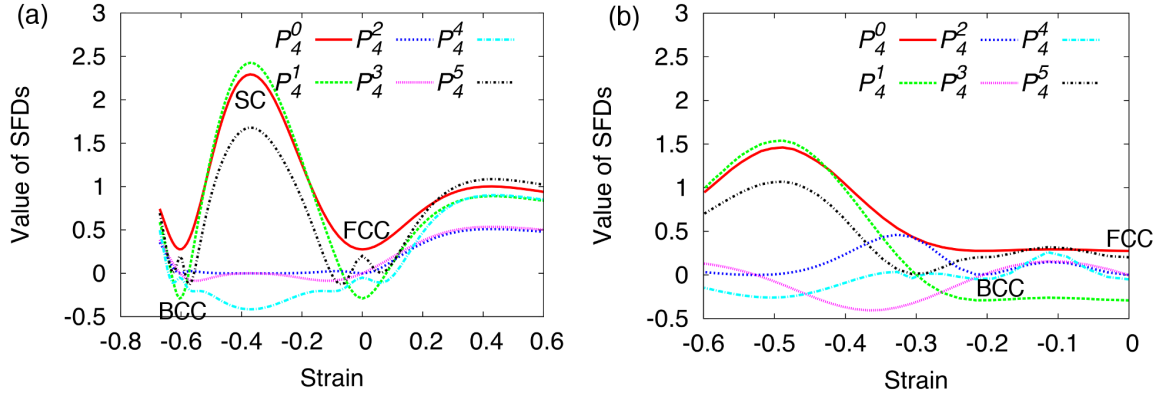


Figure 12: Fourth-order SFDs as a function of strain for volume-preserving deformations of an FCC lattice. (a) Deformation along the C_3 axis or the Trigonal path. (b) Deformation along the C_4 axis or the Bain path.

The SFDs smoothly track the deformation from FCC-SC-BCC in the trigonal path and FCC-BCC in the Bain path, with special structures (as noted in the panels) at the extremums. This demonstrates that SFDs can smoothly characterize deformations between different crystal structures, thus providing useful descriptors for phase transformations.

We also investigated the robustness of SFDs during melting. As a representative case, we studied homogeneous melting of Cu at $P=0$ atm. The simulation was performed with 3D periodic boundary conditions using a $12 \times 12 \times 12$ supercell with the C_4 axes oriented along the Cartesian x, y, and z directions. The simulation cell was initially equilibrated to a temperature of 300 K using a Nose-Hoover thermostat. Following the equilibration, NPT simulations were performed at $P=0$ atm using a heating rate of $1.0e^{12}$ Ks $^{-1}$. As the volume is not preserved, we used a variable σ for the SFD analysis, which was

calculated as $\sigma = \left[\left(\frac{V}{N} \right) / (2\pi)^{3/2} \right]^{1/3}$, where V is the instantaneous volume of the simulation cell and N is the total number of atoms. Figure 13 shows the variation of the third- (panel a) and fourth- (panel b) order shape SFDs as a function of the simulation time.

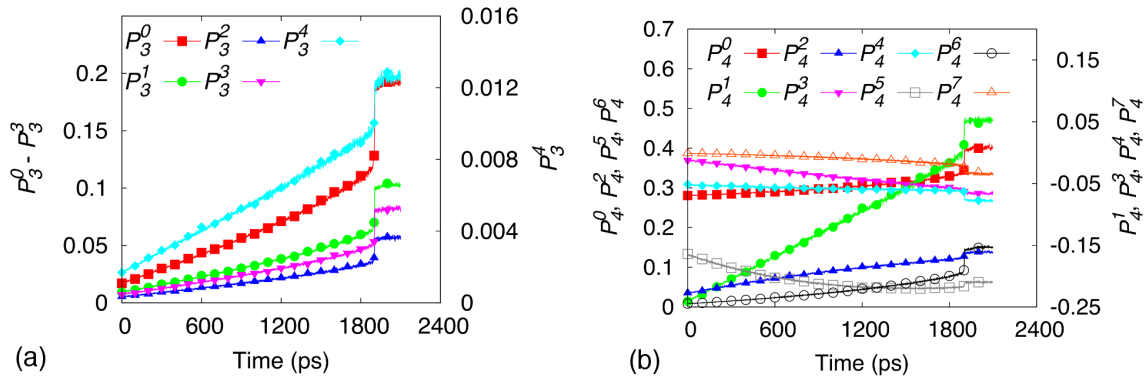


Figure 13: SFDs as a function of simulation time for homogeneous melting of Cu at $P=0$ atm. (a) Third-order SFDs. (b) Fourth-order SFDs.

The SFDs shown in Figure 13 are averaged over all the atoms in the simulation cell and are normalized using the respective maximum values over the entire simulation. As is evident from Figure 13, the third- and fourth- order descriptors are smooth and continuous till the point of melting with a discontinuous jump as the system goes through the solid-liquid phase transformation. This demonstrates that the SFDs are robust descriptors for melting.

4.3. Dislocations at 0 K

Plastic deformation in crystalline materials are closely linked to generation, propagation, and interaction of one-dimensional defects called dislocations. Figure 14 shows dislocation loops at $T=0$ K undergoing expansion under shear stress in Ta (BCC) (panel a) and Cu (FCC) (panel b).

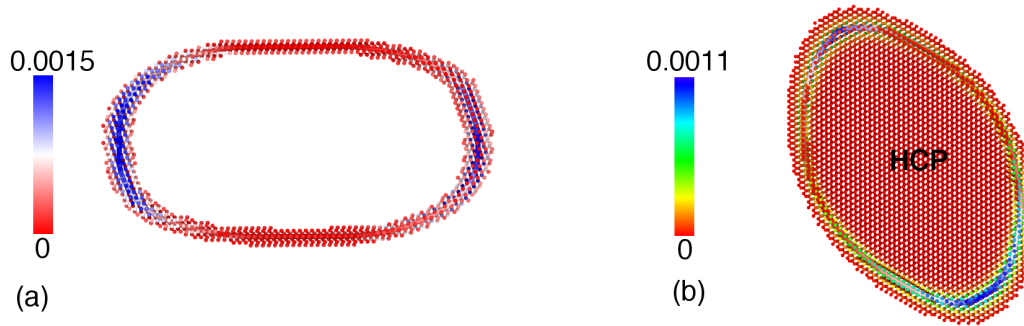


Figure 14: Expanding dislocation loops identified using third-order SFDs. The atoms are colored according to P_3^4 . The solid lines are dislocation lines identified by DXA. (a) Ta (BCC) and (b) Cu (FCC). The atoms in the stacking fault are also shown in (b).

Atoms were filtered using the criteria $P_3^0 > 0.009$ in panel a and $P_3^0 > 0.0005$ in panel b. In both cases the atoms are colored according to P_3^4 . Also shown in the figures is dislocation line identified by the DXA^{12, 13, 64} colored according to screw (red)/ edge (blue) character of the dislocation loop. It is evident that P_3^0 , the SFD which characterizes net third-order deformation is able to distinguish atoms in the dislocation core and stacking fault from nascent BCC/FCC atoms. It can also be seen that P_3^4 , which measures the net dipole of the gradient in the local number density, is sensitive to the character of the dislocation. Regions of the loop with an edge character have a relatively large value for P_3^4 (blue color in both panel a and b), thus providing a metric to distinguish between screw and edge dislocations. This is easy to understand, as edge dislocation cores will have a strong gradient perpendicular to the glide plane in the local number density. Thus, the third-order SFDs, which essentially measure third-order gradients in the number density, are able to identify dislocation cores and their edge/screw character. This follows from the fact that third-order SFDs characterize deformations that are represented using strain gradients defined in continuum mechanics, which are in turn directly related to the curvature of the crystal lattice (or equivalently elements of the Nye tensor⁶⁵). We note that determination of slip planes and Burger's vectors of the dislocations are possible with the use of the orientation SFDs but we defer that part to a subsequent publication.

4.4. Machine learning analysis of finite temperature MD simulations

Our final test was to apply machine learning classification algorithms (*i.e.*, unsupervised learning) to automate detection of defect structures in a finite temperature MD simulation. The SFD basis comprise a natural descriptor set for classification algorithms. As a test case, we performed MD simulations of isothermal compression of Cu along [001], with a barostat applied to [100] and [010] directions to maintain zero normal stresses. Simulations were performed at $T= 77$ K and 300 K, at a constant strain rate of $1e^9$ s⁻¹. The initial simulation cell consisted of a 34×34×34 cube with a total of 157216 atoms and was equilibrated in a canonical ensemble using a Nose-Hoover thermostat for 50 ps before the start of deformation. The simulation cell was deformed to a total strain of 12% to generate defective structures. This was followed by a 100 ps long equilibration in the micro-canonical ensemble to achieve the steady state defect structures.

Among the variety of classification algorithms available, we chose the Gaussian Mixture Model (GMM),⁶⁶ as implemented in Scikit-learn,⁶⁷ for our analysis. GMMs assume that the underlying data can be represented using a mixture of m Gaussians, where m is a hyper-parameter specified by the user. We tried $m= 4-10$ and used the Silhouette criterion to evaluate the quality of the resulting classes. For the 77 K case, $m=4$ was predicted to be optimal. Although $m=3$ was predicted to be optimal for the 300 K case, this did not provide a clean classification of the defect structures and therefore we used the next best set of classes given by $m=4$. The unknown parameters of the 4 Gaussians are estimated from the training data using the well-known expectation-maximization algorithm.⁶⁶ We trained the GMM classifiers using six equilibrium snapshots (≈ 950000 atomic geometries), obtained by time-averaging the atomic coordinates over 240 fs (60 snapshots, 4 fs apart) for 300 K and 120 fs (30 snapshots, 4 fs apart) for 77 K. For the purposes of this study, we used a 4th order expansion. We did not use the orientation SFDs and therefore our descriptors space consisted of 19 SFDs/atom describing the shape and size of the local atomic environments. Training and prediction were performed using the first few principal components of the SFDs (15 for 77 K and 13 for 300 K) which accounted for 99.999% variance in the training data. The four classes, that resulted from the GMM training, were identified as ‘deformed FCC’, ‘dislocations’, HCP and a ‘gradient’ class which did not belong to any known defect type. Raw classifications from the trained GMM were slightly noisy, and therefore, we performed a smoothing procedure by re-assigning the class of an atom based on the class which majority of the 12 nearest-neighbors belong to. Atoms belonging to the ‘dislocations’ class identified by the trained GMM classifier (after smoothing) on a snapshot that was not part of the training set are shown in Figure 15 (panels a and b at 77K, and panel c at 300 K). Also shown are the dislocation lines identified by the DXA implemented in OVITO.

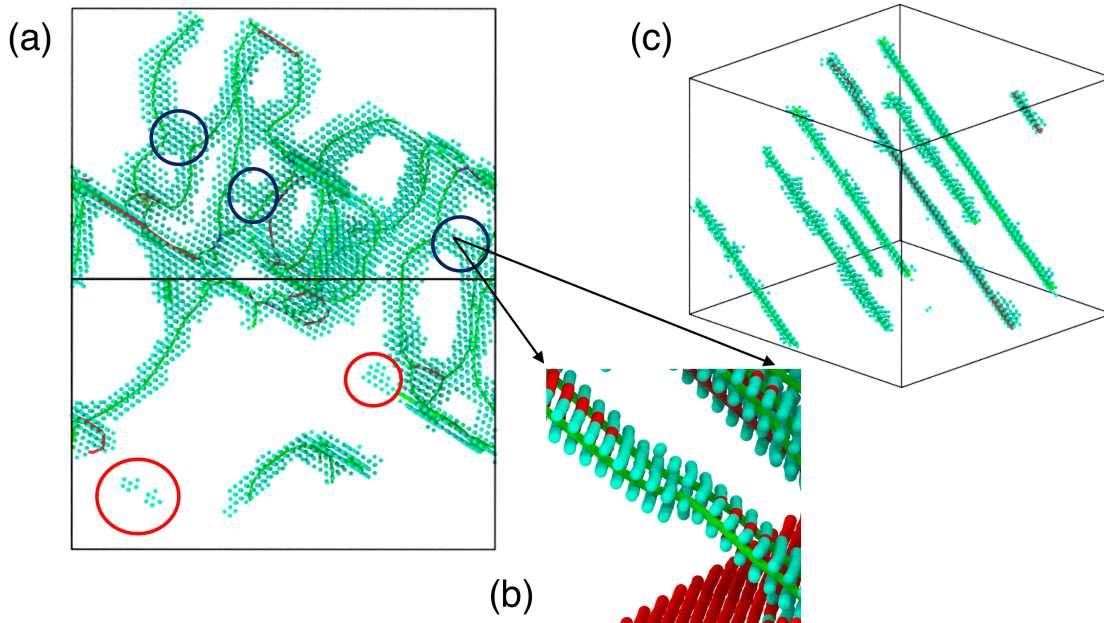


Figure 15: Dislocation structures predicted by trained Gaussian Mixture Model classifier along with dislocation lines identified by DXA. (a) All atoms in the dislocation structure at 77 K (b) A zoom-in of the jog on the Shockley partial at 77 K. Red atoms are in HCP configuration (c) All atoms in the dislocation structure at 300 K.

It is evident from Figures 15(a) that most of the atoms in this cluster belongs to core of the dislocations, which are also identified by DXA. Note that the trained GMM classifier identifies additional structures as part of this cluster at 77 K (Figure 15(a)): Atoms which are demarcated using dark blue circles in Figure 15(a) are jogs on Shockley dislocations and these are not identified as part of the dislocation network by DXA. A zoom-in of one of these jogs is shown in Figure 15(b), where the jog in the Shockley partial is clearly visible (atoms that are colored red in panel b are in HCP configuration). Atoms which are demarcated using red circles in Figure 15(a) are atoms surrounding vacancies formed during plastic deformation. The atoms belonging Figure 15(c) shows the dislocation cluster, identified using the trained GMM classifier, for the 300 K simulation. Due to the thermal activation at 300 K, the locks/intersection of dislocations are unzipped and the final structure consists of straight dislocations threading through the periodic boundaries. The dislocation structure predicted by trained GMM classifier at 300 K is in good agreement with the prediction by DXA. Methodology for identifying burgers vectors and slip planes of these dislocation structures using orientations SFDs will be considered in a subsequent publication.

Figure 16 shows atoms belonging to ‘HCP cluster’ (red) along with atoms in the dislocation structure (green) at 77 K (panel a) and 300 K (panel b).

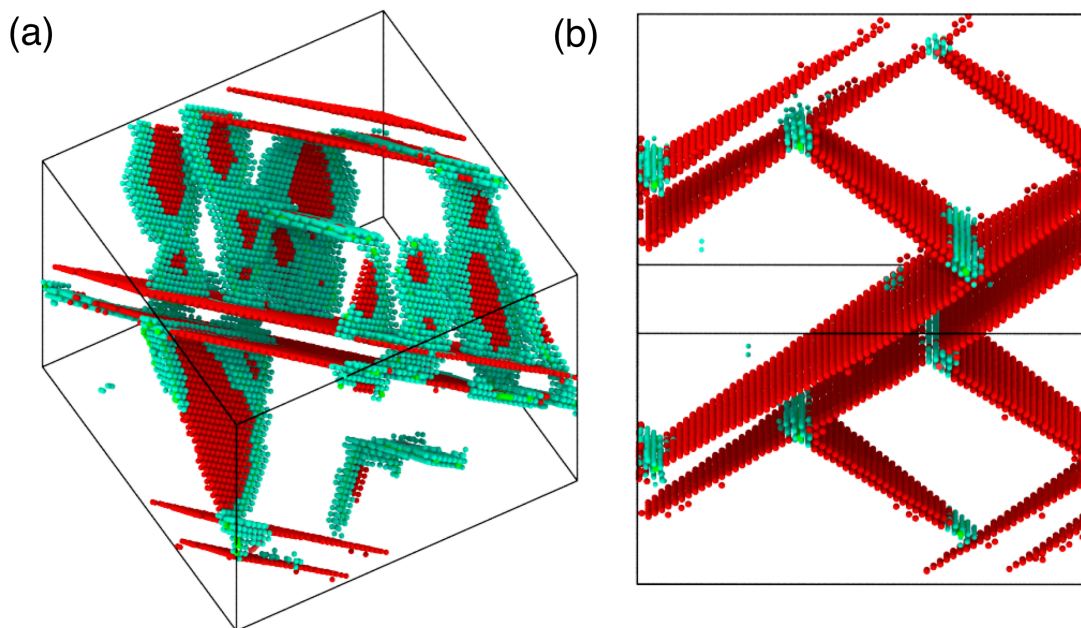


Figure 16: HCP atoms (red) predicted by the trained Gaussian Mixture Model Classifier along with atoms in the dislocation cluster. (a) 77 K (b) 300 K.

HCP atoms is present as part of stacking faults bounded by Shockley partials and also twin boundaries. In comparison with Adaptive Common Neighbor Analysis, our analysis predicts a lower number of HCP atoms: 5.6% (compared to 7.5%) at 77 K and 8.9% (compared to 9.9%) at 300 K. We have not performed a detailed analysis on the origin of these differences. We note here that classification using GMM performed better compared to other clustering algorithms such as DBSCAN⁶⁸ and K-means,⁶⁶ possibly due to the fact that the SFD distributions resulting from thermal vibrations are approximately Gaussian distributed. Our initial tests using orientation SFDs for classification showed that the twinned FCC atoms can be easily separated from uni-axially compressed FCC but defer that to a subsequent publication.

5. Conclusions

We developed a complete and symmetry-adapted set of descriptors, referred to as Strain Functional Descriptors (SFDs), for characterizing atomistic geometries. Using a Gaussian kernel, which has been shown to be the least-biased kernel for localizing information, discrete atomistic quantities are expressed as continuous functions. The SFDs are derived from n^{th} order central moments (*i.e.*, gradients) of the continuum representation of the local number density using techniques from group theory. The SFDs characterize atomic environments in terms of shape, size, and orientation of local neighborhood and can identify presence/absence of symmetry elements. We show that the SFDs can be used to distinguish between different crystal symmetries, characterize phase transformations, and identify defect structures in finite temperature MD simulations. We also coupled SFDs to unsupervised machine learning techniques (classification algorithms) and demonstrated their ability to automatically identify complex dislocation networks, stacking faults, and vacancies in finite temperature MD simulation data. These classifiers can, in principle, be

trained using small scale (hundreds of thousands of atoms) simulations, which can in turn be used for automated, *on-the-fly*, analysis of extreme-scale atomistic simulations.

Appendix A: Relationship of orientation tensor products to Euler angles

We start by defining an arbitrary rank 2 traceless tensor in its diagonal Cartesian form:

$$(A.1) \quad \mathbf{M}_{DT} = M \begin{bmatrix} v_2^2 \sin \psi_M - \frac{1}{2}v_2^0 \cos \psi_M & 0 & 0 \\ 0 & -v_2^2 \sin \psi_M - \frac{1}{2}v_2^0 \cos \psi_M & 0 \\ 0 & 0 & v_2^0 \cos \psi_M \end{bmatrix}$$

This tensor has a magnitude M and a skewness angle of ψ_M . It can then be rotated to an arbitrary frame using the Euler rotation matrix \mathbf{E}_r , using the *zyz* convention used by Edmonds (rotate about the initial z axis by α , then rotate β about the new y' axis, and then rotate γ about the new z'' axis).²⁹

$$(A.2) \quad \mathbf{E}_r = \begin{bmatrix} \cos \beta \cos \alpha \cos \gamma - \sin \alpha \sin \gamma & \cos \beta \sin \alpha \cos \gamma + \cos \alpha \sin \gamma & -\sin \beta \cos \gamma \\ -\cos \beta \cos \alpha \sin \gamma - \sin \alpha \cos \gamma & -\cos \beta \sin \alpha \sin \gamma + \cos \alpha \cos \gamma & \sin \beta \sin \gamma \\ \sin \beta \cos \alpha & \sin \beta \sin \alpha & \cos \beta \end{bmatrix}$$

The arbitrarily oriented tensor is then defined as:

$$(A.3) \quad \mathbf{M}_2 = \mathbf{E}_r \mathbf{M}_{DT} \mathbf{E}_r^T$$

For simplicity, we then evaluate the contractions between this tensor and the two tensors that define the external axis frame: \mathbf{v}_2^0 and \mathbf{v}_2^2 . These are in bold to emphasize that they are tensors, though their only non-zero components are v_2^0 and v_2^2 , respectively. The norms of both tensors are 1. Those contractions are:

$$(A.4) \quad \mathbf{N}[\mathbf{M}_2, \mathbf{v}_2^0]_0 = \frac{1}{4} \left((1 + 3 \cos 2\beta) \cos \psi_M + 2\sqrt{3} \cos 2\alpha \sin^2 \beta \sin \psi_M \right)$$

$$(A.5) \quad \mathbf{N}[\mathbf{M}_2, \mathbf{v}_2^2]_0 = \frac{1}{4} \left((\cos 2\alpha \cos 2\gamma (3 + \cos 2\beta) - 4 \sin 2\alpha \sin 2\gamma \cos \beta) \sin \psi_M + 2\sqrt{3} \cos 2\gamma \sin^2 \beta \cos \psi_M \right)$$

$$(A.6) \quad \mathbf{N}[\mathbf{N}[\mathbf{M}_2, \mathbf{v}_2^0]_2, \mathbf{v}_2^0]_0 = \frac{1}{12\sqrt{2}} \left(\sqrt{3}(1 + 3 \cos 2\beta) \cos \psi_M + 6 \cos 2\alpha \sin^2 \beta \sin \psi_M \right)$$

$$(A.7) \quad \mathbf{N}[\mathbf{N}[\mathbf{M}_2, \mathbf{v}_2^2]_2, \mathbf{v}_2^2]_0 = -\frac{1}{12\sqrt{2}} \left(\sqrt{3}(1 + 3 \cos 2\beta) \cos \psi_M + 6 \cos 2\alpha \sin^2 \beta \sin \psi_M \right)$$

$$(A.8) \quad \mathbf{N} \left[\mathbf{N}[\mathbf{M}_2, \mathbf{v}_2^0]_2, \mathbf{M}_2 \right]_0 = \frac{1}{12\sqrt{2}} \left(\sqrt{3}(1 + 3 \cos 2\beta) \cos 2\psi_M - 6 \cos 2\alpha \sin^2 \beta \sin 2\psi_M \right)$$

$$(A.9) \quad \mathbf{N} \left[\mathbf{N}[\mathbf{M}_2, \mathbf{v}_2^2]_2, \mathbf{M}_2 \right]_0 = \frac{1}{24} \left(4\sqrt{6} \cos \beta \sin 2\alpha \sin 2\gamma \sin 2\psi_M + \sqrt{2} \cos 2\gamma (6 \cos 2\psi_M \sin^2 \beta - \sqrt{3} \cos 2\alpha (3 + \cos 2\beta) \sin 2\psi_M) \right)$$

We note two relationships between two pairs of these terms (A.4 and A.6, and A.6 and A.7):

$$(A.10) \quad \mathbf{N}[\mathbf{M}_2, \mathbf{v}_2^0]_0 = \sqrt{6} \mathbf{N} \left[\mathbf{N}[\mathbf{M}_2, \mathbf{v}_2^0]_2, \mathbf{v}_2^0 \right]_0$$

$$(A.11) \quad \mathbf{N} \left[\mathbf{N}[\mathbf{M}_2, \mathbf{v}_2^0]_2, \mathbf{v}_2^0 \right]_0 = -\mathbf{N} \left[\mathbf{N}[\mathbf{M}_2, \mathbf{v}_2^2]_2, \mathbf{v}_2^2 \right]_0$$

This leaves four independent relationships in A.4, A.5, A.8 and A.9. Equations A.4 and A.8 can both be solved for $\cos 2\alpha$, and by equating those two forms and then solving $\cos 2\beta$ produces the following relationship.

$$(A.12) \quad \cos 2\beta = \frac{4 \sin 2\psi_M}{3 \sin 3\psi_M} \mathbf{N}[\mathbf{M}_2, \mathbf{v}_2^0]_0 + \frac{4\sqrt{6} \sin \psi_M}{3 \sin 3\psi_M} \mathbf{N} \left[\mathbf{N}[\mathbf{M}_2, \mathbf{v}_2^0]_2, \mathbf{M}_2 \right]_0 - \frac{1}{3}$$

This defines $\cos 2\beta$ in terms of known quantities. This can be substituted back into the previous relationships for $\cos 2\alpha$ to also define it in terms of those same quantities.

$$(A.13) \quad \cos 2\alpha = \frac{\sqrt{3}(\cos 2\psi_M \mathbf{N}[\mathbf{M}_2, \mathbf{v}_2^0]_0 - \sqrt{6} \cos \psi_M \mathbf{N}[\mathbf{N}[\mathbf{M}_2, \mathbf{v}_2^0]_2, \mathbf{M}_2]_0)}{\sin 3\psi_M - \sin 2\psi_M \mathbf{N}[\mathbf{M}_2, \mathbf{v}_2^0]_0 - \sqrt{6} \sin \psi_M \mathbf{N}[\mathbf{N}[\mathbf{M}_2, \mathbf{v}_2^0]_2, \mathbf{M}_2]_0}$$

Equations A.5 and A.9 can be rearranged to isolate the terms containing $\sin 2\gamma$ and thereby eliminate them. The remaining expression contains only terms with $\cos 2\gamma$ which produces:

$$(A.14) \quad \cos 2\gamma = \frac{\sqrt{3}(\sin 2\psi_M \mathbf{N}[\mathbf{M}_2, \mathbf{v}_2^2]_0 + \sqrt{6} \sin \psi_M \mathbf{N}[\mathbf{N}[\mathbf{M}_2, \mathbf{v}_2^2]_2, \mathbf{M}_2]_0)}{\sin 3\psi_M - \sin 2\psi_M \mathbf{N}[\mathbf{M}_2, \mathbf{v}_2^0]_0 - \sqrt{6} \sin \psi_M \mathbf{N}[\mathbf{N}[\mathbf{M}_2, \mathbf{v}_2^0]_2, \mathbf{M}_2]_0}$$

This defines the process for defining the rotation of an arbitrary rank 2 tensor into the diagonal HS form. We note that this process only allows α , β , and γ to be defined only over the range of $0-\pi$. This lack of uniqueness arises because the \pm directions in the axis directions are not distinguishable in the rank 2 framework (i.e. $(+z)^2 = (-z)^2$). This same rotation process (defined as a rank n tensor) can be applied to an arbitrary rank n tensor to transform it to its pseudo-diagonal HS form.

Next we consider defining the reference axis frame as a single tensor with some specified skewness angle ψ_0 :

$$(A.15) \quad \mathbf{R}_2 = \cos \psi_0 \mathbf{v}_2^0 + \sin \psi_0 \mathbf{v}_2^2$$

One can then express the three contractions between this and an arbitrary rank 2 tensor \mathbf{M}_2 in terms of eqs A.4-9. These can be reduced to:

$$(A.16) \quad \mathbf{N}[\mathbf{M}_2, \mathbf{R}_2]_0 = \cos \psi_0 \mathbf{N}[\mathbf{M}_2, \mathbf{v}_2^0]_0 + \sin \psi_0 \mathbf{N}[\mathbf{M}_2, \mathbf{v}_2^2]_0$$

$$(A.17) \quad \mathbf{N}[\mathbf{N}[\mathbf{M}_2, \mathbf{R}_2]_2, \mathbf{M}_2]_0 = \cos \psi_0 \mathbf{N}[\mathbf{N}[\mathbf{M}_2, \mathbf{v}_2^0]_2, \mathbf{M}_2]_0 + \sin \psi_0 \mathbf{N}[\mathbf{N}[\mathbf{M}_2, \mathbf{v}_2^2]_2, \mathbf{M}_2]_0$$

$$(A.18) \quad \mathbf{N}[\mathbf{N}[\mathbf{M}_2, \mathbf{R}_2]_2, \mathbf{R}_2]_0 = \frac{1}{\sqrt{6}} \cos 2\psi_0 \mathbf{N}[\mathbf{M}_2, \mathbf{v}_2^0]_0 - \frac{1}{\sqrt{6}} \sin 2\psi_0 \mathbf{N}[\mathbf{M}_2, \mathbf{v}_2^2]_0$$

Additionally, the value of ψ_0 can be defined from

$$(A.19) \quad \cos 3\psi_0 = \sqrt{\frac{7}{2\sqrt{5}} \frac{\mathbf{N}[\mathbf{N}[\mathbf{R}_2, \mathbf{R}_2]_2, \mathbf{R}_2]_0}{(\mathbf{N}[\mathbf{R}_2, \mathbf{R}_2]_0)^{3/2}}}$$

The significance of the form $3\psi_0$ comes from eq B.1. Numerically, solutions of ψ_0 , $\psi_0 + 2\pi/3$, and $\psi_0 + 4\pi/3$ are all equivalent. When such variations are substituted into A.1, the result is an interchange of the x, y and z axes. Consequently, a unique inversion of eqs A.16-20 to obtain the rotation angles α , β , and γ requires some additional information such as best alignment with the external axis frame, or best alignment between the two HS framework of two tensors. Such choices can be motivated by the particular application, but the intrinsic information is contained in 2 and 3-way contractions of the rank 2 tensors.

Method

All mathematical manipulations were performed using the *Mathematica* software package (13.2) available from Wolfram. The phase conventions for the spherical harmonics and Clebsch-Gordan factors are the same as those used by Edmonds.²⁹ Notebooks of these manipulations can be obtained from EMK by reasonable request.

Acknowledgements

All the authors gratefully acknowledge the support of the U.S. Department of Energy through the LDRD Program at Los Alamos National Laboratory. The work was initialized under XWG8 and the work completed under XWH4 and XX9A. NM acknowledges the Center for Non-Linear Studies at LANL for support, and Kipton Barros and Nick Lubbers for fruitful discussions. EMK dedicates this work to Prof. Thomas J. Meyer (Univ. North Carolina at Chapel Hill, retired) for encouraging him in exploring this area of science.⁵⁵

References

- (1) Lewis, A. C.; Suh, C.; Stukowski, M.; Geltmacher, A. B.; Spanos, G.; Rajan, K. Quantitative Analysis and Feature Recognition in 3-D Microstructural Data Sets. *JOM* **2006**, 52-56.
- (2) Stukowski, A. Computational Analysis Methods in Atomistic Modeling of Crystals. *JOM* **2013**, 66 (3), 399-407. DOI: 10.1007/s11837-013-0827-5.
- (3) Honeycutt, J. D.; Andersen, H. C. Molecular Dynamics Study of Melting and Freezing of Small Lennard- Jones Clusters. *Journal of Physical Chemistry* **1987**, 91, 4950-4963.
- (4) Stukowski, A. Structure identification methods for atomistic simulations of crystalline materials. *Modelling and Simulation in Materials Science and Engineering* **2012**, 20 (4), 045021. DOI: 10.1088/0965-0393/20/4/045021.
- (5) Kelchner, C. L.; Plimpton, S. J.; Hamilton, J. C. Dislocation nucleation and defect structure during surface indentation. *Phys. Rev. B* **1998**, 58, 11085-11088.
- (6) Steinhardt, P. J.; Nelson, D., R.; Ronchetti, M. Bond-orientational order in liquids and glasses. *Physical Review B* **1983**, 28 (2), 784-805.
- (7) Ackland, G. J.; Jones, A. P. Applications of local crystal structure measures in experiment and simulation. *Physical Review B* **2006**, 73 (5), 054104. DOI: 10.1103/PhysRevB.73.054104.
- (8) Maras, E.; Trushin, O.; Stukowski, A.; Ala-Nissila, T.; Jónsson, H. Global transition path search for dislocation formation in Ge on Si(001). *Computer Physics Communications* **2016**, 205, 13-21. DOI: 10.1016/j.cpc.2016.04.001.
- (9) Voronoi, G. Nouvelles applications des parametres continus a la theorie des formes quadratiques. II. *J. Reine Angew. Math.* **1908**, 134, 198-287.
- (10) Keys, A. S.; Iacovella, C. R.; Glotzer, S. C. Characterizing complex particle morphologies through shape matching: Descriptors, applications, and algorithms. *Journal of Computational Physics* **2011**, 230 (17), 6438-6463. DOI: 10.1016/j.jcp.2011.04.017.
- (11) Larsen, P. M.; Schmidt, S.; Schiøtz, J. Robust structural identification via polyhedral template matching. *Modelling and Simulation in Materials Science and Engineering* **2016**, 24 (5). DOI: 10.1088/0965-0393/24/5/055007.
- (12) Stukowski, A.; Bulatov, V. V.; Arsenlis, A. Automated identification and indexing of dislocations in crystal interfaces. *Modelling and Simulation in Materials Science and Engineering* **2012**, 20 (8). DOI: 10.1088/0965-0393/20/8/085007.
- (13) Stukowski, A. A triangulation-based method to identify dislocations in atomistic models. *Journal of the Mechanics and Physics of Solids* **2014**, 70, 314-319. DOI: 10.1016/j.jmps.2014.06.009.
- (14) Begau, C.; Hua, J.; Hartmaier, A. A novel approach to study dislocation density tensors and lattice rotation patterns in atomistic simulations. *Journal of the Mechanics and Physics of Solids* **2012**, 60 (4), 711-722. DOI: 10.1016/j.jmps.2011.12.005.
- (15) Lazar, E. A.; Han, J.; Srolovitz, D. J. Topological framework for local structure analysis in condensed matter. *Proc Natl Acad Sci U S A* **2015**, 112 (43), E5769-5776. DOI: 10.1073/pnas.1505788112.
- (16) Rosenbrock, C. W.; Homer, E. R.; Csányi, G.; Hart, G. L. W. Discovering the building blocks of atomic systems using machine learning: application to grain

- boundaries. *npj Computational Materials* **2017**, 3 (1), 1-7. DOI: 10.1038/s41524-017-0027-x.
- (17) Bartok, A. P.; Payne, M. C.; Kondor, R.; Csanyi, G. Gaussian approximation potentials: the accuracy of quantum mechanics, without the electrons. *Phys. Rev. Lett.* **2010**, 104 (13), 136403. DOI: 10.1103/PhysRevLett.104.136403.
- (18) Bartók, A. P.; Kondor, R.; Csányi, G. On representing chemical environments. *Physical Review B* **2013**, 87 (18). DOI: 10.1103/PhysRevB.87.184115.
- (19) Szlachta, W. J.; Bartók, A. P.; Csányi, G. Accuracy and transferability of Gaussian approximation potential models for tungsten. *Physical Review B* **2014**, 90 (10). DOI: 10.1103/PhysRevB.90.104108.
- (20) De, S.; Bartok, A. P.; Csanyi, G.; Ceriotti, M. Comparing molecules and solids across structural and alchemical space. *Phys Chem Chem Phys* **2016**, 18 (20), 13754-13769. DOI: 10.1039/c6cp00415f.
- (21) Deringer, V. L.; Csányi, G. Machine learning based interatomic potential for amorphous carbon. *Physical Review B* **2017**, 95 (9). DOI: 10.1103/PhysRevB.95.094203.
- (22) Shapeev, A. V. Moment Tensor Potentials: A Class of Systematically Improvable Interatomic Potentials. *Multiscale Modeling & Simulation* **2016**, 14 (3), 1153-1173. DOI: 10.1137/15m1054183.
- (23) Drautz, R. Atomic cluster expansion for accurate and transferable interatomic potentials. *Physical Review B* **2019**, 99 (1), 014104. DOI: 10.1103/PhysRevB.99.014104.
- (24) Musil, F.; Grisafi, A.; Bartók, A. P.; Ortner, C.; Csányi, G.; Ceriotti, M. Physics-Inspired Structural Representations for Molecules and Materials. *Chemical Reviews* **2021**, 121 (16), 9759-9815. DOI: 10.1021/acs.chemrev.1c00021.
- (25) Hu, M.-K. Visual Pattern Recognition by Moment Invariants. *IRE Transactions on Information Theory* **1962**, 8 (2), 179-187.
- (26) Sadjadi, F. A.; Hall, E. L. Three-Dimensional Moment Invariants. *IEEE Trans Pattern Anal Mach Intell* **1980**, PAMI-2 (2), 127-136.
- (27) Cyganski, D.; Orr, J. A. Applications of Tensor Theory to Object Recognition and Orientation Determination. *IEEE Trans. Patt. Analysis Machi. Intel.* **1985**, PAMI-7, 662-673.
- (28) Lo, C.-H.; Don, H.-S. 3-D Moment Forms: Their Construction and Application to Object Identification and Positioning. *IEEE Transactions on Pattern Analysis and Machine Intelligence* **1989**, 11 (10), 1053-1064. DOI: 10.1109/34.42836
- (29) Edmonds, A. R. Angular Momentum in Quantum Mechanics. *Princeton University Press, Princeton, NJ* **1974**, 3rd ed.
- (30) Jerphagnon, J.; Chemla, D.; Bonneville, R. The description of the physical properties of condensed matter using irreducible tensors. *Advances in Physics* **1978**, 27 (4), 609-650. DOI: 10.1080/00018737800101454.
- (31) Ennis, D. B.; Kindlmann, G. Orthogonal tensor invariants and the analysis of diffusion tensor magnetic resonance images. *Magn Reson Med* **2006**, 55 (1), 136-146. DOI: 10.1002/mrm.20741.
- (32) Kindlmann, G.; Ennis, D. B.; Whitaker, R. T.; Westin, C. F. Diffusion tensor analysis with invariant gradients and rotation tangents. *IEEE Trans Med Imaging* **2007**, 26 (11), 1483-1499. DOI: 10.1109/TMI.2007.907277.

- (33) Trott, C. R.; Hammond, S. D.; Thompson, A. P. SNAP: Strong Scaling High Fidelity Molecular Dynamics Simulations on Leadership-Class Computing Platforms. *Lecture Notes in Computer Science* **2014**, *8488*, 19-34.
- (34) Wood, M. A.; Thompson, A. P. Extending the accuracy of the SNAP interatomic potential form. *J Chem Phys* **2018**, *148* (24), 241721. DOI: 10.1063/1.5017641.
- (35) Podryabinkin, E. V.; Shapeev, A. V. Active learning of linearly parametrized interatomic potentials. *Computational Materials Science* **2017**, *140*, 171-180. DOI: 10.1016/j.commatsci.2017.08.031.
- (36) Daw, M. S.; Baskes, M. I. Embedded-atom method: Derivation and application to impurities, surfaces, and other defects in metals. *Physical Review B* **1984**, *29* (12), 6443-6453. DOI: 10.1103/PhysRevB.29.6443.
- (37) Baskes, M. I. Modified embedded-atom potentials for cubic materials and impurities. *Physical Review B* **1992**, *46* (5), 2727-2742. DOI: 10.1103/PhysRevB.46.2727.
- (38) Baskes, M. I.; Srinivasan, S. G.; Valone, S. M.; Hoagland, R. G. Multistate modified embedded atom method. *Physical Review B* **2007**, *75* (9). DOI: 10.1103/PhysRevB.75.094113.
- (39) Zimmerman, J. A.; Bammann, D. J.; Gao, H. Deformation gradients for continuum mechanical analysis of atomistic simulations. *Int. J. Sol. Struct.* **2009**, *46* (2), 238-253. DOI: 10.1016/j.ijsolstr.2008.08.036.
- (40) Falk, M. L.; Langer, J. S. Dynamics of viscoplastic deformation in amorphous solids. *Physical Review E* **1998**, *57* (6), 7192-7205.
- (41) Horstemeyer, M. F.; Baskes, M. I. Strain Tensors at the Atomic Scale. *Materials Research Society Symposium Proceedings* **2000**, *578*, 15-20.
- (42) Shimizu, F.; Ogata, S.; Li, J. Theory of Shear Banding in Metallic Glasses and Molecular Dynamics Calculations. *Materials Transactions* **2007**, *48* (11), 2923-2927. DOI: 10.2320/matertrans.MJ200769.
- (43) Gullett, P. M.; Horstemeyer, M. F.; Baskes, M. I.; Fang, H. A deformation gradient tensor and strain tensors for atomistic simulations. *Modelling and Simulation in Materials Science and Engineering* **2008**, *16* (1). DOI: 10.1088/0965-0393/16/1/015001.
- (44) Lafourcade, P.; Denoual, C.; Maillet, J.-B. Irreversible Deformation Mechanisms for 1,3,5-Triamino-2,4,6-Trinitrobenzene Single Crystal through Molecular Dynamics Simulations. *The Journal of Physical Chemistry C* **2018**, *122* (26), 14954-14964. DOI: 10.1021/acs.jpcc.8b02983.
- (45) Thompson, A. P.; Swiler, L. P.; Trott, C. R.; Foiles, S. M.; Tucker, G. J. Spectral neighbor analysis method for automated generation of quantum-accurate interatomic potentials. *J. Comp. Phys.* **2015**, *285*, 316-330. DOI: 10.1016/j.jcp.2014.12.018.
- (46) Lindeberg, T. Generalized Gaussian Scale-Space Axiomatics Comprising Linear Scale-Space, Affine Scale-Space and Spatio-Temporal Scale-Space. *J. Math. Imag. Vis.* **2010**, *40* (1), 36-81. DOI: 10.1007/s10851-010-0242-2.
- (47) Arroyo, M.; Ortiz, M. Local maximum-entropy approximation schemes: a seamless bridge between finite elements and meshfree methods. *Int. J. Num. Meth. Eng.* **2006**, *65* (13), 2167-2202. DOI: 10.1002/nme.1534.

- (48) Cyron, C. J.; Arroyo, M.; Ortiz, M. Smooth, second order, non-negative meshfree approximants selected by maximum entropy. *Int. J. Num. Meth. Eng.* **2009**, *79* (13), 1605-1632. DOI: 10.1002/nme.2597.
- (49) Grad, H. Note on N-Dimensional Hermite Polynomials. *Commun. Pure Appl. Math.* **1949**, *2* (4), 325-330.
- (50) Coope, J. A. R.; Snider, R. F.; McCourt, F. R. Irreducible Cartesian Tensors. *The Journal of Chemical Physics* **1965**, *43* (7), 2269-2275. DOI: 10.1063/1.1697123.
- (51) Coope, J. A. R.; Snider, R. F. Irreducible Cartesian Tensors. II. General Formulation. *Journal of Mathematical Physics* **1970**, *11* (3), 1003-1017. DOI: 10.1063/1.1665190.
- (52) Coope, J. A. R. Irreducible Cartesian Tensors. III. Clebsch - Gordan Reduction. *Journal of Mathematical Physics* **1970**, *11* (5), 1591-1612. DOI: 10.1063/1.1665301.
- (53) Aubert, G. An alternative to Wigner d-matrices for rotating real spherical harmonics. *AIP Advances* **2013**, *3* (6). DOI: 10.1063/1.4811853.
- (54) Cotton, F. A. *Chemical Applications of Group Theory*; John Wiley & Sons, 1990.
- (55) Kober, E. M.; Meyer, T. J. Concerning the Absorption Spectra of the Ions [M(bpy)₃]²⁺ (M = Fe, Ru, Os; bpy = 2,2'-Bipyridine). *Inorg. Chem.* **1982**, *21*, 3967-3977.
- (56) Luscher, D. J.; McDowell, D. L.; Bronkhorst, C. A. A second gradient theoretical framework for hierarchical multiscale modeling of materials. *International Journal of Plasticity* **2010**, *26* (8), 1248-1275. DOI: 10.1016/j.ijplas.2010.05.006.
- (57) Admal, N. C.; Marian, J.; Po, G. The atomistic representation of first strain-gradient elastic tensors. *Journal of the Mechanics and Physics of Solids* **2017**, *99*, 93-115. DOI: 10.1016/j.jmps.2016.11.005.
- (58) Plimpton, S. J. Fast Parallel Algorithms for Short-Range Molecular Dynamics. *J. Comput. Phys.* **1995**, *117*, 1-19.
- (59) Stukowski, A. Visualization and analysis of atomistic simulation data with OVITO—the Open Visualization Tool. *Modell. Simul. Mater. Sci. Eng.* **2010**, *18* (1), 015012. DOI: 10.1088/0965-0393/18/1/015012.
- (60) Mishin, Y.; Mehl, M. J.; Papaconstantopoulos, D. A.; Voter, A. F.; Kress, J. D. Structural stability and lattice defects in copper: Ab initio, tight-binding, and embedded-atom calculations. *Physical Review B* **2001**, *63* (22). DOI: 10.1103/PhysRevB.63.224106.
- (61) Tramontina, D.; Erhart, P.; Germann, T.; Hawreliak, J.; Higginbotham, A.; Park, N.; Ravelo, R.; Stukowski, A.; Suggit, M.; Tang, Y.; et al. Molecular dynamics simulations of shock-induced plasticity in tantalum. *High Energy Density Physics* **2014**, *10*, 9-15. DOI: 10.1016/j.hedp.2013.10.007.
- (62) Hennig, R. G.; Lenosky, T. J.; Trinkle, D. R.; Rudin, S. P.; Wilkins, J. W. Classical potential describes martensitic phase transformations between the α , β , and ω titanium phases. *Physical Review B* **2008**, *78* (5). DOI: 10.1103/PhysRevB.78.054121.
- (63) Stillinger, F. H.; Weber, T. A. Computer simulation of local order in condensed phases of silicon. *Phys. Rev. B* **1985**, *31*, 5262.

- (64) Stukowski, A.; Arsenlis, A. On the elastic–plastic decomposition of crystal deformation at the atomic scale. *Modelling and Simulation in Materials Science and Engineering* **2012**, *20* (3). DOI: 10.1088/0965-0393/20/3/035012.
- (65) Nye, J. F. Some Geometrical Relations in Dislocated Crystals. *Acta Metallurgica* **1953**, *1*, 153-162.
- (66) Bishop, C. M. *Pattern Recognition and Machine Learning (Information Science and Statistics)*; 2006.
- (67) Pedregosa, F.; Varoquaux, G.; Gramfort, A.; Michel, V.; Thirion, B.; Grisel, O.; Blondel, M.; Prettenhofer, P.; Weiss, R.; Dubourg, V.; et al. Scikit-learn: Machine Learning in Python. *J. Mach. Learn. Res.* **2011**, *12*, 2825-2830.
- (68) Sander, J.; Ester, M.; Kriegel, H.-P.; Xu, X. Density-Based Clustering in Spatial Databases: The Algorithm GDBSCAN and Its Applications. *Data Mining and Knowledge Discovery* **1998**, *2*, 169-194.

Supplemental Material

S.1: Transformation from tensor derivatives to traceless formulations

The second derivative of the weight function with respect to the \mathbf{r} vector, evaluated at $\mathbf{r} = \mathbf{r}_b$, generates a 3x3 matrix given below for the x , y and z components of the direction vector.

$$\sum_{b \neq a} \frac{\partial^2 w_a}{\partial \mathbf{r}^2} \Big|_{\mathbf{r}_b} = \sum_{b \neq a} \frac{\partial^2 \exp\left(-\frac{|\mathbf{r} - \mathbf{r}_a|^2}{2\sigma^2}\right)}{\partial \mathbf{r}^2} \Big|_{\mathbf{r}_b} = \frac{1}{\sigma^4} \sum_{b \neq a} \mathbf{D2} \exp\left(-\frac{r_{ab}^2}{2\sigma^2}\right)$$

$$\mathbf{D2} = \begin{bmatrix} x_{ab}^2 - \sigma^2 & x_{ab}y_{ab} & x_{ab}z_{ab} \\ x_{ab}y_{ab} & y_{ab}^2 - \sigma^2 & y_{ab}z_{ab} \\ x_{ab}z_{ab} & y_{ab}z_{ab} & z_{ab}^2 - \sigma^2 \end{bmatrix}$$

That matrix can then be separated into a portion that depends on the distance vector and one that depends only on σ . The former term can be simply identified as the outer product of the \mathbf{r}_{ab} vector with itself and the latter term is simply σ^2 times the 3x3 identify matrix, \mathbf{I}_2 .

$$\mathbf{D2} = \begin{bmatrix} x_{ab}^2 & x_{ab}y_{ab} & x_{ab}z_{ab} \\ x_{ab}y_{ab} & y_{ab}^2 & y_{ab}z_{ab} \\ x_{ab}z_{ab} & y_{ab}z_{ab} & z_{ab}^2 \end{bmatrix} - \begin{bmatrix} \sigma^2 & 0 & 0 \\ 0 & \sigma^2 & 0 \\ 0 & 0 & \sigma^2 \end{bmatrix} = \mathbf{r}_{ab} \otimes \mathbf{r}_{ab} - \sigma^2 \mathbf{I}_2$$

The first matrix can then be made traceless and that trace added to the second matrix to result in an expression based on the traceless and diagonal (trace) components. The traceless component of a matrix/tensor \mathbf{M} is denoted by the notation $[\mathbf{M}]_T$. The diagonal term could be simply represented as a scalar, but the full expression is retained here to be consistent with the subsequent formulations for higher order tensors.

$$\mathbf{D2} = [\mathbf{r}_{ab} \otimes \mathbf{r}_{ab}]_T + \left(\frac{r_{ab}^2}{3} - \sigma^2\right) \mathbf{I}_2$$

The third derivative of the weight function generates the 3x3x3 tensor below.

$$\sum_{b \neq a} \frac{\partial^3 w_a}{\partial \mathbf{r}^3} \Big|_{\mathbf{r}_b} = \sum_{b \neq a} \frac{\partial^3 \exp\left(-\frac{|\mathbf{r} - \mathbf{r}_a|^2}{2\sigma^2}\right)}{\partial \mathbf{r}^3} \Big|_{\mathbf{r}_b} = \frac{1}{\sigma^6} \sum_{b \neq a} \mathbf{D3} \exp\left(-\frac{r_{ab}^2}{2\sigma^2}\right)$$

$$\mathbf{D3} = \begin{bmatrix} \begin{bmatrix} 3\sigma^2 x_{ab} - x_{ab}^3 \\ \sigma^2 y_{ab} - x_{ab}^2 y_{ab} \\ \sigma^2 z_{ab} - x_{ab}^2 z_{ab} \end{bmatrix} & \begin{bmatrix} \sigma^2 y_{ab} - x_{ab}^2 y_{ab} \\ \sigma^2 x_{ab} - x_{ab} y_{ab}^2 \\ -x_{ab} y_{ab} z_{ab} \end{bmatrix} & \begin{bmatrix} \sigma^2 z_{ab} - x_{ab}^2 z_{ab} \\ -x_{ab} y_{ab} z_{ab} \\ \sigma^2 x_{ab} - x_{ab} z_{ab}^2 \end{bmatrix} \\ \begin{bmatrix} \sigma^2 y_{ab} - x_{ab}^2 y_{ab} \\ \sigma^2 x_{ab} - x_{ab} y_{ab}^2 \\ -x_{ab} y_{ab} z_{ab} \end{bmatrix} & \begin{bmatrix} \sigma^2 x_{ab} - x_{ab} y_{ab}^2 \\ 3\sigma^2 y_{ab} - y_{ab}^3 \\ \sigma^2 z_{ab} - y_{ab}^2 z_{ab} \end{bmatrix} & \begin{bmatrix} -x_{ab} y_{ab} z_{ab} \\ \sigma^2 z_{ab} - y_{ab}^2 z_{ab} \\ \sigma^2 y_{ab} - y_{ab} z_{ab}^2 \end{bmatrix} \\ \begin{bmatrix} \sigma^2 z_{ab} - x_{ab}^2 z_{ab} \\ -x_{ab} y_{ab} z_{ab} \\ \sigma^2 x_{ab} - x_{ab} z_{ab}^2 \end{bmatrix} & \begin{bmatrix} -x_{ab} y_{ab} z_{ab} \\ \sigma^2 z_{ab} - y_{ab}^2 z_{ab} \\ \sigma^2 y_{ab} - y_{ab} z_{ab}^2 \end{bmatrix} & \begin{bmatrix} \sigma^2 x_{ab} - x_{ab} z_{ab}^2 \\ \sigma^2 y_{ab} - y_{ab} z_{ab}^2 \\ 3\sigma^2 z_{ab} - z_{ab}^3 \end{bmatrix} \end{bmatrix}$$

As above the tensor can be separated into one part that does not depend on σ and one that does, as shown below.

$$\mathbf{D3} = - \begin{bmatrix} \begin{bmatrix} x_{ab}^3 \\ x_{ab}^2 y_{ab} \\ x_{ab}^2 z_{ab} \end{bmatrix} & \begin{bmatrix} x_{ab}^2 y_{ab} \\ x_{ab} y_{ab}^2 \\ x_{ab} y_{ab} z_{ab} \end{bmatrix} & \begin{bmatrix} x_{ab}^2 z_{ab} \\ x_{ab} y_{ab} z_{ab} \\ x_{ab} z_{ab}^2 \end{bmatrix} \\ \begin{bmatrix} x_{ab}^2 y_{ab} \\ x_{ab} y_{ab}^2 \\ x_{ab} y_{ab} z_{ab} \end{bmatrix} & \begin{bmatrix} x_{ab} y_{ab}^2 \\ y_{ab}^3 \\ y_{ab}^2 z_{ab} \end{bmatrix} & \begin{bmatrix} x_{ab} y_{ab} z_{ab} \\ y_{ab}^2 z_{ab} \\ y_{ab} z_{ab}^2 \end{bmatrix} \\ \begin{bmatrix} x_{ab}^2 z_{ab} \\ x_{ab} y_{ab} z_{ab} \\ x_{ab} z_{ab}^2 \end{bmatrix} & \begin{bmatrix} x_{ab} y_{ab} z_{ab} \\ y_{ab}^2 z_{ab} \\ y_{ab} z_{ab}^2 \end{bmatrix} & \begin{bmatrix} x_{ab} z_{ab}^2 \\ y_{ab} z_{ab}^2 \\ z_{ab}^3 \end{bmatrix} \end{bmatrix} + \sigma^2 \begin{bmatrix} \begin{bmatrix} 3x_{ab} \\ y_{ab} \\ z_{ab} \end{bmatrix} & \begin{bmatrix} y_{ab} \\ x_{ab} \\ 0 \end{bmatrix} & \begin{bmatrix} z_{ab} \\ 0 \\ x_{ab} \end{bmatrix} \\ \begin{bmatrix} y_{ab} \\ x_{ab} \\ 0 \end{bmatrix} & \begin{bmatrix} x_{ab} \\ 3y_{ab} \\ z_{ab} \end{bmatrix} & \begin{bmatrix} 0 \\ z_{ab} \\ y_{ab} \end{bmatrix} \\ \begin{bmatrix} z_{ab} \\ 0 \\ x_{ab} \end{bmatrix} & \begin{bmatrix} 0 \\ z_{ab} \\ y_{ab} \end{bmatrix} & \begin{bmatrix} x_{ab} \\ y_{ab} \\ 3z_{ab} \end{bmatrix} \end{bmatrix}$$

The first tensor is simply the three-fold outer product of \mathbf{r}_{ab} with itself [$\mathbf{r}_{ab} \otimes \mathbf{r}_{ab} \otimes \mathbf{r}_{ab}$], while the second has rather interesting symmetries which can be correlated with the trace of a symmetric rank 3 tensor. The trace of the symmetric rank 3 tensor $\mathbf{D3}$ is generally written as a simple vector as below, with three independent components.

$$\mathbf{T3} = Tr(\mathbf{r}_{ab} \otimes \mathbf{r}_{ab} \otimes \mathbf{r}_{ab}) = (r_{ab}^2 x_{ab}, r_{ab}^2 y_{ab}, r_{ab}^2 z_{ab})$$

$$r_{ab}^2 = x_{ab}^2 + y_{ab}^2 + z_{ab}^2$$

In general, a rank 3 tensor will have three distinct traces that depend upon which axes the contraction occurs along. The average of those three traces is equal to the trace of the symmetric portion of the general rank 3 tensor.³⁰ Since $\mathbf{D3}$ is symmetric to begin with, these traces are all equivalent to $\mathbf{T3}$. That vector can be expanded back into the form of a symmetric rank 3 tensor by the formulation below, where the symmetric trace of a matrix/tensor \mathbf{M} is designated by $[\mathbf{M}]_s$.

$$[\mathbf{r}_{ab} \otimes \mathbf{r}_{ab} \otimes \mathbf{r}_{ab}]_s(i, j, k) = \mathbf{T3}(i)\delta_{jk} + \mathbf{T3}(j)\delta_{ik} + \mathbf{T3}(k)\delta_{ij}$$

The resulting tensor, given below, is seen to have the same symmetries as the second tensor in the expression for $\mathbf{D3}$ above and is simply related to it by the scalar $\left(\frac{\sigma}{r_{ab}}\right)^2$.

$$[\mathbf{r}_{ab} \otimes \mathbf{r}_{ab} \otimes \mathbf{r}_{ab}]_S = \begin{bmatrix} \begin{bmatrix} 3r_{ab}^2 x_{ab} \\ r_{ab}^2 y_{ab} \\ r_{ab}^2 z_{ab} \end{bmatrix} & \begin{bmatrix} r_{ab}^2 y_{ab} \\ r_{ab}^2 x_{ab} \\ 0 \end{bmatrix} & \begin{bmatrix} r_{ab}^2 z_{ab} \\ 0 \\ r_{ab}^2 x_{ab} \end{bmatrix} \\ \begin{bmatrix} r_{ab}^2 y_{ab} \\ r_{ab}^2 x_{ab} \\ 0 \end{bmatrix} & \begin{bmatrix} r_{ab}^2 x_{ab} \\ 3r_{ab}^2 y_{ab} \\ r_{ab}^2 z_{ab} \end{bmatrix} & \begin{bmatrix} 0 \\ r_{ab}^2 z_{ab} \\ r_{ab}^2 y_{ab} \end{bmatrix} \\ \begin{bmatrix} r_{ab}^2 z_{ab} \\ 0 \\ r_{ab}^2 x_{ab} \end{bmatrix} & \begin{bmatrix} 0 \\ r_{ab}^2 z_{ab} \\ r_{ab}^2 y_{ab} \end{bmatrix} & \begin{bmatrix} r_{ab}^2 x_{ab} \\ r_{ab}^2 y_{ab} \\ 3r_{ab}^2 z_{ab} \end{bmatrix} \end{bmatrix}$$

The traceless version of the original rank 3 tensor is then found by subtracting off the trace multiplied by (1/5), contrasted to the (1/3) factor used for the rank 2 tensors.

$$[\mathbf{r}_{ab} \otimes \mathbf{r}_{ab} \otimes \mathbf{r}_{ab}]_T = [\mathbf{r}_{ab} \otimes \mathbf{r}_{ab} \otimes \mathbf{r}_{ab}]_S - \left(\frac{1}{5}\right) [\mathbf{r}_{ab} \otimes \mathbf{r}_{ab} \otimes \mathbf{r}_{ab}]_S$$

The expression for **D3** can then be rewritten in terms of a traceless tensor and a symmetric trace component.

$$\mathbf{D3} = -[\mathbf{r}_{ab} \otimes \mathbf{r}_{ab} \otimes \mathbf{r}_{ab}]_T + \left(\frac{\sigma^2}{r_{ab}^2} - \frac{1}{5}\right) [\mathbf{r}_{ab} \otimes \mathbf{r}_{ab} \otimes \mathbf{r}_{ab}]_S$$

This has a very similar form to the expression for **D2** above once it is recognized that

$$[\mathbf{r}_{ab} \otimes \mathbf{r}_{ab}]_{ST} = r_{ab}^2 \mathbf{I}_2$$

Similarly, the fourth derivative defines the expression

$$\sum_{b \neq a} \frac{\partial^4 w_a}{\partial \mathbf{r}^4} \Big|_{\mathbf{r}_b} = \sum_{b \neq a} \frac{\partial^4 \exp\left(-\frac{|\mathbf{r} - \mathbf{r}_a|^2}{2\sigma^2}\right)}{\partial \mathbf{r}^4} \Big|_{\mathbf{r}_b} = \frac{1}{\sigma^8} \sum_{b \neq a} \mathbf{D4} \exp\left(-\frac{r_{ab}^2}{2\sigma^2}\right)$$

The fourth rank tensor can be similarly separated into terms that depend upon the factor of σ as below

$$\mathbf{D4} = \mathbf{r}_{ab} \otimes \mathbf{r}_{ab} \otimes \mathbf{r}_{ab} \otimes \mathbf{r}_{ab} - \frac{\sigma^2}{r_{ab}^2} [\mathbf{r}_{ab} \otimes \mathbf{r}_{ab} \otimes \mathbf{r}_{ab} \otimes \mathbf{r}_{ab}]_S + \frac{\sigma^4}{2r_{ab}^4} [[\mathbf{r}_{ab} \otimes \mathbf{r}_{ab} \otimes \mathbf{r}_{ab} \otimes \mathbf{r}_{ab}]_S]_S$$

Here, the first symmetric trace tensor is defined from the trace of the original tensor, **T4**, as below

$$\mathbf{T4} = Tr(\mathbf{r}_{ab} \otimes \mathbf{r}_{ab} \otimes \mathbf{r}_{ab} \otimes \mathbf{r}_{ab}) = r_{ab}^2 \begin{bmatrix} x_{ab}^2 & x_{ab}y_{ab} & x_{ab}z_{ab} \\ x_{ab}y_{ab} & y_{ab}^2 & y_{ab}z_{ab} \\ x_{ab}z_{ab} & y_{ab}z_{ab} & z_{ab}^2 \end{bmatrix}$$

This can then be expanded back to rank 4 tensor as below

$$\begin{aligned} [\mathbf{r}_{ab} \otimes \mathbf{r}_{ab} \otimes \mathbf{r}_{ab} \otimes \mathbf{r}_{ab}]_S(i, j, k, l) \\ = \mathbf{T4}(i, j)\delta_{kl} + \mathbf{T4}(i, k)\delta_{jl} + \mathbf{T4}(i, l)\delta_{jk} + \mathbf{T4}(j, k)\delta_{il} + \mathbf{T4}(j, l)\delta_{ik} \\ + \mathbf{T4}(k, l)\delta_{ij} \end{aligned}$$

Note that it has 6 independent quantities. The second symmetric trace tensor, which is a scalar, is defined from the trace of $\mathbf{T4}$ as below:

$$S4 = Tr(Tr(\mathbf{r}_{ab} \otimes \mathbf{r}_{ab} \otimes \mathbf{r}_{ab} \otimes \mathbf{r}_{ab})) = Tr(Tr(\mathbf{T4})) = r_{ab}^4$$

$$[\mathbf{r}_{ab} \otimes \mathbf{r}_{ab}]_{ST}(i, j) = S4 \delta_{ij} = r_{ab}^4 \delta_{ij}$$

$$\begin{aligned} [[\mathbf{r}_{ab} \otimes \mathbf{r}_{ab} \otimes \mathbf{r}_{ab} \otimes \mathbf{r}_{ab}]_S]_S(i, j, k, l) \\ = [\mathbf{r}_{ab} \otimes \mathbf{r}_{ab}]_S(i, j)\delta_{kl} + [\mathbf{r}_{ab} \otimes \mathbf{r}_{ab}]_S(i, k)\delta_{jl} + [\mathbf{r}_{ab} \otimes \mathbf{r}_{ab}]_S(i, l)\delta_{jk} \\ + [\mathbf{r}_{ab} \otimes \mathbf{r}_{ab}]_S(j, k)\delta_{il} + [\mathbf{r}_{ab} \otimes \mathbf{r}_{ab}]_S(j, l)\delta_{ik} + [\mathbf{r}_{ab} \otimes \mathbf{r}_{ab}]_S(k, l)\delta_{ij} \end{aligned}$$

Note that this tensor has only 1 independent component, r_{ab}^4 , which is simply related to the r_{ab}^2 term from the $\mathbf{T4}$ tensor. As above, the expression for $\mathbf{D4}$ can be further rewritten in terms of traceless tensors as below:

$$\begin{aligned} \mathbf{D4} = [\mathbf{r}_{ab} \otimes \mathbf{r}_{ab} \otimes \mathbf{r}_{ab} \otimes \mathbf{r}_{ab}]_T - \left(\frac{\sigma^2}{r_{ab}^2} - \frac{1}{7} \right) [[\mathbf{r}_{ab} \otimes \mathbf{r}_{ab} \otimes \mathbf{r}_{ab} \otimes \mathbf{r}_{ab}]_S]_T \\ + \left(\frac{\sigma^4}{2r_{ab}^4} - \frac{\sigma^2}{3r_{ab}^2} + \frac{1}{30} \right) [[\mathbf{r}_{ab} \otimes \mathbf{r}_{ab} \otimes \mathbf{r}_{ab} \otimes \mathbf{r}_{ab}]_S]_S \end{aligned}$$

S.2 Description of strain tensors corresponding to $l=2$ deformation

The deformations represented in Figure 1 for $l=2$ can be directly mapped to Cartesian strains in mechanics literature as shown below. Note that the Cartesian z axis is arbitrarily designated as the primary axis.

$l=2, m=0$ (volume-preserving uniaxial strain state)

$$\begin{bmatrix} -\frac{1}{2}\varepsilon & 0 & 0 \\ 0 & -\frac{1}{2}\varepsilon & 0 \\ 0 & 0 & \varepsilon \end{bmatrix}$$

$l=2, m=1$ (shear strain)

$$\begin{bmatrix} 0 & 0 & 0 \\ 0 & -\varepsilon & 0 \\ 0 & 0 & \varepsilon \end{bmatrix}$$

$l=2, m=2$ (shear strain)

$$\begin{bmatrix} \varepsilon & 0 & 0 \\ 0 & -\varepsilon & 0 \\ 0 & 0 & 0 \end{bmatrix}$$

Full expressions for various moment invariants

$$\begin{aligned} \mathbf{S.3} \quad N[N[3,3]_2, N[3,3]_2]_0 &= \frac{1}{420} (16\sqrt{5}(\mu_3^0)^4 + 32\sqrt{5}(\mu_3^0)^2(\mu_3^1)^2 + 21\sqrt{5}(\mu_3^1)^4 + \\ & 80\sqrt{5}(\mu_3^0)^2(\mu_3^2)^2 + 30\sqrt{5}(\mu_3^1)^2(\mu_3^2)^2 - 40\sqrt{5}(\mu_3^0)^2(\mu_3^3)^2 - 10\sqrt{5}(\mu_3^1)^2(\mu_3^3)^2 + \\ & 50\sqrt{5}(\mu_3^2)^2(\mu_3^3)^2 + 25\sqrt{5}(\mu_3^3)^4 - 40\sqrt{3}(\mu_3^0)(\mu_3^1)^2(\mu_3^2)\text{Cos}[2(\theta_1 - \theta_2)] + \\ & 120\sqrt{5}(\mu_3^0)(\mu_3^1)(\mu_3^2)(\mu_3^3)\text{Cos}[\theta_1 + 2\theta_2 - 3\theta_3] - 40\sqrt{3}(\mu_3^1)^3(\mu_3^3)\text{Cos}[3(\theta_1 - \theta_3)] + \\ & 100\sqrt{3}(\mu_3^1)(\mu_3^2)^2(\mu_3^3)\text{Cos}[\theta_1 - 4\theta_2 + 3\theta_3]) \end{aligned}$$

$$\begin{aligned} \mathbf{S.4} \quad N[N[4,4]_2, N[4,4]_2]_0 &= \frac{1}{13860} (\sqrt{5}(400(\mu_4^0)^4 + 589(\mu_4^1)^4 + 64(\mu_4^2)^4 + 938(\mu_4^2)^2(\mu_4^3)^2 + \\ & 49(\mu_4^3)^4 - 112((\mu_4^2)^2 - 14(\mu_4^3)^2)(\mu_4^4)^2 + 784(\mu_4^4)^4 + (\mu_4^1)^2(758(\mu_4^2)^2 + 518(\mu_4^3)^2 - \\ & 952(\mu_4^4)^2) + 40(\mu_4^0)^2(20(\mu_4^1)^2 + 62(\mu_4^2)^2 - 7((\mu_4^3)^2 + 4(\mu_4^4)^2))) + \\ & 60(-42(\mu_4^0)(\mu_4^1)^2(\mu_4^2)\text{Cos}[2(\theta_1 - \theta_2)] + 46\sqrt{7}(\mu_4^0)(\mu_4^1)(\mu_4^2)(\mu_4^3)\text{Cos}[\theta_1 + 2\theta_2 - 3\theta_3] - \\ & 6\sqrt{35}(\mu_4^1)^3(\mu_4^3)\text{Cos}[3(\theta_1 - \theta_3)] - 4\sqrt{35}(\mu_4^1)^2(\mu_4^2)(\mu_4^4)\text{Cos}[2(\theta_1 + \theta_2 - 2\theta_4)] + \\ & 2\sqrt{7}(\mu_4^2)(\mu_4^4)(12(\mu_4^0)(\mu_4^2)\text{Cos}[4(\theta_2 - \theta_4)] + 7\sqrt{5}(\mu_4^3)^2\text{Cos}[2(\theta_2 - 3\theta_3 + 2\theta_4)]) + \\ & (\mu_4^1)(\mu_4^3)(9\sqrt{35}(\mu_4^2)^2\text{Cos}[\theta_1 - 4\theta_2 + 3\theta_3] + 28(\mu_4^0)(\mu_4^4)\text{Cos}[\theta_1 + 3\theta_3 - 4\theta_4] + \\ & 42\sqrt{5}(\mu_4^2)(\mu_4^4)\text{Cos}[\theta_1 - 2\theta_2 - 3\theta_3 + 4\theta_4])) \end{aligned}$$

$$\begin{aligned}
\mathbf{S.5} \quad N[N[N[4,4]_2, N[4,4]_2]_2, N[4,4]_2]_0 &= \frac{1}{58212\sqrt{770}} \left\{ \sqrt{7} \{ 8000(\mu_4^0)^6 + 512(\mu_4^2)^6 + \right. \\
&168(\mu_4^2)^4(67(\mu_4^3)^2 - 80(\mu_4^4)^2) - 147(\mu_4^2)^2 \{ 67(\mu_4^3)^4 + 812(\mu_4^3)^2(\mu_4^4)^2 - 320(\mu_4^4)^4 \} - \\
&343 \{ (\mu_4^3)^6 + 48(\mu_4^3)^4(\mu_4^4)^2 + 192(\mu_4^3)^2(\mu_4^4)^4 + 64(\mu_4^4)^6 \} - 1200(\mu_4^0)^4 \{ 100(\mu_4^2)^2 + 7(\mu_4^3)^2 + \\
&28(\mu_4^4)^2 \} - 60(\mu_4^0)^2 \{ 800(\mu_4^2)^4 - 7(\mu_4^2)^2 [167(\mu_4^3)^2 + 320(\mu_4^4)^2] - 49[(\mu_4^3)^4 + \\
&20(\mu_4^3)^2(\mu_4^4)^2 + 16(\mu_4^4)^4] \} + 252(\mu_4^2) \left[-12\sqrt{5}(\mu_4^0)(\mu_4^2)(\mu_4^4) [40(\mu_4^0)^2 + 16(\mu_4^2)^2 + 91(\mu_4^3)^2 - \right. \\
&56(\mu_4^4)^2] \text{Cos}[4\bar{\omega}_2] - (\mu_4^3)^2 \left\{ 7(\mu_4^4) [-100(\mu_4^0)^2 + 35(\mu_4^2)^2 + 35(\mu_4^3)^2 + 224(\mu_4^4)^2] \text{Cos}[2\{\bar{\omega}_2 - \right. \\
&\left. 3\bar{\omega}_3\}] + 9\sqrt{35}(\mu_4^0) \{ 25(\mu_4^2)^2 \text{Cos}[6\{\bar{\omega}_2 - 3\bar{\omega}_3\}] + 28(\mu_4^4)^2 \text{Cos}[2\{\bar{\omega}_2 + 3\bar{\omega}_3\}] \} \} \left. \right\}
\end{aligned}$$

$$\mathbf{S.6} \quad (N[4,4]_0)^2 = \frac{11\sqrt{5}}{49} N[N[4,4]_2, N[4,4]_2]_0 + \frac{143}{98} N[N[4,4]_4, N[4,4]_4]_0$$

$$\mathbf{S.7} \quad (N[4,4]_0)^2 = \frac{77\sqrt{5}}{200} N[N[4,4]_2, N[4,4]_2]_0 + \frac{11\sqrt{13}}{40} N[N[4,4]_6, N[4,4]_6]_0$$

$$\mathbf{S.8} \quad (N[4,4]_0)^2 = -\frac{28\sqrt{5}}{75} N[N[4,4]_2, N[4,4]_2]_0 + \frac{13\sqrt{17}}{30} N[N[4,4]_8, N[4,4]_8]_0$$

$$\begin{aligned}
\mathbf{S.9} \quad N[N[N[4,4]_4, N[4,4]_4]_4, N[4,4]_4]_0 &= \frac{1}{2004002} (17496(\mu_4^0)^6 - 79992(\mu_4^0)^4(\mu_4^2)^2 + \\
&164804(\mu_4^0)^2(\mu_4^2)^4 - 28248(\mu_4^2)^6 - 394632(\mu_4^0)^4(\mu_4^3)^2 + 410508(\mu_4^0)^2(\mu_4^2)^2(\mu_4^3)^2 - \\
&76104(\mu_4^2)^4(\mu_4^3)^2 + 460404(\mu_4^0)^2(\mu_4^3)^4 - 56889(\mu_4^2)^2(\mu_4^3)^4 - 27783(\mu_4^3)^6 + \\
&139608(\mu_4^0)^4(\mu_4^4)^2 - 660352(\mu_4^0)^2(\mu_4^2)^2(\mu_4^4)^2 + 122346(\mu_4^2)^4(\mu_4^4)^2 - \\
&966672(\mu_4^0)^2(\mu_4^3)^2(\mu_4^4)^2 - 12348(\mu_4^2)^2(\mu_4^3)^2(\mu_4^4)^2 - 37044(\mu_4^3)^4(\mu_4^4)^2 + \\
&108584(\mu_4^0)^2(\mu_4^4)^4 - 116424(\mu_4^2)^2(\mu_4^4)^4 + 24696(\mu_4^3)^2(\mu_4^4)^4 + 8232(\mu_4^4)^6 + \\
&24\sqrt{35}(\mu_4^0)(\mu_4^2)^2(\mu_4^4)(2818(\mu_4^0)^2 - 2937(\mu_4^2)^2 - 4837(\mu_4^3)^2 + 3738(\mu_4^4)^2) \text{Cos}[4\bar{\omega}_2] + \\
&198450(\mu_4^2)^4(\mu_4^4)^2 \text{Cos}[8\bar{\omega}_2] - 5040\sqrt{7}(\mu_4^0)^2(\mu_4^2)(\mu_4^3)^2(\mu_4^4) \text{Cos}[2(\bar{\omega}_2 - 3\bar{\omega}_3)] + \\
&26460\sqrt{7}(\mu_4^2)^3(\mu_4^3)^2(\mu_4^4) \text{Cos}[2(\bar{\omega}_2 - 3\bar{\omega}_3)] + 26460\sqrt{7}(\mu_4^2)(\mu_4^3)^4(\mu_4^4) \text{Cos}[2(\bar{\omega}_2 - 3\bar{\omega}_3)] + \\
&70560\sqrt{7}(\mu_4^2)(\mu_4^3)^2(\mu_4^4)^3 \text{Cos}[2(\bar{\omega}_2 - 3\bar{\omega}_3)] + 52500\sqrt{5}(\mu_4^0)(\mu_4^2)^3(\mu_4^3)^2 \text{Cos}[6(\bar{\omega}_2 - \bar{\omega}_3)] + \\
&58800\sqrt{5}(\mu_4^0)(\mu_4^2)(\mu_4^3)^2(\mu_4^4)^2 \text{Cos}[2(\bar{\omega}_2 + 3\bar{\omega}_3)]
\end{aligned}$$